UNIVERSITY OF CALIFORNIA SAN DIEGO

# Organization of Information-Processing Biological Networks

A dissertation submitted in partial satisfaction of the requirements for the degree

Doctor of Philosophy

in

Neurosciences with a specialization in Computational Neurosciences

by

Javier Josue How

Committee in charge:

Professor Saket Navlakha, Chair
Professor Jing Wang, Co-Chair
Professor Maksim Bazhenov
Professor Sreekanth Chalasani
Professor Eran Mukamel

2020

The dissertation of Javier Josue How is approved, and it is acceptable in quality and form for publication on microfilm and electronically:

---

---

---

---

Co-Chair

---

Chair

University of California San Diego

2020

DEDICATION

*Para mi madre*

TABLE OF CONTENTS

LIST OF FIGURES

LIST OF TABLES

ACKNOWLEDGEMENTS

It should come as no surprise that I owe a great debt to my advisors, Saket Navlakha and Shrek Chalasani, for cultivating my scientific rigor, urging and helping me to think of my long-term scientific and career interests, and ensuring it was a pleasure to come to work (if one ever really leaves). Similarly, my committee members have provided valuable advice, related to both my science and my career, for which I am grateful.

As a co-advisee, I had the pleasure to work alongside lovely computational and experimental lab members. Special thanks go to Corinne Lee-Kubli, for taking an interest in my training and providing helpful guidance on everything from the minutiae of my projects to choosing a good coffee setup for home use.

Finally, I would like to thank my family and friends. I have also had the good fortune to have excellent roommates who have become close friends, particularly my current roommate, Cayce, who has become my best friend.

Chapter 2, in full, is a reprint of the material as it appears in Evidence of Rentian Scaling of Functional Modules in Diverse Biological Networks. How, Javier J.; Navlakha, Saket. Neural Computation, 2018. The dissertation author was the primary investigator and author of this paper.

Chapter 3, in full, is a manuscript submitted for publication. Neural network features distinguish chemosensory stimuli in *Caenorhabditis elegans*. How, Javier J.; Navlakha, Saket; Chalasani, Sreekanth H, 2020. The dissertation author was the primary investigator and author of this paper.

## VITA

2015 Bachelor of Science, Florida International University

2020 Doctor of Philosophy in Neurosciences, University of California San Diego

## PUBLICATIONS

Yeh C, **How JJ,** Rosales K, Villa-Real R, DePasquale E, Groisman A, Chalasani SH (under review) A many-to-one sensory circuit encodes oxygen levels and drives respiratory behavior in *Danio rerio*

**How JJ,** Navlakha S, Chalasani SH (submitted) Neural network features distinguish chemosensory stimuli in *Caenorhabditis elegans*

**How JJ,** Navlakha S (2018) Evidence of Rentian Scaling of Functional Modules in Diverse Biological Networks. *Neural Computation* 30(8): 2210-2244.

Kaftanovskaya EM*, Soula M*, Myhr C, Ho BA, Moore SN, Yoo C, Cervantes B, **How JJ,** Marugan J, Agoulnik IU, Agoulnik AI (2017) Human Relaxin Receptor is Fully Functional in Humanized Mice and is Activated by Small Molecule Agonist ML290. *Journal of the Endocrine Society* 1(6): 712 - 725.

Ferguson L, **How JJ,** Agoulnik AI (2013) The Fate of Spermatogonial Stem Cells in the Cryptorchid Testes of RXFP2 Deficient Mice. *PLoS ONE* 8(10): e77351.

## FIELDS OF STUDY

Major Field: Neurosciences with a specialization in Computational Neurosciences

ABSTRACT OF THE DISSERTATION

Organization of Information-Processing Biological Networks

by

Javier Josue How

Doctor of Philosophy in Neurosciencess with a specialization in Computational Neurosciences

University of California San Diego, 2020

Professor Saket Navlakha, Chair

Professor Jing Wang, Co-Chair

Despite considerable effort over the past several decades, it is unclear how an organism's nervous system extracts ecologically relevant information about its environment. The connections between individual neurons (i.e. the structural connectome), and the ways in which these connections are used (i.e. the functional connectome), likely constrain how a nervous system performs this feat. The nematode *Caenorhabditis elegans* (*C. elegans*) presents a rare opportunity to study both of these aspects of a nervous system, since the complete structural connectome of one individual has been published, and recent technological advances enable scientists to record from a large part of its nervous system. I studied the *C. elegans* nervous system from both of these perspectives to better understand the structural features and network-level dynamics that allow it to extract information about the environment.

I found that the *C. elegans* structural connectome, along with those of several other biological networks, display Rentian scaling – a power-law relationship between the number of nodes in a module and the number of connections to nodes in other modules. This indicates that these biological networks, but not other social and technological networks, must negotiate a trade-off between the efficiency of information transfer and cost to maintain connections. Thus, Rentian scaling may be a feature unique to information-processing networks, either because it presents an organizational principle used to process information, or because it indicates the existence of fundamental design constraints these networks share.

While a structural connectome constrains which neurons may communicate, a functional connectome can indicate which pathways of information transfer are actually used, with the caveat that statistical dependencies may reveal interactions that are

actually false positives. I recorded from most neurons in the brain of adult *C. elegans*, and characterized their inferred functional connectome using tools from graph theory. I found that some patterns of activity were consistently modulated in a valence- or identity-specific manner. Moreover, these patterns could be used to identify which chemical an animal was experiencing. This indicates that studying the functional connectome of large-scale neural recordings may provide a mechanistic account of how neural networks extract and represent information about their environment.

## 1. Introduction

Many approaches to understand how neurons in an organism's brain extract information about its environment have been tried. Some studies have focused on individual regions of the brain, delineated based on cytoarchitectonic or functional properties (e.g. Brodmann area 17, or V1). These have typically looked at how single neurons respond to artificial stimuli with simple properties (e.g. orientation of a bar of light; Hubel and Wiesel, 1959), or how local circuits implement advanced computations (e.g. surround suppression; Adesnik et al., 2012; Nienborg et al., 2013). Other studies have also looked at how long-range inputs and behavioral state modulate activity across the brain (e.g. the role of cholinergic projections from the basal forebrain to V1; Fu et al., 2014). While these studies have uncovered important aspects about how individual or small numbers of neurons represent the sensory environment, due to technical limitations, they have been limited to observing a subset of everything that the brain is doing at any given time.

A more thorough understanding requires one to explain how the brain as a whole represents and extracts information from the world, and then uses this information to guide behavior. Ultimately, this requires an understanding of how individual neurons respond to arbitrary stimuli, why neurons are connected to each other in a certain way (i.e. the brain's structural connectivity), and how this structural backbone is used to transmit and process information as it moves across the brain (i.e. its functional connectivity). This would allow us to predict how an organism will respond to any given stimulus by precisely modeling the patterns of activity that represent the environment and

produce behavior. To do this, we will need to understand how these patterns of activity embody and perform these functions.

The hermaphrodite of the nematode *Caenorhabditis elegans* (*C. elegans*) is the ideal animal in which to ask these questions. Its nervous system has just 302 neurons, all of which are stereotyped between individuals, and the structural connectivity between these neurons, for at least one individual, has been previously published (White et al., 1986; Varshney et al., 2011). Furthermore, modern technology allows scientists to record from a large portion of its nervous system, thereby revealing large-scale patterns of activity in response to different stimuli (Schrodel et al., 2013). Finally, several of its behaviors, such as chemotaxis towards food odorants (Bargmann et al., 1993), have been well-studied, which allows us to ask ecologically-relevant questions about nervous system function.

In my dissertation, I focused on how the structural and functional connectivity of this nervous system help it extract information about its environment. I found that its structural connectivity prioritizes large-scale integration of information (Chapter 2), and that patterns of functional connectivity are modulated in a stimulus-specific manner (Chapter 3). First, I will describe the theoretical framework I used, how it has been applied to characterize several complex networks, and why it may be more informative than other commonly used techniques in neuroscience.

### 1.1 Structural connectivity of complex networks

Past studies have used a graph-theoretic framework to study the basic organizational principles of various networks. Graph theory is the study of mathematical

objects called graphs, or networks. Networks are composed of a set of elements, called nodes, connected by a set of connections, called edges. These edges can be binary (Figure 1A), which indicates the presence or absence of a connection between two nodes, or weighted (Figure 1B), which specifies the strength of this interaction. These edges can also be undirected, which implies that a pair of nodes affect each other equally, or directed, to show that one node in a pair can affect the other node, but not vice-versa (Figure 1C). Edges can also be signed, where a positive value on an edge indicates similarity or activation, and a negative number implies dissimilarity or suppression (Figure 1D). Finally, nodes can interact with themselves, graphically depicted with a self-loop. Networks of this last variety are less commonly used (Newman, 2010).

Networks can be mathematically represented using an adjacency matrix. For a set of $n$ nodes, the entries of the $n$ x $n$ adjacency matrix, call it $A$, indicate the nature of the interaction or relationship between the nodes in the corresponding row and column. In other words, each entry, $A_{ij}$, describes the edge between two nodes.

This graph-theoretic framework was first used in sociology, but eventually made its way to the study of biological networks. One of the first biological networks studied was the *C. elegans* nervous system as it represented, until recently, the only example of a complete structural connectome in neuroscience. (A connectome is the chemical and electrical connectivity between neurons of a nervous system). Other commonly studied networks include the network of physical interactions between proteins, or transcriptional regulation between genes. These biological networks may be considered to be “information processing” networks, because they take signals from the environment and adapt the dynamics of and interactions between nodes to coordinate an adaptive

response. Some social networks, such as one composed of actors who were in the same movie, likely do not process information.

In spite of this distinction, several groups have found commonalities in the structures of information and non-information processing networks. I will focus on a few, widely analyzed properties, and describe one property that seems to be unique, and therefore potentially important, to information processing networks.

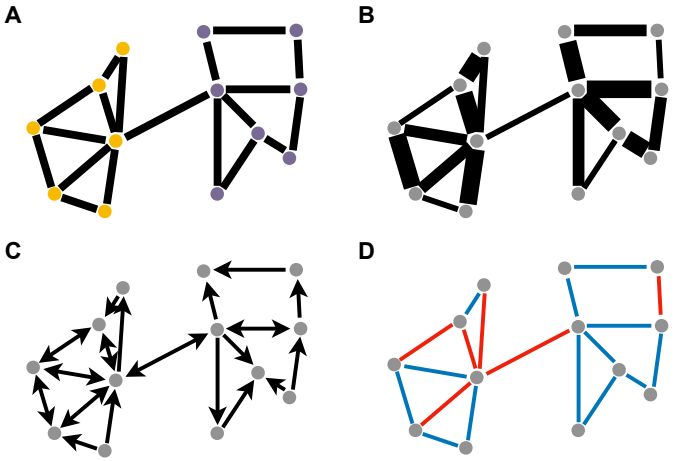


Figure 1.1 Common types of networks. Each circle represents a node (e.g. neuron) and each line an edge between a pair of nodes (e.g. a structural or functional interaction). Edges can be either absent or present (A), weighted (B, line thickness corresponds to weight or strength), directed (C, one-way relationship between a pair of nodes, with the receiver indicated by the arrowhead), or signed (D, where blue is excitatory /inducive, and red is inhibitory/repressive). Note that some networks can have multiple edge types (e.g. a signed, directed, and weighted network). The network in (A) is composed of two modules; neurons in the same module have the same color (i.e. yellow or purple).

### 1.1.1 Small-worldness

Watts and Strogatz (1998) found that the *C. elegans* nervous system, as well as a collaboration network of film actors and the electrical power grid of the Western United States, was a small-world network. A small-world network is characterized by densely connected local neighborhoods (i.e. a large clustering coefficient), yet short pathways linking any two nodes on average (i.e. a small characteristic path length). This indicates

that any two nodes in these three networks can quickly communicate. Watts and Strogatz (1998) also found that these types of networks, compared to regular or random networks, more quickly propagate signals, are more computationally powerful, and readily synchronize. This suggests that information can rapidly spread throughout the *C. elegans* nervous system, which may help it quickly react to changes in the animal's external environment. However, the small-worldness property is defined relative to random networks, which may not be fitting reference points since they are typically formed without controlling for every possible graph-theoretic feature and don't incorporate domain-specific knowledge on how networks form (Papo et al., 2016). Furthermore, the fact that an energy transfer network and a social network are both small-world indicates that this property is not unique to information processing networks. Is there a property that can distinguish between information processing and non-information processing networks? Such a property may be relevant to how the *C. elegans* nervous system and other information processing networks perform computations.

### 1.1.2 Rich clubs

Many studies have carefully analyzed the structural properties of the *C. elegans* nervous system, and found that some of these properties are shared by non-information processing networks. Towlson et al. (2013), for instance, found that the *C. elegans* nervous system has a rich-club of eleven efficiently connected high-degree neurons, or hubs, mostly composed of command interneurons that strongly regulate movement. (Degree refers to the number of neurons connected to the neuron of interest). Therefore, one way in which the *C. elegans* nervous system integrates information is by connecting

neurons which themselves integrate information from many other neurons. While this may seem to be an organizational principle that could be useful for information processing networks, Colizza et al. (2006) noted that, among others, a social network of scientific collaborations also has a rich-club, but a network composed of interactions amongst proteins did not. This indicates that the presence of a rich-club is not an unique property of information processing networks, but is found in many types of networks.

### 1.1.3 Motifs

Certain types of subnetworks, called motifs, embedded within the larger network, may be unique to information processing networks. Milo et al. (2002) compared the frequencies of 3- and 4-node motifs in various networks to random networks. They found that information processing networks, such as the *C. elegans* nervous system, the genetic regulatory network from *Escherichia coli*, and a few forward logic chips, shared a couple of motifs that were different from those found in non-information processing networks. Therefore, certain network motifs may serve as the basic building blocks of computation in information processing networks, or indicate the presence of design constraints common to these types of networks.

### 1.1.4 Modules

Modules are sets of nodes in a network that are densely interconnected, yet sparsely connected to nodes in other modules (Figure 1A). Many real networks are known to be modular, and it is believed that nodes in a module have similar functions. For instance, within a metabolic network, metabolites involved in the production of pyrimidines

are in the same module, separate from metabolites that synthesize dissacharides (Ravasz et al., 2002). Some networks are hierarchically modular, wherein smaller modules are embedded in larger modules across different hierarchical levels; this is believed to offer modules the chance to evolve more-or-less independently of one another, and to spare the rest of the network from damage inflicted to any one module (Simon, 1962; Kashtan and Alon, 2005). Ravasz et al. (2002) found that the metabolic networks of 43 species are hierarchically modular, and that these modules closely correspond to known biochemical pathways. Similarly, the *C. elegans* nervous system and human brain structural and functional connectivity networks are also hierarchically modular (Bassett et al., 2010). However, both Ravasz et al. (2003) and Sales-Pardo et al. (2007) noted that some, but not all, social and technological networks are also hierarchically modular, which shows that this property may not be unique to information processing networks. Rather, hierarchical modularity may be a property of many complex networks.

### 1.1.5 Rentian scaling

The fact that some small-world networks are modular suggests that while nodes are segregated into specialized processing modules, there are sparse, long-range connections between these modules that ultimately permit efficient communication across the network. While both small-worldness and modularity are not unique to information processing networks, the pattern of these sparse, long-range, integrative connections could be. E.F. Rent first discovered a power-law relationship between the number of gates (nodes) in a logic block (module) and the number of inputs and outputs

to and from that logic block in electronic circuits (Landman and Russo, 1971; Lanzerotti, Fiorenza, and Rand, 2005). This relationship is called Rentian scaling, and the exponent of this power-law, called the Rent's exponent, represents a trade-off between the efficiency of communication between gates and the cost of wiring an electronic circuit. Therefore, the presence of Rentian scaling and its exponent suggest the presence of a design constraint that may be unique to information processing networks. Consistently, Bassett et al. (2010) found that the *C. elegans* nervous system and structural human brain networks also exhibited Rentian scaling.

Though these studies suggest that Rentian scaling may be unique to information processing networks, Sperry et al. (2016) noted that the London Underground, a transportation network, also demonstrated Rentian scaling. Nonetheless, both Bassett et al. (2010) and Sperry et al. (2016) used partitioning algorithms to define spatial or topological modules, which may bias towards the presence of Rentian scaling. In Chapter 2, I defined functional modules, composed of nodes that share a common function, and found that the *C. elegans* nervous system, as well as several biological networks, displayed Rentian scaling, while social and technological networks did not. Furthermore, the Rent's exponents in these networks were larger than the Rent's exponent of the London Underground, yet similar to those found for electronic circuits and biological neural networks. Therefore, Rentian scaling may be a feature unique to information processing networks, or may separate these networks from non-information processing networks by differences in the magnitude of the Rent's exponent. In any case, it seems that the *C. elegans* nervous system prioritizes the integration of information from functionally distinct neurons over costs incurred to maintain these connections.

## 1.2 Understanding neural activity

While many other studies have focused on the structural characteristics (e.g. Varshney et al., 2011; Reigl et al., 2004; Bentley et al., 2016) and generative mechanisms (e.g. Chen et al., 2006; Kaiser and Hilgetag, 2006; Ahn et al., 2006; Perez-Escudero and de Polavieja, 2007; Perez-Escudero et al., 2009; Varier and Kaiser, 2011; Nicosia et al., 2013) of the *C. elegans* nervous system, several groups have used its connectome to form hypotheses regarding the role of individual neurons in specific behaviors. Chalfie et al. (1985), for instance, hypothesized that the AVA, AVB, AVD, and PVC interneurons were involved in the nematode's response to touch because, according to the connectome, they received inputs from touch cells, and sent outputs to motor neurons. They eliminated these neurons one at a time, and found that the AVD and PVC neurons were involved in touch sensitivity, while the AVA and AVB neurons were more important for movement in general. This example illustrates that a connectome can be suggestive of network function and behavior, but that one's intuition can be inaccurate. Consistently, Gray et al. (2005) used the connectome to identify four pairs of neurons that could be involved in sensory-driven exploratory behaviors, but found that they all function under different environmental conditions. Work on other biological networks has also noted that topologically identical networks can have different functions depending on the dynamics of their individual nodes (e.g. Guet et al., 2002), and this may be particularly true of nervous systems in general, with their rich diversity of cell types (e.g. neurons, interneurons, glia) and chemical messengers (e.g. neurotransmitters, neuromodulators) (see reviews by Tremblay et al., 2016; Lee and Dan, 2012).

Therefore, an understanding of the *C. elegans* nervous system requires us to measure neuronal dynamics. This will contribute to our ultimate goal of being able to predict a nervous system's response to an environmental signal, and to understand how the ensuing patterns of activity process information and produce complex behaviors. Though recent advances allow us to record from a large portion of a nervous system, it is not clear how to bridge the gap from large scale neural activity to behavior. Hence, new theoretical frameworks are needed.

### 1.2.1 Measuring neural activity

Optical reporters of *C. elegans* neural activity are ideal. Genetically encoded calcium indicators, such as those in the GCaMP family, fluoresce in response to an increase of intracellular calcium (Nakai et al., 2001). Neurons in *C. elegans* express voltage-gated calcium channels, and do not express voltage-gated sodium channels (Bargmann, 1998). Moreover, calcium seems to be the ion primarily responsible for neuronal depolarization (Goodman et al., 1998; Liu et al., 2018). Altogether, this indicates that the influx of calcium into a *C. elegans* neuron is a good proxy of neuronal depolarization. Consequently, various groups have generated transgenic animals with GCaMP localized in one or more neurons, and then used microscopes to record changes in neuronal fluorescence (and, hence, activity) in response to any number of stimuli.

These calcium-imaging studies have revealed important aspects about *C. elegans* circuit dynamics. For instance, some groups used this technique to describe the responses of single neurons in response to chemical stimuli, such as odors or salt, and contextualized these findings with a molecular dissection of the local feedforward and

feedback circuitry in which these neurons are embedded (e.g., Chalasani et al., 2007; Chalasani et al., 2010; Leinwand and Chalasani, 2013). A few groups used calcium imaging to describe the combinatorial code used by the *C. elegans* olfactory sensory neurons to represent different concentrations of different monomolecular odorants (Yoshida et al., 2012; Leinwand et al., 2015; Zaslaver et al., 2015; Hale et al., 2016). These studies, however, were limited to recording from just one or a few neurons at a time, preventing them from analyzing large-scale patterns of nervous system activity.

### 1.2.2 Summarizing large-scale neural recordings with dimensionality reduction

Although others have made use of recent technological and biological advances to record from a large number of neurons in the *C. elegans* nervous system at once (Schrodel et al., 2013), it is unclear how to make sense of this data. Neuroscientists studying other organisms have used dimensionality reduction techniques to simplify and understand multi-neuron recordings for several years now (see review by Cunningham and Yu, 2014). For instance, Stopfer et al. (2003) used locally linear embedding (LLE) to determine that populations of projection neurons in the locust antennal lobe have "concentration-specific trajectories on odor-specific manifolds." Briggman et al. (2005) used principal components analysis (PCA) to find ensemble activity that is related to a leech's decision to swim or crawl, and linear discriminant analysis (LDA) to find candidate decision-making neurons. Churchland et al. (2012) developed jPCA, a form of PCA that identifies rotations in state space, to identify surprisingly consistent rotational dynamics in neuronal activity in primary motor area (M1) of rhesus macaques while they perform

different types of arm reaches. All of these studies simplified complex, multi-neuronal recordings to find patterns that were not otherwise easily detectable.

Other than LLE, LDA, PCA, and jPCA, several other dimensionality reduction methods have been developed to leverage time-series data (e.g. Gaussian process factor analysis; Yu et al., 2009), account for multiple dependent variables (e.g. demixed PCA; Brendel et al., 2011), and capture nonlinear relationships between latent and observed variables (e.g. Isomap; Tenenbaum et al., 2000). These, and many other studies using dimensionality reduction, are reviewed elsewhere (Cunningham and Yu, 2014). An alternative approach that uses dimensionality reduction is to record from many neurons in animals performing a task, build a network model that reproduces the same relationship between stimulus and behavior, verify that the experimental observations and network model have similar dynamics by analyzing their low-dimensional manifolds, and then dissect these models to study how a biological neural network could produce the observed experimental data (see review by Williamson et al., 2019). Therefore, dimensionality reduction can be leveraged as a tool to constrain network models.

Studies of whole-brain imaging datasets in *C. elegans* have also used dimensionality reduction techniques to reveal the existence of fundamental network states. Kato et al. (2015) used PCA to determine that population activity in the *C. elegans* 'brain', composed of a dense collection of neurons in the animal's head, transitioned through a few low-dimensional motor command states to organize action sequences. Nichols et al. (2017) and Skora et al. (2018) used PCA to identify fixed-point attractors in putatively sleeping animals. Though these studies suggest that neural activity in the *C. elegans* brain is low-dimensional, it is important to note that these animals were all

physically and chemically immobilized. Instead, Scholz et al. (2018), recording from moving *C. elegans*, used PCA to show that whole-brain population activity is high-dimensional. Similarly, in Chapter 3, I show that population activity in immobilized animals exposed to chemical stimuli is also high-dimensional. Hence, it seems that a low-dimensional description of population activity, even in a relatively small nervous system, will be insufficient to explain a substantial portion of neural activity.

These studies used dimensionality reduction to concisely summarize the patterns of activity observed in large-scale neuronal recordings. As pointed out by Cunningham and Yu (2014), dimensionality reduction can improve single-trial statistical power by using multi-neuron activity to make sense of otherwise seemingly 'noisy' single-neuron responses, reveal neural mechanisms that emerge at the level of a population of neurons yet may be obscure at a single-neuron level, and facilitate exploratory analyses by summarizing the responses of many neurons. Though powerful, these methods are just one way of identifying how population activity is organized.

### 1.2.3 Characterizing functional connectivity with graph theory

A different, arguably more mechanistic, way of representing patterns of activity would be to directly study the interactions between neurons using graph theory. This requires one to record the activity of many neurons in a nervous system and then infer, or directly measure, the interactions between them. This approach recognizes that population activity is sculpted by the interactions between individual neurons, and that the structure of these interactions is likely to be important to our understanding of any nervous system. Rather than summarize population activity in a lower-dimensional space, which

is likely not overtly biologically instantiated by the nervous system, modeling the activity as interactions between neurons may reveal pathways of neural communication by which information is actively processed and transformed. However, this approach is most powerful when one can observe a large portion of the population of interest. If one is unable to record from most of the neurons that can be reasonably expected to play a role in an experiment (which, in many cases, is theoretically the entire nervous system), they may detect spurious interactions between neurons due to, for instance, a common input. In these cases, dimensionality reduction may be a more useful starting point (Cunningham and Yu, 2014).

The human neuroimaging field has used graph theory to study the functional connectivity of the brain for many decades now, and has found several similarities to the networks discussed so far. For instance, using functional magnetic resonance imaging (fMRI) to measure a proxy of neural activity in the brain (see review by Glover, 2011), Eguíluz et al. (2005) found that functional brain networks are small-world. Bassett et al. (2010) noted that structural brain networks, derived from another technique called diffusion spectrum imaging (DSI; see review by O'Donnell and Westin, 2011), are hierarchically modular, while others found that the same was true of functional brain networks (see Supekar et al., 2009, Meunier et al., 2009b). These results are consistent with findings in the *C. elegans* nervous system, and other complex networks. Finally, several graph-theoretic properties of the human brain's functional network are dysregulated in disease, which suggests that these properties may represent important organizational principles in the brain (see reviews by van den Heuvel and Pol, 2010, and Wang et al., 2010).

Although fMRI allows one to record from the entire brain, it is limited by low spatial resolution (the basic unit, voxels, contain many cells), low temporal resolution (sampling rates are slow), a reliance on a blurred proxy of neural activity (the BOLD response), and difficulties in defining a node in the network in a principled manner (which has resulted in the use of wildly different parcellation schemes across studies; see review by Hallquist and Hillary, 2018). Fortunately, recent technological advances allow scientists to record from the entire brain of the nematode *C. elegans* and zebrafish *Danio rerio* (*D. rerio*) with high spatial and temporal resolution, where the use of a GCaMP indicator provides a good proxy of neural activity (Ahrens et al., 2012; Schrodel et al., 2013; Chen et al., 2013). Furthermore, neurons are naturally defined as nodes in these networks, precluding the use of arbitrary parcellation schemes.

A few studies have focused on the large-scale interactions between neurons in *D. rerio*. These groups first clustered nearby neurons with similar responses to a given stimulus into single nodes, thereby removing redundancy in the neural code and producing a much smaller adjacency matrix than the one that would be formed by the roughly 100,000 neurons in the animal's brain. They then used techniques from graph theory to describe how regions of the brain interact. Marquez-Legorreta et al. (2019) and Constantin et al. (2019), for instance, studied sensory responses in a zebrafish model of fragile X syndrome (FXS), which in humans is associated with slowed habituation to repeated stimulus presentation and auditory hypersensitivity. Marquez-Legorreta et al. (2019) found that habituation to threatening visual stimuli accompanies a loss of strong interactions among functionally distinct neurons across the brain of wild-type fish, and that mutant animals lose these interactions more slowly, yet recover them more quickly.

As a result, they propose that animal models of FXS habituate more slowly because they maintain stronger network interactions for a longer period of time. Similarly, Constantin et al. (2019) found that auditory-responsive brain regions in animal models of FXS were more strongly connected, and more easily recruited at lower volumes, than those in wild-type animals, suggesting that auditory hypersensitivity in FXS may be partly due to excess transmission of auditory information throughout the brain. Vanwalleghem et al. (2020), on the other hand, studied the representation of water flow in healthy animals. They found that neurons responsive to head-to-tail water flow are most strongly connected to other types of flow-responsive neurons (e.g. tail-to-head water flow), indicating that the zebrafish brain prioritizes the detection and processing of water flow experienced by forward-moving animals. While these studies revealed interesting aspects of sensory processing in health and disease, future efforts should make sense of the roles of seemingly redundant neurons, and not cluster them into single nodes, although the computational costs of analyzing such a large adjacency matrix could be substantial. More importantly, while these studies focused on simpler metrics, like the strength of inferred interactions between brain regions, there are many graph-theoretic properties, and therefore ways of characterizing neural network interactions, which should be considered holistically to make sense of patterns of activity in the brain.

In Chapter 3, I used tools from graph theory to find evidence of chemical-specific patterns of activity in the *C. elegans* nervous system. This suggests that a graph-theoretic framework can reveal how interactions across a nervous system change in response to environmental stimuli, and potentially provides a cellular-level mechanism of information processing.

## 1.3 References


Adesnik H, Bruns W, Taniguchi H, Huang ZJ, Scanziani M. (2012). A neural circuit for spatial summation in visual cortex. *Nature*. https://doi.org/10.1038/nature11526

Ahn YY, Jeong H, Kim BJ. (2006). Wiring cost in the organization of a biological neuronal network. *Physica A: Statistical Mechanics and Its Applications*. https://doi.org/10.1016/j.physa.2005.12.013

Ahrens MB, Li JM, Orger MB, Robson DN, Schier AF, Engert F, Portugues R. (2012). Brain-wide neuronal dynamics during motor adaptation in zebrafish. *Nature*. https://doi.org/10.1038/nature11057

Bargmann CI. (1998). Neurobiology of the Caenorhabditis elegans genome. In *Science*. https://doi.org/10.1126/science.282.5396.2028

Bargmann CI, Hartwieg E, Horvitz HR. (1993). Odorant-selective genes and neurons mediate olfaction in C. elegans. *Cell*. https://doi.org/10.1016/0092-8674(93)80053-H

Bassett DS, Greenfield DL, Meyer-Lindenberg A, Weinberger DR, Moore SW, Bullmore ET. (2010). Efficient physical embedding of topologically complex information processing networks in brains and computer circuits. *PLoS Computational Biology*, *6*(4). https://doi.org/10.1371/journal.pcbi.1000748

Bentley B, Branicky R, Barnes CL, Chew YL, Yemini E, Bullmore ET, Vértes PE, Schafer WR. (2016). The Multilayer Connectome of Caenorhabditis elegans. *PLoS Computational Biology*. https://doi.org/10.1371/journal.pcbi.1005283

Brendel W, Romo R, MacHens CK. (2011). Demixed principal component analysis. *Advances in Neural Information Processing Systems 24: 25th Annual Conference on Neural Information Processing Systems 2011, NIPS 2011*.

Briggman KL, Abarbanel HDI, Kristan WB. (2005). Optical imaging of neuronal populations during decision-making. *Science*. https://doi.org/10.1126/science.1103736

Chalasani SH, Chronis N, Tsunozaki M, Gray JM, Ramot D, Goodman MB, Bargmann CI. (2007). Dissecting a circuit for olfactory behaviour in Caenorhabditis elegans. *Nature*, *450*(7166), 63–70. https://doi.org/10.1038/nature06292

Chalasani SH, Kato S, Albrecht DR, Nakagawa T, Abbott LF, Bargmann CI. (2010). Neuropeptide feedback modifies odor-evoked dynamics in Caenorhabditis elegans olfactory neurons. *Nature Neuroscience*. https://doi.org/10.1038/nn.2526

Chalfie M, Sulston J, White J, Southgate E, Thomsom J, Brenner S. (1985). The neural circuit for touch sensitivity in Caenorhabditis elegans. *The Journal of Neuroscience*. https://doi.org/3981252

Chen BL, Hall DH, Chklovskii DB. (2006). Wiring optimization can relate neuronal structure and function. *Proceedings of the National Academy of Sciences of the United States of America*. https://doi.org/10.1073/pnas.0506806103

Chen TW, Wardill TJ, Sun Y, Pulver SR, Renninger SL, Baohan A, Schreiter ER, Kerr RA, Orger MB, Jayaraman V, Looger LL, Svoboda K, Kim DS. (2013). Ultrasensitive fluorescent proteins for imaging neuronal activity. *Nature*. https://doi.org/10.1038/nature12354

Churchland MM, Cunningham JP, Kaufman MT, Foster JD, Nuyujukian P, Ryu SI, Shenoy K V., Shenoy K V. (2012). Neural population dynamics during reaching. *Nature*. https://doi.org/10.1038/nature11129

Colizza V, Flammini A, Serrano MA, Vespignani A. (2006). Detecting rich-club ordering in complex networks. *Nature Physics*. https://doi.org/10.1038/nphys209

Constantin L, Poulsen RE, Favre-Bulle IA, Taylor MA, Sun B, Goodhill GJ, Vanwalleghem GC, Scott EK. (2019). Altered brain-wide auditory networks in fmr1-mutant larval zebrafish. *BioRxiv*, 722082. https://doi.org/10.1101/722082

Cunningham JP, Yu BM. (2014). Dimensionality reduction for large-scale neural recordings. In *Nature Neuroscience*. https://doi.org/10.1038/nn.3776

Eguíluz VM, Chialvo DR, Cecchi GA, Baliki M, Apkarian AV. (2005). Scale-free brain functional networks. *Physical Review Letters*. https://doi.org/10.1103/PhysRevLett.94.018102

Fu Y, Tucciarone JM, Espinosa JS, Sheng N, Darcy DP, Nicoll RA, Huang ZJ, Stryker MP. (2014). A cortical circuit for gain control by behavioral state. *Cell*. https://doi.org/10.1016/j.cell.2014.01.050

Glover GH. (2011). Overview of functional magnetic resonance imaging. In *Neurosurgery Clinics of North America*. https://doi.org/10.1016/j.nec.2010.11.001

Goodman MB, Hall DH, Avery L, Lockery SR. (1998). Active currents regulate sensitivity and dynamic range in C. elegans Neurons. *Neuron*. https://doi.org/10.1016/S0896-6273(00)81014-4

Gray JM, Hill JJ, Bargmann CI. (2005). A circuit for navigation in Caenorhabditis elegans. *Proceedings of the National Academy of Sciences of the United States of America*. https://doi.org/10.1073/pnas.0409009101

Guet CC, Elowitz MB, Hsing W, Leibler S. (2002). Combinatorial synthesis of genetic networks. *Science*. https://doi.org/10.1126/science.1067407

Hale LA, Lee ES, Pantazis AK, Chronis N, Chalasani SH. (2016). Altered Sensory Code Drives Juvenile-to-Adult Behavioral Maturation in Caenorhabditis elegans . *Eneuro*. https://doi.org/10.1523/eneuro.0175-16.2016

Hallquist MN, Hillary FG. (2018). Graph theory approaches to functional network organization in brain disorders: A critique for a brave new small-world. *Network Neuroscience*, *3*(1), 1–26. https://doi.org/10.1162/netn_a_00054

Hubel DH, Wiesel TN. (1959). Receptive fields of single neurones in the cat's striate cortex. *The Journal of Physiology*. https://doi.org/10.1113/jphysiol.1959.sp006308

Kaiser M, Hilgetag CC. (2006). Nonoptimal component placement, but short processing paths, due to long-distance projections in neural systems. *PLoS Computational Biology*. https://doi.org/10.1371/journal.pcbi.0020095

Kashtan N, Alon U. (2005). Spontaneous evolution of modularity and network motifs. *Proceedings of the National Academy of Sciences of the United States of America*. https://doi.org/10.1073/pnas.0503610102

Kato S, Kaplan HS, Schrödel T, Skora S, Lindsay TH, Yemini E, Lockery S, Zimmer M. (2015). Global Brain Dynamics Embed the Motor Command Sequence of Caenorhabditis elegans. *Cell*. https://doi.org/10.1016/j.cell.2015.09.034

Landman BS, Russo RL. (1971). On a Pin Versus Block Relationship For Partitions of Logic Graphs. *IEEE Transactions on Computers*. https://doi.org/10.1109/T-C.1971.223159

Lanzerotti MY, Fiorenza G, Rand RA. (2005). Predicting interconnect requirements in ultra-large-scale integrated control logic circuitry. *International Workshop on System Level Interconnect Prediction, SLIP*. https://doi.org/10.1145/1053355.1053366

Lee SH, Dan Y. (2012). Neuromodulation of Brain States. In *Neuron*. https://doi.org/10.1016/j.neuron.2012.09.012

Leinwand SG, Chalasani SH. (2013). Neuropeptide signaling remodels chemosensory circuit composition in Caenorhabditis elegans. *Nature Neuroscience*, *16*(10), 1461–1467. https://doi.org/10.1038/nn.3511

Leinwand SG, Yang CJ, Bazopoulou D, Chronis N, Srinivasan J, Chalasani SH. (2015). Circuit mechanisms encoding odors and driving aging-associated behavioral declines in Caenorhabditis elegans. *ELife*. https://doi.org/10.7554/eLife.10181

Liu Q, Kidd PB, Dobosiewicz M, Bargmann CI. (2018). C. elegans AWA Olfactory Neurons Fire Calcium-Mediated All-or-None Action Potentials. *Cell*. https://doi.org/10.1016/j.cell.2018.08.018

Marquez-Legorreta E, Constantin L, Piber M, Favre-Bulle IA, Taylor MA, Vanwalleghem GC, Scott E. (2019). Brain-wide visual habituation networks in wild type and fmr1 zebrafish. *BioRxiv*. https://doi.org/10.1101/722074

Meunier D, Lambiotte R, Fornito A, Ersche KD, Bullmore ET. (2009). Hierarchical modularity in human brain functional networks. *Frontiers in Neuroinformatics*. https://doi.org/10.3389/neuro.11.037.2009

Milo R, Shen-Orr S, Itzkovitz S, Kashtan N, Chklovskii D, Alon U. (2002). Network motifs: Simple building blocks of complex networks. *Science*. https://doi.org/10.1126/science.298.5594.824

Nakai J, Ohkura M, Imoto K. (2001). A high signal-to-noise ca2+ probe composed of a single green fluorescent protein. *Nature Biotechnology*. https://doi.org/10.1038/84397

Newman M. (2010). Networks: An Introduction. In *Networks: An Introduction*. https://doi.org/10.1093/acprof:oso/9780199206650.001.0001

Nichols ALA, Eichler T, Latham R, Zimmer M. (2017). A global brain state underlies C. Elegans sleep behavior. *Science*. https://doi.org/10.1126/science.aam6851

Nicosia V, Vértes PE, Schafer WR, Latora V, Bullmore ET. (2013). Phase transition in the economically modeled growth of a cellular nervous system. *Proceedings of the National Academy of Sciences of the United States of America*. https://doi.org/10.1073/pnas.1300753110

Nienborg H, Hasenstaub A, Nauhaus I, Taniguchi H, Josh Huang Z, Callaway EM. (2013). Contrast dependence and differential contributions from somatostatin- and parvalbumin-expressing neurons to spatial integration in mouse V1. *Journal of Neuroscience*. https://doi.org/10.1523/JNEUROSCI.5320-12.2013

O'Donnell LJ, Westin CF. (2011). An introduction to diffusion tensor image analysis. In *Neurosurgery Clinics of North America*. https://doi.org/10.1016/j.nec.2010.12.004

Papo D, Zanin M, Martínez JH, Buldú JM. (2016). Beware of the small-world neuroscientist! *Frontiers in Human Neuroscience*. https://doi.org/10.3389/fnhum.2016.00096

Pérez-Escudero A, De Polavieja GG. (2007). Optimally wired subnetwork determines neuroanatomy of Caenorhabditis elegans. *Proceedings of the National Academy of Sciences of the United States of America*. https://doi.org/10.1073/pnas.0703183104

Pérez-Escudero A, Rivera-Alba M, De Polavieja GG. (2009). Structure of deviations from optimality in biological systems. *Proceedings of the National Academy of Sciences of the United States of America*. https://doi.org/10.1073/pnas.0905336106

Ravasz E, Somera AL, Mongru DA, Oltvai ZN, Barabási AL. (2002). Hierarchical organization of modularity in metabolic networks. *Science*. https://doi.org/10.1126/science.1073374

Reigl M, Alon U, Chklovskii DB. (2004). Search for computational modules in the C. elegans brain. *BMC Biology*. https://doi.org/10.1186/1741-7007-2-25

Sales-Pardo M, Guimerà R, Moreira AA, Nunes Amaral LA. (2007). Extracting the hierarchical organization of complex systems. *Proceedings of the National Academy of Sciences of the United States of America*. https://doi.org/10.1073/pnas.0703740104

Scholz M, Linder AN, Randi F, Sharma AK, Yu X, Shaevitz JW, Leifer A. (2018). Predicting natural behavior from whole-brain neural dynamics. *BioRxiv*. https://doi.org/10.1101/445643

Schrödel T, Prevedel R, Aumayr K, Zimmer M, Vaziri A. (2013). Brain-wide 3D imaging of neuronal activity in Caenorhabditis elegans with sculpted light. *Nature Methods*. https://doi.org/10.1038/nmeth.2637

Simon HA. (1962). The Architecture of Complexity. *Proceedings of the American Philosophical Society*, *106*(6), 467–482. http://www.jstor.org/stable/985254

Skora S, Mende F, Zimmer M. (2018). Energy Scarcity Promotes a Brain-wide Sleep State Modulated by Insulin Signaling in C. elegans. *Cell Reports*. https://doi.org/10.1016/j.celrep.2017.12.091

Sperry MM, Telesford QK, Klimm F, Bassett DS. (2017). Rentian scaling for the measurement of optimal embedding of complex networks into physical space. *Journal of Complex Networks*. https://doi.org/10.1093/comnet/cnw010

Stopfer M, Jayaraman V, Laurent G. (2003). Intensity versus identity coding in an olfactory system. *Neuron*. https://doi.org/10.1016/j.neuron.2003.08.011

Supekar K, Musen M, Menon V. (2009). Development of large-scale functional brain networks in children. *PLoS Biology*. https://doi.org/10.1371/journal.pbio.1000157

Tenenbaum JB, De Silva V, Langford JC. (2000). A global geometric framework for nonlinear dimensionality reduction. *Science*. https://doi.org/10.1126/science.290.5500.2319

Towlson EK, Vértes PE, Ahnert SE, Schafer WR, Bullmore ET. (2013). The rich club of the C. elegans neuronal connectome. *Journal of Neuroscience*. https://doi.org/10.1523/JNEUROSCI.3784-12.2013

Tremblay R, Lee S, Rudy B. (2016). GABAergic Interneurons in the Neocortex: From Cellular Properties to Circuits. In *Neuron*. https://doi.org/10.1016/j.neuron.2016.06.033

van den Heuvel MP, Hulshoff Pol HE. (2010). Exploring the brain network: A review on resting-state fMRI functional connectivity. In *European Neuropsychopharmacology*. https://doi.org/10.1016/j.euroneuro.2010.03.008

Vanwalleghem G, Schuster K, Taylor MA, Favre-Bulle IA, Scott EK. (2020). Brain-wide mapping of water flow perception in zebrafish. *The Journal of Neuroscience*, JN-RM-0049-20. https://doi.org/10.1523/JNEUROSCI.0049-20.2020

Varier S, Kaiser M. (2011). Neural development features: Spatio-temporal development of the Caenorhabditis elegans neuronal network. *PLoS Computational Biology*. https://doi.org/10.1371/journal.pcbi.1001044

Varshney LR, Chen BL, Paniagua E, Hall DH, Chklovskii DB. (2011). Structural properties of the Caenorhabditis elegans neuronal network. *PLoS Computational Biology*. https://doi.org/10.1371/journal.pcbi.1001066

Wang J, Zuo X, He Y. (2010). Graph-based network analysis of resting-state functional MRI. In *Frontiers in Systems Neuroscience*. https://doi.org/10.3389/fnsys.2010.00016

Watts DJ, Strogatz SH. (1998). Collective dynamics of ‘small-world’ networks. *Nature*, *393*(6684), 440–442. https://doi.org/10.1038/30918

White JG, Southgate E, Thomson JN, Brenner S. (1986). The Structure of the Nervous System of the Nematode Caenorhabditis elegans. *Philosophical Transactions of the Royal Society B: Biological Sciences*. https://doi.org/10.1098/rstb.1986.0056

Williamson RC, Doiron B, Smith MA, Yu BM. (2019). Bridging large-scale neuronal recordings and large-scale network models using dimensionality reduction. In *Current Opinion in Neurobiology*. https://doi.org/10.1016/j.conb.2018.12.009

Yoshida K, Hirotsu T, Tagawa T, Oda S, Wakabayashi T, Iino Y, Ishihara T. (2012). Odour concentration-dependent olfactory preference change in C. elegans. *Nature Communications*, *3*. https://doi.org/10.1038/ncomms1750

Yu BM, Cunningham JP, Santhanam G, Ryu SI, Shenoy K V., Sahani M. (2009). Gaussian-process factor analysis for low-dimensional single-trial analysis of neural population activity. *Journal of Neurophysiology*. https://doi.org/10.1152/jn.90941.2008

Zaslaver A, Liani I, Shtangel O, Ginzburg S, Yee L, Sternberg PW. (2015). Hierarchical sparse coding in the sensory system of Caenorhabditis elegans. *Proceedings of the National Academy of Sciences of the United States of America*. https://doi.org/10.1073/pnas.1423656112

## 2. Evidence of Rentian Scaling of Functional Modules in Diverse Biological Networks

### 2.1 Abstract

Biological networks have long been known to be modular, containing sets of nodes that are highly connected internally. Less emphasis, however, has been placed on understanding how intermodule connections are distributed within a network. Here, we borrow ideas from engineered circuit design and study Rentian scaling, which states that the number of external connections between nodes in different modules is related to the number of nodes inside the modules by a power-law relationship. We tested this property in a broad class of molecular networks, including protein interaction networks for six species and gene regulatory networks for 41 human and 25 mouse cell types. Using evolutionarily defined modules corresponding to known biological processes in the cell, we found that all networks displayed Rentian scaling with a broad range of exponents. We also found evidence for Rentian scaling in functional modules in the *Caenorhabditis elegans* neural network, but, interestingly, not in three different social networks, suggesting that this property does not inevitably emerge. To understand how such scaling may have arisen evolutionarily, we derived a new graph model that can generate Rentian networks given a target Rent exponent and a module decomposition as inputs. Overall, our work uncovers a new principle shared by engineered circuits and biological networks.

## 2.2 Introduction

One approach to understand how biological networks are organized is to study their scaling properties. Developmental constraints often force evolution to conserve certain properties of networks as they change in size. By relating these properties to function, we can uncover new structure-function relationships. Here, we describe a new scaling relationship present in functional modules in diverse biological networks.

Molecular interaction networks are highly modular, containing subsets of nodes (genes or proteins) that interact more strongly with each other compared to the rest of the network (Spirin & Mirny, 2003; Sharan, Ulitsky, & Shamir, 2007; Navlakha, Schatz, & Kingsford, 2009; Jiang & Singh, 2010; Davis, Yaveroglu, Malod-Dognin, Stojmirovic, & Przulj, 2015). These modules represent core biological processes that occur in the cell, such as RNA metabolism, protein methylation, or autophagy (Ashburner et al., 2000). Although less studied, there are also many interactions between proteins in different modules (Pinkert, Schultz, & Reichardt, 2010), such as pleiotropic genes that have multiple functions and belong to multiple modules. These together suggest there is substantial cross-talk between biological modules, including across modules that are seemingly unrelated (Stearns, 2010). Here, our goal is to uncover structure in this intermodule communication using theories developed from engineered circuit design.

E. F. Rent, a scientist at IBM in the 1960s, studied the structure of computer circuits and found that when he plotted the number of gates (nodes) in a logical block (module) of the circuit versus the number of connections to or from that block, the two scaled according to a power law (Landman & Russo, 1971; Lanzerotti, Fiorenza, & Rand, 2005). This relationship, now known as Rent's rule, was preserved across many spatial scales,

from very small to very large modules, indicating that interconnections can be described by a self-similar function (Stevens, 2009). The rule has also been shown to hold over time as circuits evolved to become larger (more on-board components), more energy efficient, and higher performing (Bakoglu, 1990; Lanzerotti et al., 2005; Bassett et al., 2010).

The exponent of the power law relationship is called Rent's exponent. Higher exponents denote random, complex wiring, though with greater logical capacity; smaller values denote less capacity but a more economical design that prefers short-versus long-range connections (Christie & Stroobandt, 2000). Thus, the exponent encodes a trade-off between the economy of design and performance complexity. In digital circuits, the exponent is important because it can be used to predict the total amount of wiring needed to realize a specific design topology (Christie & Stroobandt, 2000), and thus how efficiently the network is embedded in space (Bullmore & Sporns, 2012). It can also be used to estimate various chip layout parameters (Christie & Stroobandt, 2000). Proteins in molecular networks do not have fixed positions in space, and thus there is no exact analog of "wiring length"; however, proteins are largely partitioned into physical cellular compartments, and thus Rent's exponent may provide insight into the efficiency of cross-compartment communication. Remarkably, circuit design engineers at IBM did not explicitly try to optimize for Rent's rule; it emerged naturally from the human design process. In molecular networks, a certain amount of independence of modules is clearly desired, yet the diameters of most molecular networks and signaling pathways are rather small, suggesting that intermodule connections are significant and useful for information integration (Mason & Verwoerd, 2007; Gitter, Klein-Seetharaman, Gupta, & Bar-Joseph, 2011; Deeds, Krivine, Feret, Danos, & Fontana, 2012; Navlakha, Gitter, & Bar-Joseph,

2012). This tradeoff between economy and complexity could also signify how disruption of one biological process affects another (closely or distantly related) biological process (Dillin, Gottschling, & Nystrom, 2014) and how efficiently these effects propagate throughout the network (Navlakha, He, Faloutsos, & BarJoseph, 2014).

In this work, we find evidence of Rentian scaling of functional modules in a diverse set of molecular and cellular networks, including physical protein interaction networks, cell-type specific gene regulatory networks, and neural circuits. In contrast to prior work testing Rentian scaling, which decomposed networks into topological modules using graph partitioning algorithms (Bassett et al., 2010; Klimm, Bassett, Carlson, & Mucha, 2014; Bullmore & Sporns, 2012), we decomposed networks into biological modules based on known functional annotations of nodes. This allowed us to test whether natural modules designed by evolution exhibited Rentian scaling in the same way that the human design process naturally led to Rentian scaling of engineered circuits. We find strong evidence in support of Rentian scaling, even when using different definitions of *biological module* and different protein interaction data sources for defining molecular networks. In gene regulatory networks, we also found that Rent's exponents in embryonic cells are significantly smaller than the exponents in differentiated cells, indicating that Rentian scaling may provide a useful network feature for understanding cellular maturation throughout development. We also find Rentian scaling in functional modules of the *C. elegans* neural network, but, interestingly, not in three social networks, implying that information processing may play a role in producing Rentian structure. Finally, to help explain how Rentian scaling may have emerged biologically, we derived a new evolutionary graph model to generate networks with a specified Rent's exponent. Overall,

our work describes a new principle of how intermodule edges are distributed within diverse biological networks.

## 2.3 Materials and Methods

### 2.3.1 Calculating the Rent's Exponent of a Network

As input, we are provided an undirected network $G = (V, E)$ and a decomposition of the nodes $V$ into $k$ modules, $M = (M_1, M_2, \ldots, M_k)$, where each $M_i \subset V$. An individual node can belong to multiple modules, and hence $M_i \cap M_j \neq \emptyset$, necessarily.

To compute the Rent's exponent $p$ for each network (see Figure 1), we calculated two numbers for each module $M_i$: the number of nodes inside the module ($n_i$), and the total number of external edges ($e_i$) from nodes in $M_i$ to nodes in other modules. This is straightforward to calculate, except in the case where modules overlap. For example, if node $x \in M_i$, $M_j$ and node $y \in M_j$, and if edge $(x,y) \in E$, then for $M_i$, the edge is counted as external, but for $M_j$, it is internal since both $x$ and $y$ belong to $M_j$. We then plot $n_i$ versus $e_i$ for all $i$ and test whether the following relationship between the two variables holds:

$$e = cn^p, \tag{2.1}$$

where $c$ is an integration constant equal to the average number of external connections per node.

The significance of this relationship was tested by plotting $n_i$ versus $e_i$ for all $i$ on a log-log scale, computing a regression line for the data using least squares, and then computing the coefficient of determination ($R^2$) for the line. Following Bassett et al. (2010), we removed modules that contained more than $N/2$ nodes, where $N$ equals the number of nodes in the network, in order to avoid the Region II boundary effects of Rentian plots,

where a single module contains most of the nodes in a network. We also excluded nodes that appeared solely in these larger modules. This Region II has been observed in physical and topological partitions for a network (Christie & Stroobandt, 2000), and in VLSI chips, it refers to the fact that there is a limited number of input-output terminals at the boundary of the chip (Landman & Russo, 1971; Bassett et al., 2010). Nonetheless, it is clear from Figures 3, 4, and 5 that a lower threshold may be needed, as there still appears to be a plateau or turning down of the scaling relationship for modules with a large number of nodes.

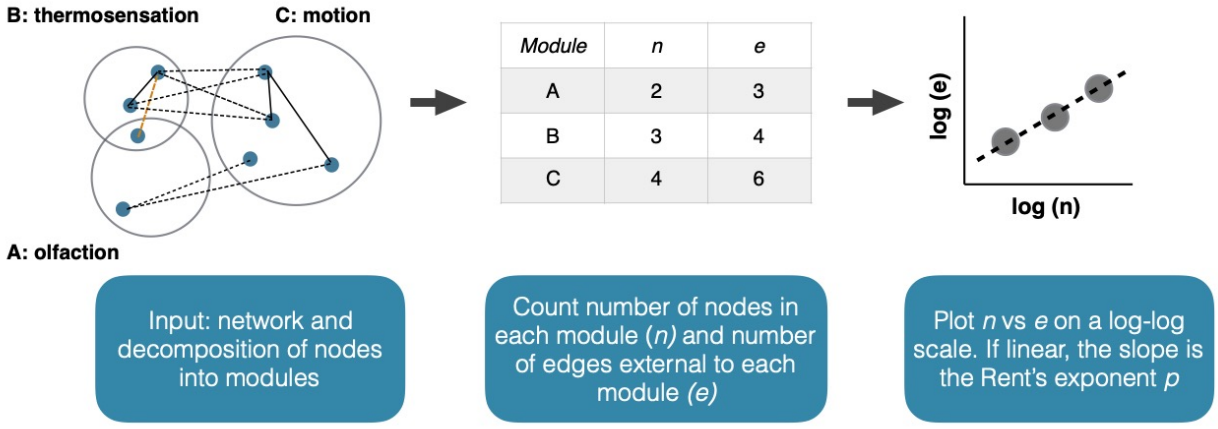


Figure 2.1 Computing the Rent's exponent of a network. (Left) The input is a network and a decomposition of the nodes into modules. Solid and dotted lines denote internal and external edges, respectively. The orange dotted line is considered an external edge for module A and an internal edge for module B. (Middle) Count the number of nodes in each module ($n$) and the number of external edges from nodes in that module to nodes in other modules ($e$). (Right) Plot $n$ versus $e$ on a log-log scale. If linear, the slope of the line is the Rent's exponent.

If the points fall on a straight line on a log-log plot, the network exhibits Rentian scaling, with an exponent $0< p \leq 1$.Thus, $p$=1corresponds to a random arrangement of external connections, with no placement optimization (i.e., no preference between inter-

or intramodule connections). For digital circuits with a homogeneous layout, the smaller the value of *p*, the more efficiently the network is embedded (Christie & Stroobandt, 2000; Bassett et al., 2010), indicating a preference of economy over complexity. In functional modules in molecular networks, the embedding can correspond to a diffusion distance for proteins to find their correct interaction partners, with smaller values of *p* indicating a preference for local interactions.

Testing Rentian scaling requires a network to be decomposed into modules (M). Prior work has defined these modules using the topology of the network (Bassett et al., 2010), for example, by recursively bipartitioning the network using graph cuts (Karypis, Aggarwal, Kumar, & Shekhar, 1999) and computing Rent's exponent using modules at all levels in the hierarchy. However, one downside of this approach is that a graph clustering method needs to be selected, and this method might implicitly bias toward modules that display Rentian scaling. An alternative approach for networks that are physically embedded in space is to randomly place randomly sized "boxes" onto the network; each box corresponds to a module and includes all the nodes it covers (Yang, Bozorgzadeh, & Sarrafzadeh, 2001; Bassett et al., 2010). This is also undesirable for us because most proteins diffuse and do not have fixed positions in space. Here, we depart from both of these approaches and instead define modules biologically (instead of topologically), based on the known cellular function of individual nodes. Specifically, a biological module contains a set of genes or proteins that takes part in the same biological process within the cell, such as RNA metabolism, protein methylation, or autophagy. Assigning genes/proteins to modules is largely done independently from network topology, often based on a battery of experimental assays, including gene knockout

experiments and expression data on transcript levels in different conditions. These natural modules also range across many sizes, which is important to test any scaling rule. Critically, this approach allows us to test whether evolution-defined modules exhibit Rentian scaling similar to how the human design process naturally led to Rentian scaling of digital circuits.

#### 2.3.1.1 Network Randomization to Test Rentian Scaling

To determine whether a network's Rent's exponent was not due to chance alone, for each network we compared its empirical Rent's exponent with three random controls. We reason that any given network that follows Rent's rule should, if randomized, have a larger Rent's exponent, as found by Bassett et al. (2010). We repeated each type of randomization 100 times and then compared each network's empirical and random Rent's exponents using a one-sample two-tailed *t*-test. The controls were generated as follows:

1. *Random modules*. We selected two random nodes *u* and *v* and for each listed the modules they do not share in common. Assuming these two lists are not empty, we then randomly selected one module in each list (call them $m_u$ and $m_v$ ) with probability proportional to the size of the module, so that larger modules were more likely to be randomized. We then moved *u* into $m_v$ and *v* into $m_u$. This procedure ensured that module affiliations are randomized, but the distribution of module sizes remains the same as in the empirical network. We swapped nodes $\sum n_i$ times (i.e., the sum of the number of nodes in every module) and calculated Rent's exponent with the new modules. We repeated this procedure 100 times and report the average Rent's exponent. The edges remain unchanged for this control.

2. *Random edges*. We performed a standard edge-swapping procedure that preserves the degree distribution: we selected two edges ($u$, $v$) and ($x$, $y$) and swapped their end points to create ($u$, $y$) and ($v$, $x$), assuming neither of the new edges already exists. We swapped pairs of edges $|E|$ times, where $|E|$ is the number of edges in the network, and then computed Rent's exponent. We repeated this procedure 100 times and report the average Rent's exponent. The modules remain unchanged for this control.
3. *Random both*. We first randomized the modules and then randomized the edges.

In all randomization procedures, we fixed $c$ (the average number of external connections per node) to the value found in the corresponding empirical network; otherwise, the change in slope was masked by a change in this value.

#### 2.3.1.2 Methodological Limitations

One novelty of this study is that we use functional, not topological, modules to partition the networks we studied. This approach, however, comes with some limitations. First, graph partitioning approaches used previously (e.g., hMetis used by Bassett et al., 2010) can be used to study modules over different scales of the topological hierarchy that allow one to study fractal and other forms of scaling (Song, Havlin, & Makse, 2005). We studied a functional hierarchy; in the Gene Ontology, we find modules that vary over one to two orders of magnitude, with larger modules corresponding to broader biological processes (e.g., cellular physiological process) and smaller sized modules corresponding to more specific processes (e.g., pyrimidine metabolic process). The Gene Ontology,

however, is not structured as a tree but rather as a directed acyclic graph, which does not provide clear distinctions between levels. Furthermore, there has been extensive prior work in developing graph partitioning methods to extract topological modules from protein interaction networks that can be used to predict protein function (Brohee & van Helden, 2006; Navlakha et al., 2009; Song & Singh, 2009; Sharan et al., 2007); however, success largely depends on the partitioning algorithm used. Thus, it may be difficult to compare insights from topological and functional analyses. Second, nodes (e.g., proteins) in our networks do not have fixed positions in physical space, but rather diffuse more broadly in cellular components. These compartments do provide a coarse physical embedding of nodes, but the embedding is within a limited physical region as opposed to a static position. Thus, further work is needed to relate Rent's exponents to typical notions of wiring economy and embedding when proteins can diffuse within limited physical regions. Third, Rentian scaling was originally developed to study nonoverlapping logic blocks (modules); in using functional modules, a node can be assigned to many modules, which may modify the interpretation of Rent's exponent. Fourth, the networks studied here are binary, whereas many biological networks also have weights indicating the strength or the confidence of interactions.

### 2.3.2 An Evolutionary Algorithm to Generate Rentian Networks

Here, our goal is to derive a simple, biologically feasible graph model that could generate networks that display Rentian scaling. Formally, the problem is as follows:

*Given:* A set of nodes $V$, a decomposition of $V$ into modules $M$, and a target Rent's exponent $p$

*Find:* A graph $G = (V, E)$ with Rent's exponent $\approx p$, computed using the modules $M$

Our goal is to develop a generative model to define the edges connecting the given nodes in $V$ . Contrary to most generative graph models (Leskovec, Kleinberg, & Faloutsos, 2005; Barabási & Albert, 1999; Watts & Strogatz, 1998; Vázquez, Flammini, Maritan, & Vespignani, 2003) and prior work in Rentian scaling (Klimm et al., 2014), our problem formulation includes a module decomposition as input used to compute Rent's exponent. The modules are used as input so that we can use the same decomposition and target Rent's exponent of any empirical network, which ensures that a solution exists and allows for a direct comparison between the synthetic and real networks.

Duplication-divergence represents one common biological mechanism used to evolve molecular networks. Below, we describe a standard model for this process (called DMC) followed by our extension of this model (called DSC) that uses the same duplication principle but better captures Rentian properties of biological networks. We generated an ensemble of 100 DMC and 32 DSC networks. We generated only 32 DSC networks because of the time required to generate networks with an extra parameter (namely, $q_{fav}$). We then generated 100 DSC networks for the best parameter combination for each species in order to better compare the DMC and DSC networks. The results we describe are averages over the ensemble.

#### 2.3.2.1 The Duplication-Mutation with Complementarity Model (DMC)

In this model (Vázquez et al., 2003), an existing gene (node *u*) duplicates to initially form a topologically equivalent node (*v*). Then their set of common interaction partners diverges, indicating subspecialization of the two genes. These two processes, duplication and divergence, are controlled by two parameters: $q_{mod}$ and $q_{con}$. Specifically, after each duplication step, each common neighbor *x* of *u* and v is retained independently by both *u* and v with probability $1 - q_{mod}$; with probability $q_{mod}$, either (*u*, *x*) or (*v*, *x*) is removed, with equal probability. Then, with probability $q_{con}$ , an edge (*u*, *v*) is added between the duplicates. This model has been extensively validated in terms of its ability to reproduce many known topological features of protein interaction networks (Middendorf, Ziv, & Wiggins, 2005; Navlakha & Kingsford, 2011; Navlakha, Faloutsos, & Bar-Joseph, 2015), yet it does not use or incorporate any module decomposition in its growth procedure.

In each step of the model, we choose one random unconnected node (*u*, the "new" node) and a random node that already joined the network (*v*, the "anchor" node), and copy *v* to *u* by applying the DMC procedure described above. We iterated this process until all nodes joined the network.

#### 2.3.2.2 The Duplication-Specialization with Complementarity Model (DSC)

To directly incorporate the module decomposition into the growth procedure, we created the DSC model (see Figure 2). This model differs from DMC in two ways:

1. *We introduced a module-aware parameter, $q_{fav}$, used in the duplication step.* With probability $q_{fav}$, the anchor node *v* is selected randomly from a module in which the new node *u* lies (instead of randomly from the entire network in DMC). This is

motivated by the biological observation that duplicated nodes retain some functional association with their ancestral node (Wagner, 2001; Pereira-Leal & Teichmann, 2005); $q_{fav}$ allows us to model this variability. Due to module overlap, even if $q_{fav} = 1$, there may still be external edges between modules.

2. *We modified the divergence procedure.* If an edge to neighbor $x$ is chosen to diverge, then instead of randomly selecting which edge ($u$, $x$) or ($v$,$x$) to delete, we deterministically delete the edge depending on which node ($u$ or $v$) has fewer modules in common with $x$. In other words, if $u$ and $x$ have fewer modules in common than $v$ and $x$, then edge ($u$,$x$) is deleted. This represents the specialization of duplicated proteins observed by Nasvall, Sun, Roth, and Andersson (2012) and agrees with the observation by Zinman, Zhong, and BarJoseph (2011) that interactions between proteins in the same module are more likely to be conserved than interactions between proteins in different modules. Thus, when choosing which edge will diverge, the DSC model takes into account the module overlap with the neighbor in question, whereas DMC merely flips a coin.

An illustration of the DSC model is shown in Figure 2. Pseudocode of the model is shown in algorithm 1.

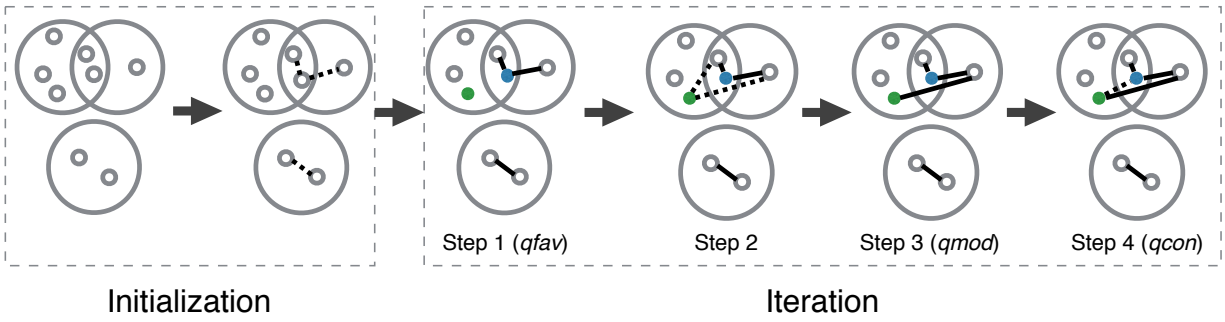


Figure 2.2 Duplication-specialization with complementarity (DSC) model. (Left) To initialize, we connect two random nodes in each module; some nodes may be chosen more than once because modules overlap. (Right) Step 1: We select a "new" node $u$ (green) and an "anchor" node $v$ (blue) from which $u$ duplicates. With probability $q_{fav}$, the anchor node is selected from a module shared with $u$. Step 2: Neighbors of $v$ are copied onto $u$. Step 3: For each common neighbor $x$, with probability $1 - q_{mod}$, both edges $(u, x)$ and $(v, x)$ are retained; with probability $q_{mod}$, $(u,x)$ is deleted if $u$ and $x$ share fewer modules than $v$ and $x$, or vice versa. Step 4: The two duplicated nodes are connected with probability $q_{con}$. This procedure is repeated until all nodes join the network.

**Algorithm 1:** DSC ($M$, $q_{con}$, $q_{mod}$, $q_{fav}$)

```
G = Graph()       # Initialize empty graph.
for all m ∈ M do
    u = m.random_node()
    v = m.random_node()
    G.add_edge(u,v)     # Start with dumbbell in each module.
end for

V_C = set of connected nodes
V_U = set of unconnected nodes

while |V_U| > 0 do
    u = V_U.pop_random_node()
    M_u = set of modules that u is in
    M_rest = set of modules that u is not in

    #1. Module-aware duplication.
    if rand() < q_fav then
        m = M_u.random_module()
    else
        m = M_rest.random_module()
    end if
    m_C = m ∩ V_C # Set of connected nodes in m
    v = m_C.random_node()

    G.copy_node(v,u)    # Duplicate v to u.
    for all x ∈ G.neighbors(v) do
        #2. Neighbor divergence.
        Overlap_u = number of modules shared by x and u
        Overlap_v = number of modules shared by x and v
        if rand() < q_mod then
            if Overlap_u < Overlap_v then
                G.delete_edge(u,x)
            else
                G.delete_edge(v,x)
            end if
        end if
    end for

    #3. Duplicate interaction.
    if rand() < q_con then
        G.add_edge(v,u)
    end if
end while
return G
```

### 2.3.3 Data sets

#### 2.3.3.1 Protein interaction networks

We downloaded protein-protein interactions (PPIs) from BioGRID version 3.4.141 for six species: *M. musculus*, *S. pombe*, *H. sapiens*, *A. thaliana*, *D. melanogaster*, and *S. cerevisiae* (Stark et al., 2006). We removed all interactions that were genetic, between genes in different organisms, or found using AffinityCapture RNA or Protein-RNA assays. We annotated each protein to all significantly enriched Biological Process GO terms using GOTermFinder (Boyle et al., 2004). We excluded annotations that were inferred electronically (IEA annotations). We set a *p*-value cutoff of 1 to find all associated GO terms for each protein (Boyle et al., 2004). The items on the list of GO terms and their associated *p*-values were then supplied to REVIGO to group GO terms into semantic clusters, which allowed us to exclude overly redundant modules (Supek et al., 2011). We used three values for the semantic cutoff parameter in REVIGO—0.5, 0.7, and 0.9—in order to test the robustness of our analysis against modules of varying sizes and degrees of overlap. When we did not use REVIGO, for computing the Rent plots, we averaged the number of external edges for every module of the same size, as done before (Stroobandt, 1998).

We also analyzed Rentian scaling in PPIs from the STRING database v10, which collects interactions from several sources and assigns each one a confidence score (Szklarczyk et al., 2015). We kept only interactions that were annotated as “binding” (physical interactions) and had a score greater than or equal to 700 (high confidence). We used FlyBase version FB2016_05 to convert the protein IDs for *D. melanogaster* from the format used by STRING to one usable by GOTermFinder (Attrill et al., 2016). We used

bioDBnet's db2db tool to convert the proteins IDs for *H. sapiens* and *M. musculus* from their Ensembl Protein ID format to Gene Symbol, which could be used in GOTermFinder (Mudunuri, Che, Yi, & Stephens, 2009). We also removed proteins that began with "LOC" and picked the first Gene Symbol when several were provided for one Ensembl Protein ID. We then used GOTermFinder to annotate the nodes, and REVIGO at three different cutoffs to reduce semantic redundancy.

#### 2.3.3.2 Social and Information Networks

The Amazon network was described in the main text. The DBLP network represented scientific collaborations between authors (nodes) who have coauthored a paper (edges). Here, publication venues (conferences) serve as the modules (communities). These modules are highly overlapping (Yang & Leskovec, 2015), much like the PPI networks, and yet they fail to display Rentian scaling. The YouTube social network was taken from January 2007, where users (nodes) were connected to other users they were friends with (edges). Modules in this network were user-defined groups. For all three networks, only the top 5000 highest-quality modules were used, where each module was assigned a score that corresponded to an average of four goodness metrics that mathematically describe how module-like it was (Yang & Leskovec, 2015).

## 2.4 Results

First, we asked if three classes of biological networks (molecular, gene regulatory, and neural) and two classes of nonbiological networks (information and social) exhibit

Rentian scaling. Second, we evaluated the ability of two generative graph models (DMC and DSC) to recapitulate Rentian properties for the biological networks studied.

### 2.4.1 Molecular Networks Demonstrate Rentian Scaling

We collected protein-protein interaction (PPI) networks for six species from BioGRID (Stark et al., 2006; see section 2.3.3.1): *Drosophila melanogaster* (fly), *Homo sapiens* (human), *Mus musculus* (mouse), *Arabidopsis thaliana* (plant), *Schizosaccharomyces pombe* (fission yeast), and *Saccharomyces cerevisiae* (baker's yeast). We assigned each protein in the network to modules based on the protein's known annotations under the Biological Process ontology in the Gene Ontology database (GO; Ashburner et al., 2000). Each module represents a biological process; all proteins annotated to that biological process are assigned to the module. These annotations are largely determined using biological assays, such as gene knockout experiments, that did not include network topology as a criteria.

To test Rent's rule for modules over a range of sizes, we selected nonredundant GO annotations from all levels of the GO hierarchy using REVIGO (Supek, Bosnjak, Skunca, & Smuc, 2011). REVIGO uses a clustering algorithm to find one GO annotation (module) that represents many semantically similar GO annotations. Semantic similarity accounts for how close a pair of GO annotations is to its lowest common ancestor in the GO hierarchy (Schlicker, Domingues, Rahnenfuhrer, & Lengauer, 2006). A userdefined cutoff parameter can be used to vary the number and semantic overlap of annotations. The resulting sizes of modules varied by an order of magnitude, for example, from 174 to 1803 nodes per module for *M. musculus* at a REVIGO cutoff of 0.7. There was also

significant module overlap (pleiotropy), with nodes belonging to an average of 12.5 modules (*S. pombe*) to 35.8 modules (*M. musculus*), with the other species lying in between.

We found that all six PPI networks displayed Rentian scaling—each least-squares regression line achieved an $R^2 > 0.75$—with Rent's exponents ranging from 0.591 for mouse to 0.860 for human (see Figure 3). This means that as modules contain more nodes, they have more external connections in accordance with a power law, indicating that a single scaling rule can capture the distribution of intermodule connections for modules of many sizes.

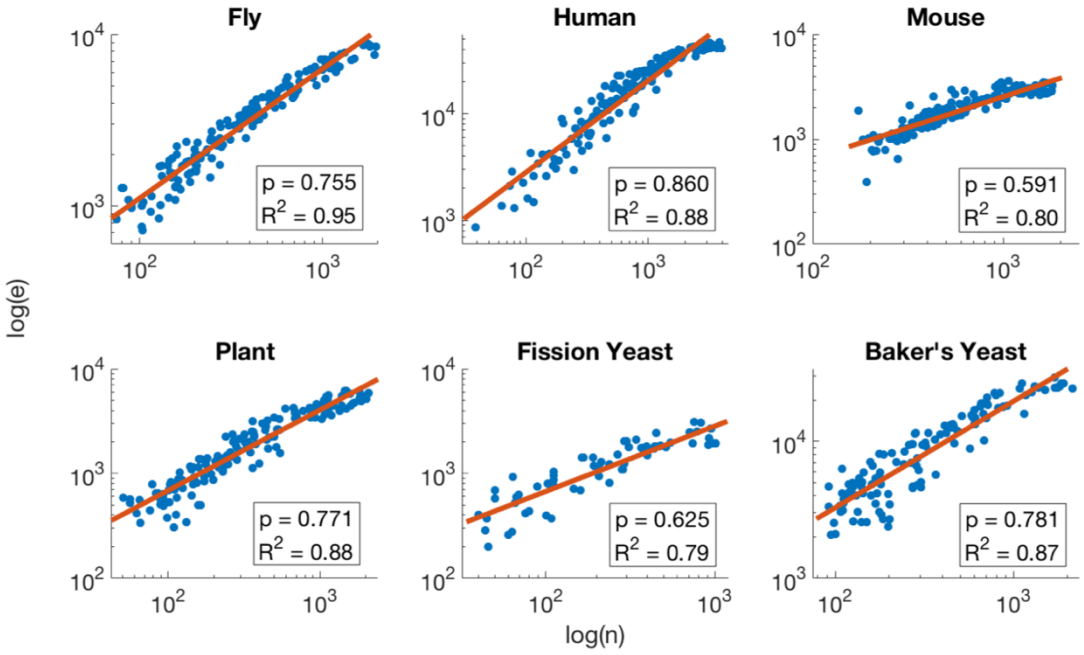


Figure 2.3 Molecular networks exhibit Rentian scaling. Rent's exponents for protein interaction networks of six species with REVIGO cutoff of 0.7. The *x*-axis is the log of the number of nodes (*n*), and the *y*-axis is the log of the number of external edges (*e*) from that module to other modules. All networks display Rentian scaling, with the Rent's exponent *p* shown in the legend.

We also found a strong positive correlation between the number of edges in the network and the Rent's exponent ($R$ = 0.80, over all species), suggesting that larger networks tend to increase cross-module communication, as opposed to increasing intramodularity. Moreover, all randomized controls produced Rent's values that were significantly higher than the empirical Rent's exponent observed for the real network (see Table 1). Randomizing both edges and modules consistently produced networks with larger Rent's exponents than randomizing either modules or edges alone (see Table 1). There was, however, no clear pattern when comparing Rent's exponents when we randomize either edges or modules; in half the species, the former produced lower Rent's exponents, whereas the opposite was true in the other species. While some of these differences may appear small, they are differences in log-space, and they mimic the range of differences observed in prior Rentian analysis of brain networks (Bassett et al., 2010).

Table 2.1 Rent's Exponents for PPI Networks and the *C. elegans* Neural Network. All Rent's exponents are significantly smaller than each of the corresponding randomized controls ($p < 0.01$, one- sample two-tailed *t*-test). Values in parentheses are $R^2$.

| Species | Number of Nodes | Number of Modules | Number of Edges | REVIGO | Rent's Exponent | Random Modules | Random Edges | Random Both |
|---|---|---|---|---|---|---|---|---|
| Fly | 4544 | 95 | 18,791 | 0.5 | 0.742 (0.94) | 0.751 (0.97) | 0.751 (0.96) | 0.754 (0.97) |
| | 4585 | 171 | 18,952 | 0.7 | 0.755 (0.95) | 0.764 (0.97) | 0.765 (0.96) | 0.767 (0.97) |
| | 4589 | 280 | 18,981 | 0.9 | 0.762 (0.95) | 0.770 (0.97) | 0.772 (0.96) | 0.774 (0.97) |
| Human | 9615 | 87 | 102,292 | 0.5 | 0.845 (0.86) | 0.869 (0.92) | 0.857 (0.88) | 0.873 (0.92) |
| | 9656 | 158 | 102,884 | 0.7 | 0.860 (0.88) | 0.881 (0.93) | 0.873 (0.90) | 0.886 (0.92) |
| | 9657 | 305 | 102,895 | 0.9 | 0.868 (0.88) | 0.886 (0.93) | 0.880 (0.90) | 0.891 (0.93) |
| Mouse | 3796 | 96 | 7047 | 0.5 | 0.565 (0.76) | 0.582 (0.83) | 0.582 (0.86) | 0.588 (0.86) |
| | 3817 | 185 | 7068 | 0.7 | 0.591 (0.80) | 0.607 (0.83) | 0.607 (0.88) | 0.613 (0.87) |
| | 3820 | 292 | 7072 | 0.9 | 0.604 (0.80) | 0.620 (0.81) | 0.620 (0.87) | 0.626 (0.86) |
| Plant | 5390 | 79 | 15,556 | 0.5 | 0.762 (0.88) | 0.781 (0.97) | 0.784 (0.93) | 0.788 (0.97) |
| | 5418 | 158 | 15,606 | 0.7 | 0.771 (0.88) | 0.789 (0.97) | 0.792 (0.93) | 0.796 (0.97) |
| | 5418 | 280 | 15,606 | 0.9 | 0.770 (0.90) | 0.786 (0.97) | 0.791 (0.94) | 0.793 (0.97) |
| Fission yeast | 2030 | 53 | 6943 | 0.5 | 0.561 (0.81) | 0.605 (0.94) | 0.612 (0.92) | 0.614 (0.95) |
| | 2030 | 73 | 6943 | 0.7 | 0.625 (0.79) | 0.669 (0.93) | 0.674 (0.90) | 0.680 (0.93) |
| | 2030 | 109 | 6943 | 0.9 | 0.674 (0.77) | 0.719 (0.91) | 0.727 (0.87) | 0.733 (0.91) |
| Baker's yeast | 4743 | 92 | 65,775 | 0.5 | 0.770 (0.86) | 0.802 (0.94) | 0.791 (0.90) | 0.806 (0.94) |
| | 4747 | 124 | 65,810 | 0.7 | 0.781 (0.87) | 0.810 (0.95) | 0.802 (0.91) | 0.816 (0.95) |
| | 4759 | 202 | 66,056 | 0.9 | 0.825 (0.87) | 0.853 (0.94) | 0.846 (0.90) | 0.859 (0.93) |
| Worm | 239 | 8 | 1612 | — | 0.859 (0.97) | 0.950 (0.95) | 0.920 (0.99) | 0.960 (0.95) |

#### 2.4.1.1 Robustness to Different Module Decompositions

We tested the robustness of this observation in two ways. First, we varied the cutoff parameter in REVIGO to generate module decompositions with fewer (cutoff = 0.5) and greater (cutoff = 0.9) numbers of modules. In both cases, we observed similar Rent's exponents for each species, which continued to be significantly lower than randomized controls (see Table 1). Rent's exponents generally increased as the number of modules increased for all species.

Second, we assigned proteins to all modules in the entire GO Biological Process hierarchy (we kept semantically redundant modules) using the GoTermFinder tool (Boyle et al., 2004). This increased the range of module sizes to over four orders of magnitude, and it produced even more highly overlapping modules; for example, each node belonged to an average of 41.3 modules in *S. pombe* and 106.7 modules in *M. musculus*. This extensive amount of module overlap increased the number of cross-module connections; thus, all Rent's exponents increased, but we still observed Rentian scaling over separate hierarchical levels of every PPI network (see Table 2 and Figure 4).

These tests together demonstrate that Rentian scaling in PPIs is robust to different definitions of a module and extent of module overlap.

Table 2.2 Rentian Scaling Using All Modules Assigned from GOTermFinder. All Rent's exponents are smaller than that of the randomized controls ($p < 0.01$, one-sample two-tailed *t*-test). Values in parentheses are $R^2$.

| Species | Number of Nodes | Number of Modules | Number of Edges | Rent's Exponent | Random Modules | Random Edges | Random Both |
|---|---|---|---|---|---|---|---|
| Fly | 7174 | 4539 | 31,948 | 0.880 (0.93) | 0.882 (0.94) | 0.884 (0.93) | 0.886 (0.94) |
| Human | 13,400 | 9744 | 134,638 | 0.887 (0.84) | 0.896 (0.87) | 0.894 (0.85) | 0.901 (0.87) |
| Mouse | 4159 | 8971 | 7659 | 0.809 (0.88) | 0.821 (0.88) | 0.820 (0.89) | 0.826 (0.89) |
| Plant | 7486 | 3520 | 25,715 | 0.917 (0.90) | 0.927 (0.95) | 0.932 (0.92) | 0.935 (0.95) |
| Fission yeast | 2477 | 2942 | 8248 | 0.846 (0.80) | 0.886 (0.89) | 0.884 (0.84) | 0.898 (0.89) |
| Baker's yeast | 4866 | 3861 | 66,749 | 0.907 (0.83) | 0.934 (0.89) | 0.930 (0.86) | 0.940 (0.88) |

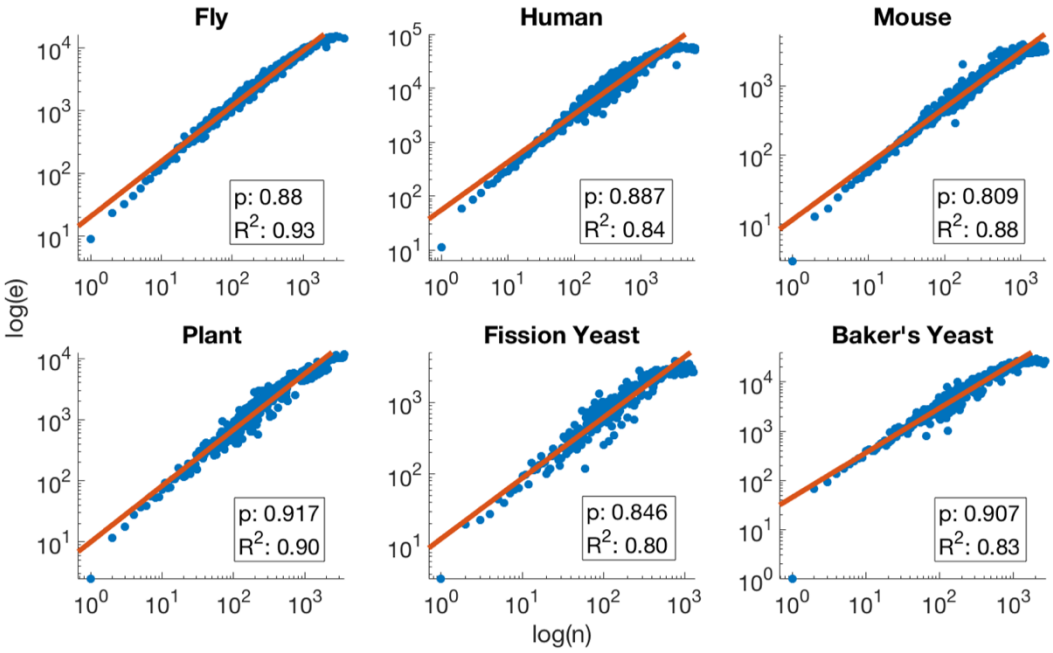


Figure 2.4 Rentian scaling using GOTermFinder. PPIs from six species display Rentian scaling, even when using overlapping modules defined by several thousand GO terms.

#### 2.4.1.2 Robustness to Different Data Sources

Protein interaction networks are notoriously noisy and incomplete (Bader, Chaudhuri, Rothberg, & Chant, 2004; Huang & Bader, 2009), affecting the conclusions that can be drawn from their analyses. To generate an alternative set of interactions, we used the STRING database, which collects interactions over a broader range of data sources (Szklarczyk et al., 2015; see section 2.3.3.1). We considered physical "binding interactions" only with a confidence score greater than 700 to minimize noise. We again used REVIGO at three different cutoffs to define modules and found that these networks continued to display Rentian scaling (see Figure 5 and Table 3), further suggesting that Rentian scaling is a robust and conserved property of PPI networks. Of note, when the STRING database is used, the human PPI network has a much lower $R^2$ value compared

to other species and compared to the full human PPI network (see Table 1). This discrepancy may be due to the substantially fewer nodes in the high-confidence STRING human PPI network (~3300) versus in the full human PPI network (~9600). This reduction suggests that there are many human PPIs yet to be mapped at a high-confidence level, leaving the network more incomplete compared to other species. It could also suggest that human PPI networks simply do not exhibit Rentian scaling.

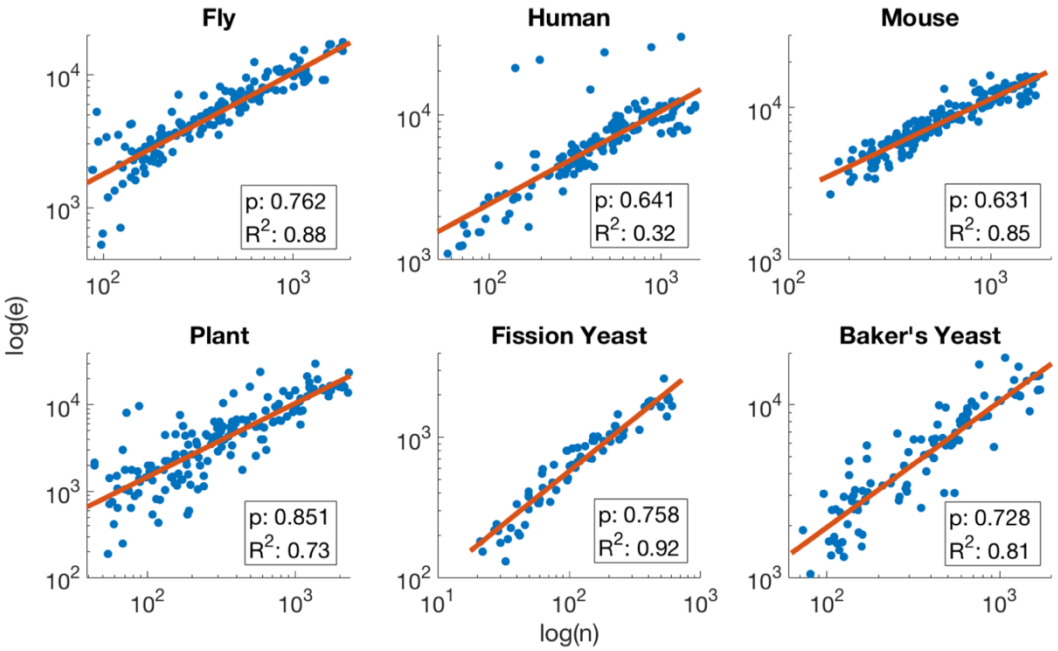


Figure 2.5 Rentian scaling using STRING. PPIs from six species display Rentian scaling, even when using the high-confidence networks with a score greater than or equal to 700 from the STRING database and a REVIGO cutoff of 0.7. Note the low $R^2$ for the Human network, which may be due to many missing proteins and interactions when compared to the BioGRID network.

Table 2.3 PPIs for Six Different Species from the STRING Database Also Display Rentian Scaling. All Rent's exponents are smaller than that of the randomized controls ($p < 0.01$, one-sample two-tailed *t*-test). Values in parentheses are $R^2$.

| Species | Number of Nodes | Number of Modules | Number of Edges | REVIGO | Rent Exponent | Random Modules | Random Edges | Random Both |
|---|---|---|---|---|---|---|---|---|
| Fly | 4010 | 100 | 41,052 | 0.5 | 0.812 (0.85) | 0.864 (0.97) | 0.858 (0.91) | 0.872 (0.96) |
| | 4055 | 176 | 41,186 | 0.7 | 0.762 (0.87) | 0.808 (0.97) | 0.805 (0.92) | 0.817 (0.97) |
| | 4055 | 281 | 41,186 | 0.9 | 0.771 (0.87) | 0.815 (0.97) | 0.813 (0.91) | 0.824 (0.97) |
| Human | 3344 | 79 | 81,481 | 0.5 | 0.615 (0.22) | 0.707 (0.97) | 0.710 (0.50) | 0.731 (0.98) |
| | 3347 | 144 | 81,503 | 0.7 | 0.641 (0.32) | 0.723 (0.98) | 0.735 (0.65) | 0.752 (0.98) |
| | 3347 | 277 | 81,503 | 0.9 | 0.636 (0.33) | 0.710 (0.98) | 0.730 (0.62) | 0.742 (0.98) |
| Mouse | 3530 | 86 | 40,871 | 0.5 | 0.614 (0.84) | 0.645 (0.98) | 0.653 (0.95) | 0.659 (0.99) |
| | 3551 | 175 | 41,097 | 0.7 | 0.631 (0.85) | 0.661 (0.98) | 0.667 (0.95) | 0.674 (0.98) |
| | 3552 | 294 | 41,100 | 0.9 | 0.644 (0.85) | 0.670 (0.98) | 0.678 (0.95) | 0.683 (0.98) |
| Plant | 5404 | 95 | 73,304 | 0.5 | 0.853 (0.76) | 0.941 (0.96) | 0.905 (0.82) | 0.951 (0.96) |
| | 5404 | 173 | 73,304 | 0.7 | 0.851 (0.73) | 0.939 (0.96) | 0.901 (0.83) | 0.949 (0.96) |
| | 5404 | 283 | 73,304 | 0.9 | 0.839 (0.69) | 0.913 (0.96) | 0.885 (0.80) | 0.924 (0.96) |
| Fission Yeast | 1329 | 60 | 9333 | 0.5 | 0.762 (0.92) | 0.903 (0.96) | 0.864 (0.94) | 0.918 (0.96) |
| | 1329 | 83 | 9333 | 0.7 | 0.758 (0.92) | 0.881 (0.97) | 0.852 (0.95) | 0.899 (0.97) |
| | 1329 | 121 | 9333 | 0.9 | 0.781 (0.9) | 0.895 (0.97) | 0.880 (0.95) | 0.918 (0.97) |
| Baker's Yeast | 4034 | 76 | 47,175 | 0.5 | 0.751 (0.78) | 0.831 (0.95) | 0.812 (0.88) | 0.841 (0.95) |
| | 4043 | 108 | 47,355 | 0.7 | 0.728 (0.81) | 0.806 (0.95) | 0.787 (0.90) | 0.816 (0.95) |
| | 4048 | 175 | 47,405 | 0.9 | 0.757 (0.81) | 0.826 (0.96) | 0.818 (0.90) | 0.839 (0.95) |

#### 2.4.1.3 Comparison of Rent's Exponents Using Functional versus Topological Modules

Conventional analyses have used topological modules instead of functional modules to derive Rent's exponents. Here, we compared the exponents generated by the two approaches. To derive topological modules, we used hMetis (Bassett et al., 2010; Karypis et al., 1999), which recursively bipartitions the graph to minimize the number of edges between partitions. This procedure resulted in 11 to 13 hierarchical levels of partitions across the different PPI networks. The average number of nodes and external degrees in a partition at a given hierarchical level were plotted on a log-log scale, and the slope of the line was defined as the topological Rent's exponent. The Rent's exponents ranged from 0.74 to 1.04 for mouse and human, respectively, and the $R^2$ values ranged from 0.25 to 0.85 for human and fission yeast, respectively (see Table 4). The Rent's exponents from the topological modules were always larger than those for the functional modules at all REVIGO cutoff values and for every species, which implies more random wiring in the topological modules. Further, in five out of six networks, the fits were poorer. Thus, Rentian scaling in PPIs seems to be better defined using functional, not topological, modules.

The differences in Rent's exponents observed between topological modules and functional modules could be attributed to several factors. First, there are numerous graph-theoretic algorithms to partition networks, and it is not clear which definition of *topological module* makes the most biological sense. While hMetis is commonly used in the Rent community, recent work has shown that the Markov clustering algorithm (Enright, Van Dongen, & Ouzounis, 2002; Brohee & van Helden, 2006) and graph-summarization-

based approaches (Navlakha et al., 2009) produce the highest correlation between topological and functional modules in PPI networks useful for protein function prediction. These methods, however, do not return hierarchical modules, which is important in order to test Rentian scaling across scales. Second, PPI networks are notoriously noisy, with many spurious interactions and false negatives that obfuscate the true modules. Thus, we focused our study here on more ground-truth modules, based on known functional annotations. There are also some limitations in using functional modules (see section 2.3.1.2).

Table 2.4 PPIs for Six Species Using Topological Modules Display Poorer Rentian Scaling. All Rent's exponents are larger and $R^2$ fits are poorer from topological modules derived from hMetis (v.1.5.3) compared to those derived using functional modules (except for Fission Yeast, where the fit is higher with topological modules).

| Species | REVIGO | Rent Exponent | $R^2$ |
|---|---|---|---|
| Fly | 0.5 | 0.907 | 0.78 |
| | 0.7 | 0.882 | 0.77 |
| | 0.9 | 0.869 | 0.91 |
| Human | 0.5 | 0.826 | 0.34 |
| | 0.7 | 1.039 | 0.25 |
| | 0.9 | 0.943 | 0.24 |
| Mouse | 0.5 | 0.679 | 0.98 |
| | 0.7 | 0.744 | 0.77 |
| | 0.9 | 0.915 | 0.87 |
| Plant | 0.5 | 0.745 | 0.80 |
| | 0.7 | 0.753 | 0.83 |
| | 0.9 | 0.816 | 0.72 |
| Fission Yeast | 0.5 | 0.667 | 0.85 |
| | 0.7 | 0.844 | 0.85 |
| | 0.9 | 0.857 | 0.84 |
| Baker's Yeast | 0.5 | 0.726 | 0.67 |
| | 0.7 | 0.964 | 0.61 |
| | 0.9 | 0.906 | 0.78 |

### 2.4.2 Analysis of Cell-Type Specific Regulatory Networks

We collected cell-type-specific regulatory interactions for 41 human and 25 mouse cell lines (Neph et al., 2012; Stergachis et al., 2014) to test if Rentian scaling also appears in transcriptional networks. Nodes in these networks correspond to genes, and an edge exists between two genes if one regulates the transcription of the other. Each of the 66 networks contained interactions that occur within only one specific cell type (e.g., fetal brain, hepatoblastoma, and embryonic stem cells). Using REVIGO-defined modules, we found that all cell-type-specific networks displayed Rentian scaling, with exponents ranging from 0.795 to 0.937 (mouse; see Table 5) and 0.843 to 0.921 (human; see Table 6). The largest of the Rent's exponents were attributed to immune and cancer cells.

We also found that embryonic stem cells (ESCs) had significantly lower Rent's exponents than differentiated cells in both species (see Figure 6). Unlike the PPI networks, where more interactions correlated with significantly higher Rent's exponents, the opposite was true here: ESCs contained more interactions than other cell types (17, 883 ± 3518 for ESCs versus 14, 810 ± 3522 for differentiated cells in mouse) yet had lower Rent's exponents (see Figure 6). This suggests that as a cell develops and defines its functional identity, its Rent's exponent increases by eliminating more intramodule edges than intermodule edges. Thus, one signature of cellular differentiation may be changes in the distribution of intermodule connections, from less to more intermodule cross-talk as the cell matures, an observation consistent with the balanced lineage specifier hypothesis (Loh & Lim, 2011).

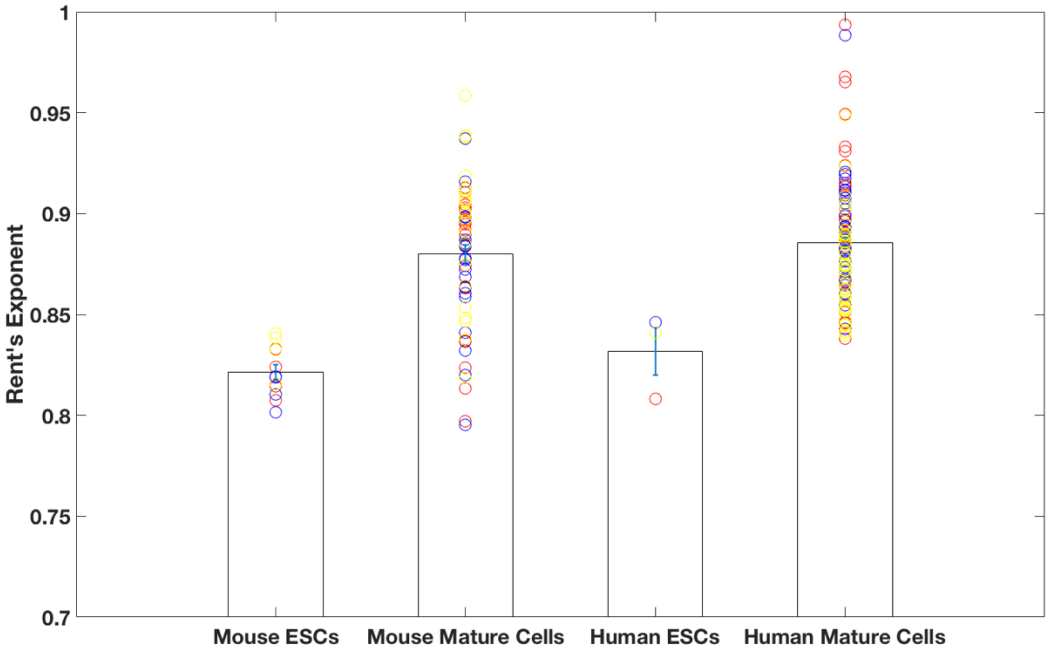


Figure 2.6 Embryonic stem cells (ESCs) exhibit a lower Rent's exponent than differentiated cells. The average Rent's exponent for ESCs was lower than that of mature cells in both mice and humans. Bars are standard error of the mean, and circles are the Rent's exponents for individual cell lines with modules defined by REVIGO at three cutoffs. The three different colors for the circles denote the three REVIGO cutoffs (red = 0.5, blue = 0.7, yellow = 0.9). Differences in Rent's exponents between ESCs and non-ESCs in a given species are statistically significant across all REVIGO values ($p < 0.01$, two-sample two-tailed *t*-test) and within individual cutoffs ($p < 0.01$,two-sample Kolmogorov-Smirnov test for mouse at REVIGO values of 0.5, two-sample two-tailed *t*-tests for mouse at REVIGO values of 0.7 and 0.9, and one-sample two-tailed *t*-tests for human because the latter had just one ESC line).

Table 2.5 Mouse Regulatory Networks Demonstrate Rentian Scaling. Only results for a REVIGO cutoff of 0.7 are shown. Similar results hold for other REVIGO cutoffs of 0.5 and 0.9. Values in parentheses are $R^2$. [a]Rows correspond to ESCs. [b]Rows correspond to cancer cell lines. [c]Rows correspond to immune cells.

| Cell line | Number of Nodes | Number of Modules | Number of Edges | Rent Exponent | Random Modules | Random Edges | Random Both |
|---|---|---|---|---|---|---|---|
| mfBrain-DS14536 | 503 | 121 | 18524 | 0.795 (0.92) | 0.798 (0.94) | 0.795 (0.92) | 0.798 (0.94) |
| ZhBTc4-DS15236[a] | 504 | 119 | 22248 | 0.802 (0.94) | 0.803 (0.95) | 0.801 (0.94) | 0.803 (0.95) |
| ZhBTc4-DS17562[a] | 503 | 119 | 18631 | 0.810 (0.93) | 0.813 (0.94) | 0.810 (0.93) | 0.813 (0.94) |
| ZhBTc4-DS17616[a] | 503 | 119 | 16822 | 0.819 (0.92) | 0.823 (0.94) | 0.819 (0.92) | 0.822 (0.94) |
| mCJ7-DS13320[a] | 500 | 119 | 13832 | 0.819 (0.93) | 0.821 (0.95) | 0.819 (0.93) | 0.822 (0.95) |
| mRetina-DS20004 | 504 | 119 | 15963 | 0.820 (0.91) | 0.824 (0.94) | 0.82 (0.91) | 0.824 (0.94) |
| mHeart-DS18138 | 503 | 121 | 18867 | 0.832 (0.88) | 0.840 (0.93) | 0.832 (0.88) | 0.841 (0.93) |
| mGenitalFatPad-DS18182 | 504 | 119 | 24360 | 0.841 (0.90) | 0.847 (0.94) | 0.841 (0.90) | 0.848 (0.94) |
| mB-DS16168 | 496 | 117 | 15081 | 0.859 (0.86) | 0.867 (0.93) | 0.859 (0.87) | 0.868 (0.93) |
| m3134-DS8497[b] | 468 | 120 | 13763 | 0.861 (0.89) | 0.870 (0.93) | 0.861 (0.89) | 0.870 (0.93) |
| mLung-DS14479 | 500 | 120 | 18258 | 0.864 (0.88) | 0.874 (0.94) | 0.864 (0.88) | 0.874 (0.94) |
| mLiver-DS14605 | 490 | 120 | 10586 | 0.869 (0.85) | 0.881 (0.92) | 0.868 (0.85) | 0.881 (0.92) |
| mATn-DS17070[c] | 500 | 120 | 18768 | 0.872 (0.87) | 0.882 (0.94) | 0.872 (0.87) | 0.882 (0.94) |
| mNIH_3T3-DS16900[b] | 491 | 121 | 14025 | 0.877 (0.88) | 0.886 (0.93) | 0.877 (0.88) | 0.886 (0.93) |

Table 2.5 Mouse Regulatory Networks Demonstrate Rentian Scaling (continued).

| Cell line | Number of Nodes | Number of Modules | Number of Edges | Rent Exponent | Random Modules | Random Edges | Random Both |
|---|---|---|---|---|---|---|---|
| mKidney-DS13948 | 498 | 120 | 14593 | 0.878 (0.90) | 0.885 (0.94) | 0.878 (0.90) | 0.886 (0.94) |
| m416B-DS14099 | 490 | 118 | 12091 | 0.884 (0.85) | 0.895 (0.93) | 0.884 (0.85) | 0.896 (0.93) |
| mTN-DS16171[c] | 497 | 119 | 15013 | 0.884 (0.86) | 0.896 (0.93) | 0.884 (0.86) | 0.896 (0.93) |
| mThymus-DS18819[c] | 463 | 121 | 11336 | 0.885 (0.86) | 0.896 (0.93) | 0.885 (0.86) | 0.896 (0.93) |
| mTN-DS17080[c] | 492 | 122 | 15747 | 0.887 (0.87) | 0.898 (0.93) | 0.887 (0.87) | 0.898 (0.93) |
| mB-DS17866 | 451 | 117 | 9279 | 0.898 (0.84) | 0.909 (0.92) | 0.899 (0.84) | 0.910 (0.92) |
| MEL-DS13036[b] | 491 | 120 | 13449 | 0.898 (0.86) | 0.910 (0.93) | 0.899 (0.86) | 0.910 (0.93) |
| mATr-DS20149[c] | 496 | 118 | 14184 | 0.907 (0.85) | 0.919 (0.93) | 0.907 (0.85) | 0.920 (0.93) |
| mBrain-DS12727 | 483 | 120 | 10182 | 0.907 (0.87) | 0.915 (0.93) | 0.906 (0.87) | 0.915 (0.93) |
| mA20-DS16695[b] | 492 | 122 | 13382 | 0.916 (0.87) | 0.927 (0.93) | 0.916 (0.88) | 0.927 (0.94) |
| mTR-DS17864[c] | 488 | 119 | 13577 | 0.937 (0.84) | 0.950 (0.92) | 0.937 (0.84) | 0.950 (0.92) |

Table 2.6 Human Regulatory Networks Demonstrate Rentian Scaling. Only results for a REVIGO cutoff of 0.7 are shown. Similar results hold for other REVIGO cutoffs of 0.5 and 0.9. Values in parentheses are $R^2$. [a]Row corresponds to ESCs. [b]Rows correspond to cancer cell lines. [c]Rows correspond to immune cells.

| Cell line | Number of Nodes | Number of Modules | Number of Edges | Rent Exponent | Random Modules | Random Edges | Random Both |
|---|---|---|---|---|---|---|---|
| fLung-DS14724 | 322 | 87 | 6478 | 0.843 (0.91) | 0.856 (0.94) | 0.845 (0.91) | 0.856 (0.94) |
| hESCT0-DS11909[a] | 325 | 86 | 6244 | 0.846 (0.93) | 0.854 (0.94) | 0.848 (0.93) | 0.855 (0.94) |
| fHeart-DS12531 | 312 | 84 | 5115 | 0.855 (0.90) | 0.866 (0.93) | 0.856 (0.90) | 0.867 (0.93) |
| NHDF_Neo-DS11923 | 314 | 85 | 5415 | 0.859 (0.91) | 0.866 (0.94) | 0.861 (0.91) | 0.867 (0.94) |
| HPF-DS13390 | 321 | 86 | 5033 | 0.860 (0.90) | 0.875 (0.94) | 0.863 (0.90) | 0.876 (0.94) |
| HepG2-DS7764[b] | 298 | 83 | 4600 | 0.865 (0.90) | 0.874 (0.93) | 0.866 (0.90) | 0.874 (0.93) |
| HEEpiC-DS12763 | 317 | 85 | 5101 | 0.867 (0.89) | 0.881 (0.93) | 0.870 (0.89) | 0.881 (0.93) |
| NHLF-DS12829 | 318 | 86 | 5145 | 0.868 (0.90) | 0.884 (0.94) | 0.870 (0.90) | 0.884 (0.94) |
| HVMF-DS13981 | 318 | 86 | 5356 | 0.868 (0.91) | 0.880 (0.93) | 0.870 (0.90) | 0.881 (0.93) |
| HMVEC_LLy-DS13185 | 314 | 85 | 5445 | 0.869 (0.89) | 0.887 (0.93) | 0.873 (0.88) | 0.886 (0.93) |
| HFF-DS15115 | 309 | 88 | 4249 | 0.871 (0.90) | 0.883 (0.93) | 0.873 (0.90) | 0.883 (0.93) |
| HMVEC_dBlAd-DS13337 | 312 | 85 | 4699 | 0.872 (0.89) | 0.882 (0.93) | 0.875 (0.89) | 0.883 (0.93) |
| HMF-DS13368 | 320 | 86 | 4632 | 0.873 (0.90) | 0.885 (0.94) | 0.876 (0.89) | 0.886 (0.94) |
| HCF-DS12501 | 315 | 86 | 5090 | 0.876 (0.89) | 0.895 (0.93) | 0.878 (0.89) | 0.897 (0.93) |
| HMVEC_dBlNeo-DS13242 | 317 | 86 | 6031 | 0.881 (0.89) | 0.895 (0.93) | 0.883 (0.89) | 0.896 (0.93) |

Table 2.6 Human Regulatory Networks Demonstrate Rentian Scaling (continued).

| Cell line | Number of Nodes | Number of Modules | Number of Edges | Rent Exponent | Random Modules | Random Edges | Random Both |
|---|---|---|---|---|---|---|---|
| HSMM-DS14426 | 315 | 86 | 4761 | 0.881 (0.90) | 0.895 (0.93) | 0.884 (0.90) | 0.896 (0.94) |
| IMR90-DS13219 | 314 | 89 | 3828 | 0.881 (0.90) | 0.895 (0.94) | 0.882 (0.90) | 0.896 (0.93) |
| fBrain-DS11872 | 313 | 88 | 4254 | 0.881 (0.90) | 0.894 (0.93) | 0.882 (0.90) | 0.893 (0.93) |
| SkMC-DS11949 | 323 | 86 | 6025 | 0.881 (0.91) | 0.895 (0.94) | 0.882 (0.91) | 0.897 (0.94) |
| HAEpiC-DS12663 | 316 | 87 | 4620 | 0.882 (0.89) | 0.896 (0.92) | 0.884 (0.89) | 0.897 (0.92) |
| HPAF-DS13411 | 321 | 83 | 4715 | 0.883 (0.88) | 0.903 (0.92) | 0.884 (0.88) | 0.905 (0.92) |
| HAh-DS15192 | 322 | 84 | 5928 | 0.883 (0.89) | 0.901 (0.92) | 0.884 (0.89) | 0.902 (0.92) |
| SAEC-DS10518 | 310 | 86 | 3299 | 0.883 (0.89) | 0.891 (0.93) | 0.884 (0.89) | 0.892 (0.93) |
| NHA-DS12800 | 310 | 88 | 3070 | 0.883 (0.90) | 0.897 (0.93) | 0.884 (0.90) | 0.897 (0.93) |
| AoAF-DS13513 | 320 | 86 | 4898 | 0.887 (0.90) | 0.902 (0.93) | 0.889 (0.89) | 0.903 (0.93) |
| AG10803-DS12374 | 310 | 87 | 4140 | 0.890 (0.89) | 0.903 (0.93) | 0.893 (0.89) | 0.905 (0.93) |
| HCM-DS12599 | 317 | 85 | 5273 | 0.893 (0.89) | 0.908 (0.93) | 0.895 (0.89) | 0.908 (0.93) |
| HMVEC_dLyNeo-DS13150 | 316 | 86 | 5467 | 0.893 (0.89) | 0.912 (0.93) | 0.897 (0.89) | 0.914 (0.93) |
| NHDF_Ad-DS12863 | 318 | 86 | 4471 | 0.893 (0.91) | 0.906 (0.94) | 0.895 (0.91) | 0.907 (0.94) |
| HIPEpiC-DS12684 | 316 | 84 | 4291 | 0.899 (0.90) | 0.909 (0.93) | 0.900 (0.89) | 0.909 (0.93) |

Table 2.6 Human Regulatory Networks Demonstrate Rentian Scaling (continued).

| Cell line | Number of Nodes | Number of Modules | Number of Edges | Rent Exponent | Random Modules | Random Edges | Random Both |
|---|---|---|---|---|---|---|---|
| SKNSH-DS8482[b] | 298 | 86 | 4599 | 0.902 (0.88) | 0.919 (0.92) | 0.904 (0.88) | 0.920 (0.92) |
| CD34-DS12274 | 318 | 82 | 5894 | 0.905 (0.89) | 0.927 (0.92) | 0.908 (0.88) | 0.929 (0.93) |
| CD20-DS18208[c] | 315 | 85 | 5920 | 0.908 (0.89) | 0.931 (0.92) | 0.912 (0.88) | 0.930 (0.93) |
| HCPEpiC-DS12447 | 319 | 85 | 5001 | 0.910 (0.89) | 0.927 (0.92) | 0.912 (0.89) | 0.926 (0.92) |
| GM06990-DS7748[c] | 300 | 83 | 4545 | 0.911 (0.85) | 0.937 (0.91) | 0.914 (0.85) | 0.937 (0.91) |
| NB4-DS12543 | 319 | 86 | 6632 | 0.912 (0.90) | 0.930 (0.93) | 0.915 (0.90) | 0.929 (0.93) |
| HRCE-DS10666 | 309 | 87 | 3083 | 0.917 (0.89) | 0.933 (0.92) | 0.921 (0.89) | 0.936 (0.92) |
| HPdLF-DS13573 | 315 | 85 | 4362 | 0.917 (0.90) | 0.927 (0.93) | 0.918 (0.90) | 0.928 (0.93) |
| K562-DS9767 | 296 | 88 | 3100 | 0.920 (0.89) | 0.935 (0.93) | 0.923 (0.89) | 0.936 (0.93) |
| GM12865-DS12436[c] | 315 | 81 | 5223 | 0.921 (0.86) | 0.949 (0.92) | 0.923 (0.86) | 0.951 (0.92) |

### 2.4.3 Analysis of Neural, Social, and Information Networks

Next, we tested the generality of Rent's rule when applied to topology-independent module decompositions of other biological (neural) and nonbiological (social, information) networks.

Prior work has analyzed the Rentian properties of the *C. elegans* neural network (Bassett et al., 2010); however, here we applied a Rentian analysis based on a module decomposition defined by known functional annotations of neurons, as opposed to defining modules using a graph partitioning algorithm, as was previously done. Specifically, we obtained the neural network for *C. elegans* from WormAtlas (Varshney, Chen, Paniagua, Hall, & Chklovskii, 2011) and decomposed this network into eight natural modules, where each module contained neurons with the same function (Varshney et al., 2011). These functions were chemosensation, mechanosensation, nociception, thermosensation, proprioception, sensation of oxygen, olfaction, and motion. We found that the network displayed Rentian scaling ($R^2 = 0.97$), with a Rent's exponent of 0.859 (see Figure 7A), which was smaller than randomized controls (see Table 1). This exponent suggests two things. First, neural circuits have some preference for short-range over long-range connections, as supported by the wiring economy principle (Ramón y Cajal, 1899; Chklovskii, Schikorski, & Stevens, 2002; Rivera-Alba, Peng, de Polavieja, & Chklovskii, 2014), which states that wire is a commodity in space- and resource-constrained neural circuits (as in digital circuits). Second, due to the relatively high exponent, there is some deviation from this principle, as may be expected since intermodule connections are needed to integrate data from multiple neural types to determine appropriate behavioral responses (Perez-Escudero & de Polavieja, 2007).

Prior work found a lower Rent's exponent (0.74) when computed using random partitions in a physical placement of the neurons (Bassett et al., 2010). Thus, Rentian scaling appears robust, but the exponent is sensitive to the choice of module decomposition.

We then tested Rentian scaling on three social and information networks with ground-truth modules (Yang and Leskovec, 2015; Mislove, Marcon, Gummadi, Druschel, & Bhattacharjee, 2007). In the Amazon network, products (nodes) were linked to other products that were purchased together (edges). The modules represented groups of at least three products that share a common function, ascribed using predefined product categories (Yang & Leskovec, 2015). The Amazon network did not display Rentian scaling, as the log-log regression was not a straight line ($R^2$ = 0.11; see Figure 7B). We also tested the DBLP collaborations network and YouTube social groups network (see section 2.3.3.2), and found that neither exhibited Rentian scaling.

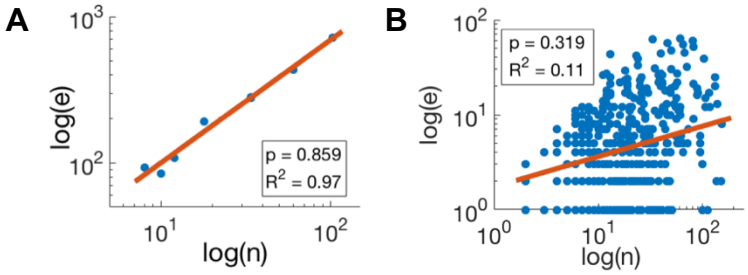


Figure 2.7 The *C. elegans* neural network displays Rentian scaling (A), but the Amazon product network does not (B). The $R^2$ for the worm neural network was 0.97; for the Amazon network, it was 0.11.

Together, these results suggest that Rentian scaling is not an inevitable consequence of any network developmental process. Further, many classes of random networks also do not exhibit Rentian behavior (Stroobandt, 2007; Klimm et al., 2014).

One hypothesis, then, is that Rentian scaling may be unique to information processing networks (e.g., digital circuits on a computer chip or biological circuits) and is derived implicitly by some general growth process, which we investigate next.

### 2.4.4 A Random Graph Model to Recapitulate Rentian Properties of Networks

The fact that Rentian scaling is found in molecular and cellular networks of several species and cell types indicates that this property may be a consequence of a common evolutionary process. We first tested whether a popular, existing generative graph model (DMC) could form networks that exhibit Rentian scaling while agnostic to the module decomposition. Overall, we found that DMC mostly failed in generating the empirical Rent's exponents of PPI networks, whereas our extended model (DSC) performed better, as described below. The DMC and DSC models are described in section 2.3.2.

To test each model's ability to generate Rentian networks, we used as input to the model the same set of nodes and their module decomposition from each PPI network, separately. The challenge was to recapitulate the Rentian properties for each PPI network by defining the edges. The synthetic, model-generated network "succeeded" in this regard if it: (A) it had a Rent's exponent within 0.04 of the empirical value; (B) contained within 10% of the number of edges as the empirical network; and (C) had a similar distribution of external edges per node as the empirical network. Attempting to lower the error rate of measure B resulted in an inability to match Rent's exponents for some networks; thus, more model parameters may be needed for a tighter fit. We tested all combinations of the three model parameters ($q_{mod}$, $q_{con}$, $q_{fav}$) with their values ranging from 0.1 to 0.9 in

intervals of 0.1. We report the results for the best parameter settings for each model in terms of measures A and B.

In the analysis of the ensemble, we found that the average DSC Rent's exponents were closer to the empirical Rent exponents than the DMC Rent's exponents across all species (see Figure 8A). In this figure, we selected the parameters that generated networks with the closest Rent's exponent to the empirical while abiding by the constraint on number of edges. Figure 8B shows example Rentian plots with the number of external edges averaged over the entire ensemble (the sizes of the modules remain the same across the ensemble). In all six species, the DSC model produced networks with more similar Rent's exponent and/or more similar number of edges as the empirical network, compared to DMC-grown networks. For example, when using the same set of nodes and module decomposition as the fly PPI network (see Table 7), there were 18,952 edges in the empirical network, 17,658 edges in the DSC network, and 19,289 edges in the DMC network. Furthermore, the DMC network had a Rent's exponent of 0.87, which was further away from the DSC and empirical networks' Rent's exponents of 0.78 and 0.76, respectively.

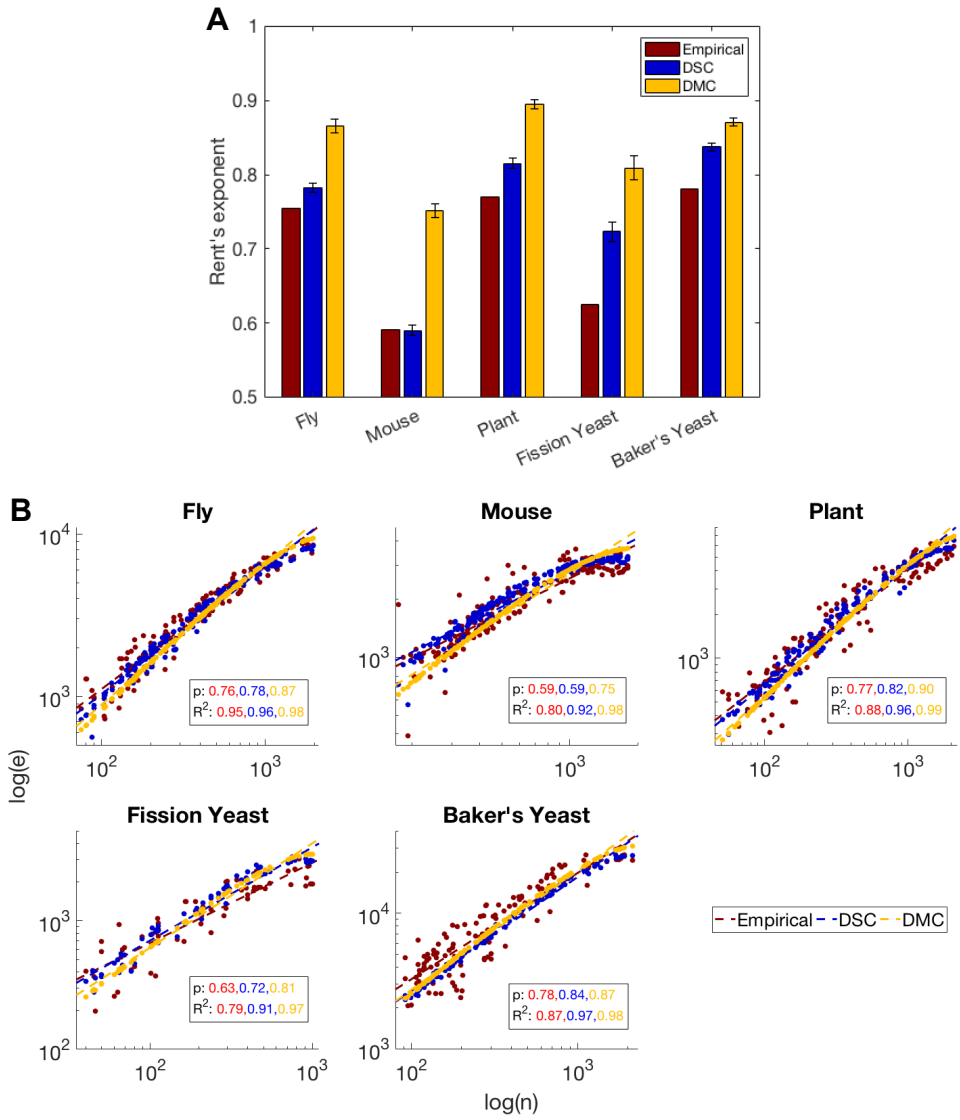


Figure 2.8 The DSC model better recapitulates the Rentian properties of real PPI networks compared to DMC. A) Compared to DMC, the DSC model generates networks with Rent's exponents closer to the empirical Rent's exponents of five PPI networks. Ensembles of networks were generated for each possible parameter combination for each model. Bars indicate mean Rent's exponent, and error bars represent standard deviations over the ensemble. We used the same nodes and module decomposition of each real PPI network (REVIGO cutoff of 0.7). B) Rent plots of networks generated by DMC and DSC (REVIGO cutoff of 0.7). Empirical data are shown in red, the DSC model is shown in blue, and the DMC model is shown in yellow. Each dot corresponds to one module. Ideal performance would be an exact overlap with the red data, indicating the same number of edges and the same Rent's exponent as the PPI network. Performance is shown for the best parameters for each model. Overall, the DSC line is closer than DMC to the empirical line across all species. The Rent's exponents (p) and fits ($R^2$) are shown in boxes.

Interestingly, the parameter settings for DSC that led to successful networks may highlight the relative roles of duplication and divergence during evolution. For all parameter values that generated successful networks (as defined above), $q_{mod}$ = 0.64 ± 0.09, $q_{con}$ = 0.63 ± 0.23, $q_{fav}$ = 0.53 ± 0.26. Prior studies have determined that $q_{mod}$ = 0.4 and $q_{con}$ = 0.7 produce networks that closely match other topological properties of the yeast PPI network (Navlakha & Kingsford, 2011; Navlakha et al., 2015); these parameters lie roughly within the range of best parameters we found, which further validates their use here.

We also found that the DSC model better reproduced the degree distribution of the number of external edges per node compared to DMC (see Table 7). This is a common metric used to evaluate the similarity between a real network and a synthetic network generated by a model. This measure (dubbed “homogeneity” by the Rentian community) is a common feature of digital circuits and suggests that the interconnect complexity of nodes is similar across modules of different sizes (Christie & Stroobandt, 2000). To quantify the similarity in degree distributions, we calculated the Kullback-Leibler (KL) divergence to compute the distance between homogeneity histograms, from empirical to DSC and from empirical to DMC. The KL distance from empirical to DSC was smaller than the distance from empirical to DMC in all species (e.g., 0.018 ± 0.002 versus 0.025 ± 0.003, respectively, for *D. melanogaster*), except for *S. pombe*, where the two distances were nearly identical. This further validates the ability of DSC to reproduce Rentian properties of real networks compared to DMC. There are numerous other measures used to establish the similarity between two networks (e.g., motifs, graphlets, random walk distributions, graph spectra). We do not claim that DSC is the definitive model in this

regard; rather, we show how a simple model based on established biological principles can capture a new feature (Rentian scaling) that future, more complex models should attempt to satisfy.

Table 2.7 The DSC Generative Model Better Recapitulates Key Characteristics of the Empirical Networks than the DMC Model. All values are means standard deviations from 100 network instantiations for the DMC and DSC models. KL Distance refers to the average Kullback-Leibler divergence of the number of external edges per node in a module from the PPI networks to 100 instantiations of DMC or DSC networks, plus or minus the standard deviation. Results here used a REVIGO cutoff of 0.7.

| Species | Rent's Exponent | Number of Edges | DMC Rent's Exponent | DMC Number of Edges | DMC KL Distance | DSC Rent's Exponent | DSC Number of Edges | DSC KL Distance |
|---|---|---|---|---|---|---|---|---|
| Fly | 0.755 | 18,952 | 0.866 ± 0.009 | 19,289 ± 1178 | 0.025 ± 0.003 | 0.783 ± 0.006 | 17,658 ± 446 | 0.018 ± 0.002 |
| Mouse | 0.591 | 7068 | 0.751 ± 0.010 | 7226 ± 234 | 0.033 ± 0.002 | 0.590 ± 0.006 | 6756 ± 132 | 0.026 ± 0.001 |
| Plant | 0.771 | 15,606 | 0.896 ± 0.006 | 14,724 ± 511 | 0.055 ± 0.004 | 0.815 ± 0.007 | 15,126 ± 267 | 0.041 ± 0.003 |
| Fission yeast | 0.625 | 6943 | 0.809 ± 0.016 | 6645 ± 464 | 0.089 ± 0.009 | 0.723 ± 0.014 | 7014 ± 239 | 0.087 ± 0.008 |
| Baker's yeast | 0.781 | 65,810 | 0.871 ± 0.006 | 63,787 ± 3887 | 0.060 ± 0.003 | 0.837 ± 0.005 | 60,010 ± 2359 | 0.053 ± 0.005 |

## 2.5 Discussion

We provided evidence that the structure of several molecular and cellular networks studied here is Rentian. While modularity has long been an appreciated facet of molecular networks, we find that these networks are “more than mere modules” (Pinkert et al., 2010), with significant structure in their intermodule connectivity. Inspired by theories developed from engineered digital circuits, we showed that Rentian scaling is a conserved property of several protein interaction networks and gene regulatory networks across multiple species and cell types; it also applies to functional modules in the *C. elegans* neural network but not to three social or information networks. Important to our work was testing this theory using module decompositions that were derived largely independently from network topology and instead by the underlying biology itself. This allowed us to test whether evolution converged onto biological modules with Rentian properties.

This power law relationship in module interconnects may aid in other applications, such as for function prediction tasks (Pinkert et al., 2010) or for ranking false or missing interactions in the network. Rentian scaling may also be used as a feature to discriminate between networks, especially across time. For instance, Sperry, Telesford, Klimm, and Bassett (2017) found that the present-day London Underground railroad displays Rentian scaling, but it did not in the year 1900. We found that regulatory networks for embryonic stem cells displayed Rentian scaling but that Rent’s exponents significantly increased with cellular development. Hence, the emergence of Rentian scaling, or the increase in Rent’s exponent, may provide another feature of how networks develop over time (Leskovec et al., 2005). Rentian scaling, however, cannot be trivially explained by changes in network density. For the PPIs, we found a positive correlation between Rent’s

exponent and network density; however, this relationship did not hold when PPIs were taken from the STRING database ($R$ = 0.80 and −0.05 for the full PPIs and those from STRING, respectively). Furthermore, in the regulatory networks, there was an inverse correlation between Rent's exponent and network density ($R$ = −0.64 and −0.26 for the mouse and human cell lines, respectively).

While this scaling law was persistent, exact interpretation of the Rent's exponent for an individual species may be muddled by the fact that protein interaction networks are still very noisy and incomplete. Although we attempted to account for this by studying networks derived from different data sources, it is difficult to determine whether the "true" Rent's exponents for these networks are higher or lower than the values derived here. Erroneous edges would likely count more as intermodule edges than intramodule edges; thus, removing noise may lower Rent's exponents. On the other hand, there are likely many missing edges between proteins in different modules, which might increase Rent's exponent when mapped. Our results here can serve as a benchmark for future studies as these networks continue to be mapped.

We also provided a new graph model (DSC) to generate graphs with a desired Rent's exponent, given a module decomposition. This model may be useful when designing synthetic biocircuits (Nielsen et al., 2016) or in other engineered network design applications. If a module decomposition is not available, one can use common network partitioning algorithms (Bassett et al., 2010), though there is no guarantee that these modules will be relevant to actual biological modules. Thus, an important contribution of this study is that Rentian scaling is found in networks decomposed into functional, not topological, modules and that the DSC model can build networks that exhibit Rentian

scaling using these modules. While our algorithm requires a module decomposition as input, a more sophisticated generator would also assign proteins to modules during the growth process. How to evolve such modularity is an important problem (Kashtan & Alon, 2005; Clune et al., 2013), but one that we do not consider here.

There may also be multiple mechanisms that can generate networks with Rentian scaling. The DSC graph model under a duplication model can produce Rentian networks. On the other hand, neither the London Underground railroad nor digital chips likely evolved using a duplication model, yet both demonstrate Rentian scaling (Sperry et al., 2017). Thus, while we posit a biological mechanism, we recognize that other mechanisms can produce Rentian scaling. Yet not every network growth mechanism generates Rentian networks. For example, the three social and information networks we studied likely did not evolve using a duplication model, and neither exhibited Rentian scaling. Thus, future work needs to better understand the theoretical basis underlying which mechanisms can produce Rentian networks and which cannot.

It is possible that mechanisms that produce Rentian networks are those constrained by a cost-performance trade-off. Proteins, for instance, must interact with specific partners with cognate structural domains. Proteins can also be sequestered into distinct cellular compartments (e.g., the nucleus), which limits the number of proteins with which they may interact. Neuronal circuits, similarly, are neither completely randomly wired nor minimally wired (Bassett et al., 2010). A biological network, then, must determine its topology by balancing cost and performance. Rentian scaling might be a by-product of these various constraints (i.e., a spandrel— Rubinov, 2016), and not an evolutionary adaptation. This would be consistent with our finding that Rentian scaling is

absent in three social and information networks, where the cost of making edges across any distance within the graph is likely to be much lower than in biological networks. Future work needs to provide a better theoretical basis for this observation.

Finally, how do the Rent's exponents calculated here compare with those observed in digital (e.g., VLSI) circuits? Mid- and large-sized circuits, taken from circuit repositories from the Microelectronics Center of North Carolina and IBM-PLACE (Alpert, 1998), display Rentian scaling with exponents ranging from 0.449 to 0.648 (Yang et al., 2001; Karypis et al., 1999). Another benchmark VLSI circuit, the ISCAS89 s953, had a higher Rent's exponent of 0.730 (Bassett et al., 2010). Overall, these computer circuits have Rent's exponents that are typically smaller than that of the PPI networks studied here. It has been observed that more recent complex circuits have higher Rent values compared to older designs (Bassett et al., 2010). We also observed that the Rent's exponent for the most complex organism studied, *H. sapiens*, was larger than that of the other species (see Table 1), though this may be coincidental.

Overall, the fact that both evolution and the human design process produced Rentian circuits suggests another close correspondence between biological and engineered networks (Navlakha & Bar-Joseph, 2011; Del Vecchio et al., 2016).

Chapter 2, in full, is a reprint of the material as it appears in Evidence of Rentian Scaling of Functional Modules in Diverse Biological Networks. How, Javier J.; Navlakha, Saket. Neural Computation, 2018. The dissertation author was the primary investigator and author of this paper.

## 2.6 References


Alpert CJ. ISPD98 circuit benchmark suite. In: Proceedings of the International Symposium on Physical Design. New York, NY, USA: ACM; 1998. p. 80–5.

Ashburner M, Ball CA, Blake JA, Botstein D, Butler H, Cherry JM, Davis AP, Dolinski K, Dwight SS, Eppig JT, Harris MA, Hill DP, Issel-Tarver L, Kasarskis A, Lewis S, Matese JC, Richardson JE, Ringwald M, Rubin GM, Sherlock G. Gene ontology: Tool for the unification of biology. Nat Genet. 2000 May;25(1):25–9.

Attrill H, Falls K, Goodman JL, Millburn GH, Antonazzo G, Rey AJ, Marygold SJ, FlybBase Consortium. FlyBase: Establishing a gene group resource for Drosophila melanogaster. Nucleic Acids Res. 2016 Jan;44(D1):D786–92.

Bader JS, Chaudhuri A, Rothberg JM, Chant J. Gaining confidence in high-throughput protein interaction networks. Nat Biotechnol. 2004 Jan;22(1):78–85.

Bainbridge D, y Cajal SR. Textura del Sistema Nervioso del Hombre y de los Vertebrados, 1899–1904. Vol. 2, Stripped Bare. Nicolas Moya; 2019. 216–219 p.

Barabási AL, Albert R. Emergence of scaling in random networks. Struct Dyn Networks. 2011;9781400841356(5439):349–52.

Bassett DS, Greenfield DL, Meyer-Lindenberg A, Weinberger DR, Moore SW, Bullmore ET. Efficient physical embedding of topologically complex information processing networks in brains and computer circuits. PLoS Comput Biol. 2010 Apr;6(4):e1000748.

Boyle EI, Weng S, Gollub J, Jin H, Botstein D, Cherry JM, Sherlock G. GO::TermFinder - Open source software for accessing Gene Ontology information and finding significantly enriched Gene Ontology terms associated with a list of genes. Bioinformatics. 2004 Dec;20(18):3710–5.

Brohée S, van Helden J. Evaluation of clustering algorithms for protein-protein interaction networks. BMC Bioinformatics. 2006;7(1):488.

Brohée S, van Helden J. Evaluation of clustering algorithms for protein-protein interaction networks. BMC Bioinformatics. 2006 Nov;7:488.

Chen BL, Hall DH, Chklovskii DB. Wiring optimization can relate neuronal structure and function. Proc Natl Acad Sci U S A. 2006 Mar;103(12):4723–8.

Chklovskii DB, Schikorski T, Stevens CF. Wiring optimization in cortical circuits. Neuron. 2002 Apr;34(3):341–7.

Christie P. Rent exponent prediction methods. IEEE Trans Very Large Scale Integr Syst. 2000;8(6):679–88.

Clune J, Mouret JB, Lipson H. Summary of the evolutionary origins of modularity. In: GECCO 2013 - Proceedings of the 2013 Genetic and Evolutionary Computation Conference Companion. 2013. p. 23.

Datta SR, Anderson DJ, Branson K, Perona P, Leifer A. Computational Neuroethology: A Call to Action. Vol. 104, Neuron. 2019. p. 11–24.

Datta SR, Anderson DJ, Branson K, Perona P, Leifer A. Computational Neuroethology: A Call to Action. Vol. 104, Neuron. 2019. p. 11–24.

Davis D, Yaveroğlu ÖN, Malod-Dognin N, Stojmirovic A, Pržulj N. Topology-function conservation in protein-protein interaction networks. Bioinformatics. 2015 May;31(10):1632–9.

Deeds EJ, Krivine J, Feret J, Danos V, Fontana W. Combinatorial complexity and compositional drift in protein interaction networks. PLoS One [Internet]. 2012;7(3):1–14. Available from: http://dx.doi.org/10.1371%2Fjournal.pone.0032032

Del Vecchio D, Densmore D, El-Samad H, Ingber D, Khalil AS, Kosuri S, Lander AD, Tang C. What Have the Principles of Engineering Taught Us about Biological Systems? Cell Syst. 2016 Jan;2(1):5–7.

Dillin A, Gottschling DE, Nyström T. The good and the bad of being connected: The integrons of aging. Curr Opin Cell Biol. 2014 Feb;26(1):107–12.

Enright AJ, Van Dongen S, Ouzounis CA. An efficient algorithm for large-scale detection of protein families. Nucleic Acids Res. 2002 Apr;30(7):1575–84.

Gitter A, Klein-Seetharaman J, Gupta A, Bar-Joseph Z. Discovering pathways by orienting edges in protein interaction networks. Nucleic Acids Res. 2011 Mar;39(4):e22.

Hu Q, Zhang ZG. MUI: A new functional similarity measure for gene products based on Gene Ontology. 3rd Int Conf Bioinforma Biomed Eng iCBBE 2009. 2009 Jun;7:302.

Huang H, Bader JS. Precision and recall estimates for two-hybrid screens. Bioinformatics. 2009 Feb;25(3):372–8.

Jiang P, Singh M. SPICi: A fast clustering algorithm for large biological networks. Bioinformatics. 2010 Apr;26(8):1105–11.

Jin Y, Turaev D, Weinmaier T, Rattei T, Makse HA. The Evolutionary Dynamics of Protein-Protein Interaction Networks Inferred from the Reconstruction of Ancient Networks. PLoS One. 2013;8(3):e58134.

Klimm F, Bassett DS, Carlson JM, Mucha PJ. Resolving Structural Variability in Network Models and the Brain. PLoS Comput Biol. 2014 Mar;10(3):e1003491.

Landman BS, Russo RL. On a Pin Versus Block Relationship For Partitions of Logic Graphs. IEEE Trans Comput. 1971 Dec;C–20(12):1469–79.

Lanzerotti MY, Fiorenza G, Rand RA. Microminiature packaging and integrated circuitry: The work of E. F. Rent, with an application to on-chip interconnection requirements. IBM J Res Dev. 2005 Jul;49(4–5):777–803.

Leskovec J, Kleinberg J, Faloutsos C. Graphs over time: Densification laws, shrinking diameters and possible explanations. In: Proceedings of the ACM SIGKDD International Conference on Knowledge Discovery and Data Mining. New York, NY, USA: ACM; 2005. p. 177–87.

Loh KM, Lim B. A precarious balance: Pluripotency factors as lineage specifiers. Cell Stem Cell. 2011 Apr;8(4):363–9.

Mason O, Verwoerd M. Graph theory and networks in biology. IET Syst Biol. 2007;1(2):89–119.

McDaid AF, Greene D, Hurley N. Normalized Mutual Information to evaluate overlapping community finding algorithms. 2011 Oct; Available from: http://arxiv.org/abs/1110.2515

Middendorf M, Ziv E, Wiggins CH. Inferring network mechanisms: The Drosophila melanogaster protein interaction network. Proc Natl Acad Sci U S A. 2005 Mar;102(9):3192–7.

Näsvall J, Sun L, Roth JR, Andersson DI. Real-time evolution of new genes by innovation, amplification, and divergence. Science (80- ). 2012 Oct;338(6105):384–7.

Navlakha S, Bar-Joseph Z. Algorithms in nature: The convergence of systems biology and computational thinking. Mol Syst Biol. 2011 Nov;7:546.

Navlakha S, Faloutsos C, Bar-Joseph Z. MassExodus: modeling evolving networks in harsh environments. Data Min Knowl Discov [Internet]. 2015;29(5):1211–32. Available from: http://dx.doi.org/10.1007/s10618-014-0399-1

Navlakha S, Gitter A, Bar-Joseph Z. A Network-based Approach for Predicting Missing Pathway Interactions. PLoS Comput Biol. 2012;8(8):e1002640.

Navlakha S, He X, Faloutsos C, Bar-Joseph Z. Topological properties of robust biological and computational networks. J R Soc Interface. 2014 Jul;11(96):20140283.

Navlakha S, Kingsford C. Network archaeology: Uncovering ancient networks from present-day interactions. PLoS Comput Biol. 2011 Apr;7(4):e1001119.

Navlakha S, Schatz MC, Kingsford C. Revealing biological modules via graph summarization. J Comput Biol. 2009 Feb;16(2):253–64.

Neph S, Stergachis AB, Reynolds A, Sandstrom R, Borenstein E, Stamatoyannopoulos JA. Circuitry and dynamics of human transcription factor regulatory networks. Cell. 2012 Sep;150(6):1274–86.

Nielsen AAK, Der BS, Shin J, Vaidyanathan P, Paralanov V, Strychalski EA, Ross D, Densmore D, Voigt CA. Genetic circuit design automation. Science (80- ). 2016 Apr;352(6281):aac7341.

Pereira-Leal JB, Teichmann SA. Novel specificities emerge by stepwise duplication of functional modules. Genome Res. 2005;15(4):552–9.

Pérez-Escudero A, De Polavieja GG. Optimally wired subnetwork determines neuroanatomy of Caenorhabditis elegans. Proc Natl Acad Sci U S A. 2007 Oct;104(43):17180–5.

Pinkert S, Schultz J, Reichardt J. Protein interaction networks-more than mere modules. PLoS Comput Biol. 2010 Jan;6(1):e1000659.

Reese TM, Brzoska A, Yott DT, Kelleher DJ. Analyzing Self-Similar and Fractal Properties of the C. elegans Neural Network. PLoS One. 2012;7(10):e40483.

Rivera-Alba M, Peng H, De Polavieja GG, Chklovskii DB. Wiring economy can account for cell body placement across species and brain areas. Curr Biol. 2014 Feb;24(3):R109--110.

Rivera-Alba M, Vitaladevuni SN, Mishchenko Y, Lu Z, Takemura SY, Scheffer L, Meinertzhagen IA, Chklovskii DB, de Polavieja GG. Wiring economy and volume exclusion determine neuronal placement in the drosophila. Curr Biol. 2012 Dec;22(2):172.

Schaeffer SE. Graph clustering by flow simulation [Internet]. Vol. 1, Computer Science Review. University of Utrecht; 2007. Available from: http://www.sciencedirect.com/science/article/pii/S1574013707000020%5Cnhttp://linkinghub.elsevier.com/retrieve/pii/S1574013707000020

Sharan R, Ulitsky I, Shamir R. Network-based prediction of protein function. Mol Syst Biol. 2007;3:1–13.

Song C, Havlin S, Makse HA. Self-similarity of complex networks. Nature. 2005 Jan;433(7024):392–5.

Song J, Singh M. How and when should interactome-derived clusters be used to predict functional modules and protein function? Bioinformatics. 2009;25(23):3143–50.

Sperry MM, Telesford QK, Klimm F, Bassett DS. Rentian scaling for the measurement of optimal embedding of complex networks into physical space. J Complex Networks [Internet]. 2017 Aug;5(2):199–218. Available from: http://dx.doi.org/10.1093/comnet/cnw010

Spirin V, Mirny LA. Protein complexes and functional modules in molecular networks. Proc Natl Acad Sci U S A. 2003 Oct;100(21):12123–8.

Stearns FW. One hundred years of pleiotropy: A retrospective. Genetics [Internet]. 2010;186(3):767–73. Available from: http://www.genetics.org/content/186/3/767

Stephens GJ, Johnson-Kerner B, Bialek W, Ryu WS. Dimensionality and dynamics in the behavior of C. elegans. PLoS Comput Biol. 2008;4(4).

Stephens GJ, Johnson-Kerner B, Bialek W, Ryu WS. Dimensionality and dynamics in the behavior of C. elegans. PLoS Comput Biol. 2008;4(4).

Stergachis AB, Neph S, Sandstrom R, Haugen E, Reynolds AP, Zhang M, Byron R, Canfield T, Stelhing-Sun S, Lee K, Thurman RE, Vong S, Bates D, Neri F, Diegel M, Giste E, Dunn D, Vierstra J, Hansen RS, Johnson AK, Sabo PJ, Wilken MS, Reh TA, Treuting PM, Kaul R, Groudine M, Bender MA, Borenstein E, Stamatoyannopoulos JA. Conservation of trans-acting circuitry during mammalian regulatory evolution. Nature. 2014 Nov;515(7527):365–70.

Stevens CF. Darwin and Huxley revisited: The origin of allometry. J Biol. 2009;8(2):14.

Stroobandt D. Analytical methods for a priori wire length estimates in computer systems, November 1998. University of Ghent; 1998.

Stroobandt D. Rent's Rule Coincidence or the Result of the Design Process? In: Proc of the IEEE System Level Interconnect Prediction (SLIP) Workshop [Internet]. 2007. Available from: http://www.elis.rug.ac.be/

Varshney LR, Chen BL, Paniagua E, Hall DH, Chklovskii DB. Structural properties of the Caenorhabditis elegans neuronal network. PLoS Comput Biol. 2011 Feb;7(2):e1001066.

Wagner A. The yeast protein interaction network evolves rapidly and contains few redundant duplicate genes. Mol Biol Evol. 2001;18(7):1283–92.

Yang J, Leskovec J. Defining and evaluating network communities based on ground-truth. Knowl Inf Syst. 2015;42(1):181–213.

Yang X, Bozorgzadeh E, Sarrafzadeh M. Wirelength estimation based on Rent exponents of partitioning and placement. 2001 Int Work Syst Interconnect Predict (SLIP 2001). 2001;25–31.

Zinman GE, Zhong S, Bar-Joseph Z. Biological interaction networks are conserved at the module level. BMC Syst Biol. 2011 Aug;5:134.

## 3. Neural network features distinguish chemosensory stimuli in *Caenorhabditis elegans*.

### 3.1 Abstract

Nervous systems extract and process information from their environment to alter animal behavior and physiology. Despite progress in understanding how different stimuli are represented by changes in neuronal activity, less is known about how they affect broader neural network properties. We developed a framework to use graph-theoretic features of neural network activity and predict ecologically-relevant stimulus properties – namely, stimulus identity and valence. Specifically, we used the transparent nematode, *Caenorhabditis elegans*, with its small nervous system, to define neural network features associated with various chemosensory stimuli. We trapped animals using a microfluidic device and exposed their noses to chemical stimuli known to be attractive or repellent, while monitoring changes in neural activity in more than 40 neurons in their heads. We found that repellents trigger higher average neural activity across the network, and that the tastant salt increases neural variability. In contrast, graph-theoretic features, which capture patterns of interactions between neurons, are better suited to decode stimulus identity than measures of neural activity. Furthermore, we show that a simple machine learning classifier trained using graph-theoretic features alone or in combination with neural activity features can accurately predict stimulus identity. These results indicate that graph theory reveals network characteristics that are distinct from neural activity, confirming its utility in extracting stimulus properties from neural population data.

## 3.2 Significance Statement

Changes in the external environment (stimuli) alter patterns of neural activity in animal nervous systems. A central challenge in computational neuroscience is to identify how stimulus properties alter interactions between neurons. We recorded neural activity from *C. elegans* head neurons while the animal experienced various chemosensory stimuli. We then used a combination of activity statistics (i.e., average, standard deviation, frequency-based measures) and graph-theoretic features of network structure (e.g., modularity – the extent to which a network can be divided into independent clusters) to accurately predict stimulus identity. Our method is general and can be used across species, especially in instances when individual neural identities are unknown.

## 3.3 Introduction

Animals have evolved mechanisms to encode the vast array of chemical information in their environment. The underlying neural circuitry encoding odor and taste information in both vertebrates and invertebrates is thought to include both labeled lines and combinatorial activity patterns. Specifically, odor information is initially filtered by olfactory sensory neurons that are organized into specific expression zones in the vertebrate olfactory epithelium (Ressler et al., 1993), and into sensilla selective for pheromones (Kurtovic et al., 2007), food odors (Hallem and Carlson, 2006), acids (Ai et al., 2010), oviposition cues (Dweck et al., 2013) or toxic odors (Stensmyr et al., 2012) in flies. This information is relayed to specific glomeruli and then higher-order centers in the brain (Leinwand and Chalasani, 2011; Grabe and Sachse, 2018). Similarly, taste information in both flies and mice are represented by spatial patterns of neural activity,

likely using combinatorial coding (Smith and St John, 1999; de Brito Sanchez and Giurfa, 2011; Ohla et al., 2019). While these studies highlight the progress made in understanding how chemical information is encoded in the periphery and early cortical areas, its processing and representation in higher brain centers is poorly understood. One solution to this problem is to monitor neural activity of the entire circuit in an intact nervous system as the animal experiences changes in its chemical environment, and to extract neural features that predict those changes.

The nematode *C. elegans*, with its nervous system consisting of just 302 neurons connected by identified chemical and electrical synapses (White et al., 1986; Cook et al., 2019), is ideally suited to record neural activity across a large part of the network. *C. elegans* neurons express rapidly activating voltage-gated calcium channels, such that changes in neuronal calcium approximately correlate with neuronal depolarization (Jospin et al., 2002; Kerr et al., 2000; Liu et al., 2018). By monitoring neural activity using genetically encoded calcium indicators, we previously showed that *C. elegans* sensory neurons encode chemical stimulus concentration and identity using a combinatorial code (Leinwand and Chalasani, 2013; Leinwand et al., 2015). Moreover, large-scale activity measurements in the *C. elegans* nervous system are aided by two innovations – custom-designed microfluidic devices that trap and precisely deliver chemical stimuli to adult animals during recording of neural activity (Chronis et al., 2007; Chalasani et al., 2007), and nuclear-localized genetically encoded calcium indicators that restrict fluorescent signals to easily resolved neuronal nuclei instead of overlapping cytoplasm (Schrodel et al., 2013).

Previous analyses of *C. elegans* whole-brain imaging data used principle components analysis (PCA) to show that neural activity lies in a low-dimensional space (Kato et al., 2015; Nichols et al., 2017; Skora et al., 2018). For example, Kato et al. (2015) showed that the *C. elegans* neural network likely exists in a few global states that might represent locomotory commands, such as forward movement, reversals, turns, and others. Nichols et al. (2017) and Skora et al. (2018) revealed low-dimensional neural activity patterns associated with physiological and behavioral states, such as sleep and starvation. Critically, these approaches required having labels for neurons such that the same neuron can be uniquely identified across animals. However, in most model systems (e.g., recording from cortical neurons in a mouse), such neuron-specific labels do not exist, precluding the use of PCA-based approaches in this manner. Furthermore, Scholz et al. (2018) found evidence that neural dynamics have higher dimensionality than previously thought, suggesting the engagement of many neurons in driving behavior. Hence, even with neuron-specific labels, it is important to probe how the entire network cooperates to process stimuli.

Therefore, here we ask: can we identify stimulus properties using graph-theoretic features of neural interactions recorded during stimulus onset or offset? Graphs are a natural representation to capture the pairwise interactions between nodes (or neurons) connected by edges (functional interactions). Graphs have been used to uncover structure-function relationships in physical, biological, social, and information systems (Müller et al., 2012; Easley and Kleinberg, 2010; Barabási, 2016). By viewing a nervous system as a graph, we hypothesize that we may uncover more complex patterns of activity than if we considered neurons as independent units. Indeed, we identified a range

of network features that emerge in response to chemosensory stimulation. We chose five chemical stimuli each at two different concentrations and monitored the responses of at least 40 head neurons. Head neurons in *C. elegans* include olfactory and gustatory sensory neurons, several downstream interneurons and command interneurons that direct locomotion, and some motor neurons (White et al., 1986). We then computed how two stimulus properties – a chemical's valence (attractant or repellent) and identity (i.e., chemical structure) – affect neural activity across the network. We observed that activity statistics and graph-theoretic features were successful in discriminating between stimulus properties, and validated these results using machine learning classifiers. Finally, we found that chemical identity mostly altered the subnetwork composed of putatively excitatory, as opposed to inhibitory, interactions, suggesting that patterns of excitation define the representation of a chemical in the nematode brain.

### 3.4 Results

We performed whole-brain calcium imaging in 30 worms immobilized in an olfactory chip, a microfluidic device that permits near-instantaneous switching between two fluid flows (Figure 1A; Chronis et al., 2007). Each worm experienced three 21-minute imaging sessions: one without stimulation ("Spontaneous", although M9 buffer is still present), one with buffer changes around the animal's nose ("Buffer", with M9 buffer), and one with chemical stimulation ("Stimulus", where an odorant or tastant was diluted in M9 buffer). Sessions with stimulation had seven pulses that lasted 30 seconds, 1 minute, or 3 minutes (Figure 1B; modified from Albrecht and Bargmann, 2011). We exposed worms to one of 10 conditions: high or low concentrations of one of five chemical stimuli (Figure

1C). Stimuli were either innately attractive or repellent as determined by previous chemotaxis and drop assays (Figure 1C; Bargmann et al., 1993; Chatzigeorgiou et al., 2013). We monitored and tracked the activity of each neuron individually within a session, but we did not identify that same neuron across animals or sessions (i.e., Spontaneous, Buffer, Stimulus). Some neural responses were locked to the onset or offset of the stimulus in the Buffer and Stimulus sessions, and were likely sensory or interneurons involved in the detection and behavioral response to chemical stimulation (Chalasani et al., 2007). Other neurons may be interneurons or motor neurons involved in motor commands (Kato et al., 2015). A median of 44, 48, and 64 neurons were active during Spontaneous, Buffer, and Stimulus sessions, respectively, which indicated that more neurons were active during Stimulus sessions than either Spontaneous or Buffer sessions (Figure 1D). All Stimulus sessions, however, activated similar numbers of neurons, regardless of stimulus identity (Figure 2). Thus, network engagement increases in response to stimuli, and we next sought to assess whether different stimulus properties can be extracted using signatures of this change.

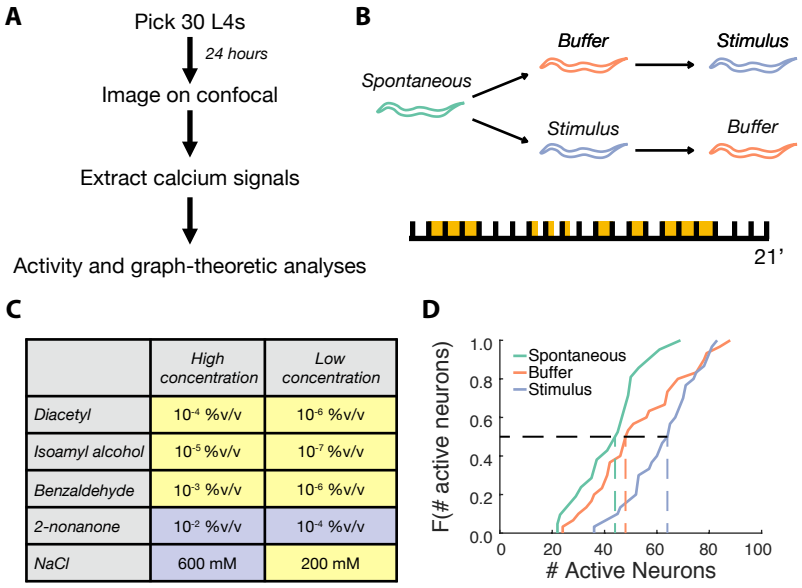


| | *High concentration* | *Low concentration* |
|---|---|---|
| *Diacetyl* | $10^{-4}$ %v/v | $10^{-6}$ %v/v |
| *Isoamyl alcohol* | $10^{-5}$ %v/v | $10^{-7}$ %v/v |
| *Benzaldehyde* | $10^{-3}$ %v/v | $10^{-6}$ %v/v |
| *2-nonanone* | $10^{-2}$ %v/v | $10^{-4}$ %v/v |
| *NaCl* | 600 mM | 200 mM |

Figure 3.1 Whole-brain imaging experiments and analysis. A) Schematic showing the experimental proto- col. Thirty stage L4 animals were picked onto a plate covered with OP50 24 hours before each experiment. Animals, as 1-day old young adults, were stimulated in an olfactory chip and their neural responses were imaged on a Zeiss Airyscan 880. Fluorescence traces were extracted from each video, and subsequently analyzed. B) Animals were imaged in three 21 minute-long sessions: Spontaneous, Buffer, and Stimulus. Buffer and Stimulus sessions used seven pulses of M9 buffer or one of 10 chemicals, respectively. C) Table showing the chemicals (attractants are colored yellow, repellents are violet) and concentrations tested. Three animals were tested per stimulus condition. %v/v refers to % vol/vol. D) The cumulative distribution function for the number of neurons active during Spontaneous (green), Buffer (orange), and Stimulus (blue) sessions shows that more neurons are active when a stimulus is present (p = 9.20E-6 and p = 4.61E-3 for the Spontaneous to Stimulus and Buffer to Stimulus comparisons, respectively, by the two-sample Kolmogorov-Smirnov test). N = 21, 30, and 30 animals for Spontaneous, Buffer, and Stimulus sessions, respectively.

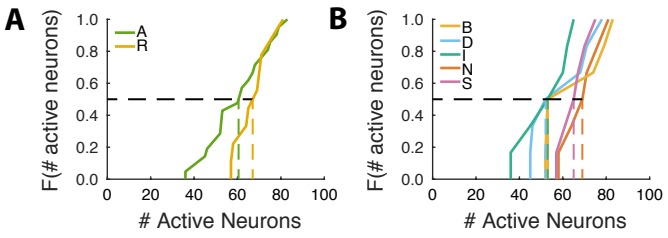


Figure 3.2 Chemical classes do not activate different numbers of neurons. The cumulative distribution of number of active neurons does not differ in a (A) valence- or (B) identity-dependent manner. All $p > 0.05$, by two-sample Kolmogorov-Smirnov test. N = 21 for attractants and N = 9 for repellents (A), and N = 6 for each chemical stimulus (B).

### 3.4.1 Stimulus valence and identity alter neural activity statistics

We first tested if simple measures of neural activity systematically changed with respect to different stimulus properties. We considered two ecologically-relevant stimulus properties: 1) Identity (diacetyl, 2-nonanone, benzaldehyde, isoamyl alcohol, or NaCl) and 2) Valence (attractive or repellent). We reasoned that an animal navigating its environment will recognize different chemicals (i.e., identity) as nutritious or toxic (i.e., valence). We focused on statistical measures (average and standard deviation of normalized neural activity) and measures that capture temporal dynamics (Fourier-based analysis of frequency spectra; Chalasani et al., 2010). Each cell's activity was normalized to the peak value it attained in the 21-minute session, and all measures were normalized to their pre-switch values.

We found that stimulus valence and identity have distinct effects on neural activity at stimulus onset (Figures 3A,C, 4) but not offset (Figures 3B,D, 5). For example, repellents (2-nonanone and 600mM NaCl) evoked higher mean neural activity than attractants (diacetyl, benzaldehyde, isoamyl alcohol, and 200mM NaCl) on stimulus onset

(Figures 3A, 4A), but not offset (Figures 3B, 5A). The tastant NaCl induced more variable neural activity than the odorants on stimulus onset but not on offset (Figures 3C,D, 4, 5), and there was no effect of stimulus identity on the mean activity (Figures 3C,D, 4, 5). While repellents decreased the average frequency with the most power on stimulus onset (Figures 3A, 4A), there was no difference between repellents and attractants on offset (Figures 3B, 5A). For stimulus identity, the offset (Figures 3D, 5B) of diacetyl and isoamyl alcohol slightly increased the peak frequency of neural oscillations (i.e., max of the frequencies with the most power in a sliding window over a 30-second period), but this effect was not observed on stimulus onset (Figures 3C, 4B). Finally, there was no significant difference for most properties in buffer trials (Figures 3, 4, 5), which indicates that these measures are sensitive to chemosensory stimulation. Thus, activity features are modulated by stimulus properties in an inconsistent manner at stimulus onset and offset.


Figure 3.3 Stimulus valence and identity have distinct effects on neural activity. Repellents induce an increase in average neural activity and a decrease in the average frequency of the peak frequency on stimulus onset (A), with no changes on stimulus offset (B). On the other hand, stimulus identity affects the variability (i.e., standard deviation) of neural activity on stimulus onset (C), and the peak frequency on stimulus offset (D). There were no changes in any of the measured properties on buffer onset (A, C) or offset (B, D). Avg and S.D. of activity refer to average and standard deviation of neural activity. Power in 3rd band refers to average power in the frequency range from 0.34 - 0.47 Hz. Peak frequency is the frequency with the most power in a 30-second bin, and avg frequency is the average of the frequencies with the most power in a sliding-window bin covering a 30-second period. N = 21 for attractants and N = 9 for repellents (A, B). N = 6 for each chemical stimulus (C, D). * $p < 0.025$, *** $p < 0.0005$, by likelihood ratio test on full and null generalized linear mixed-effects model, where the former included either valence or identity as a fixed effect.

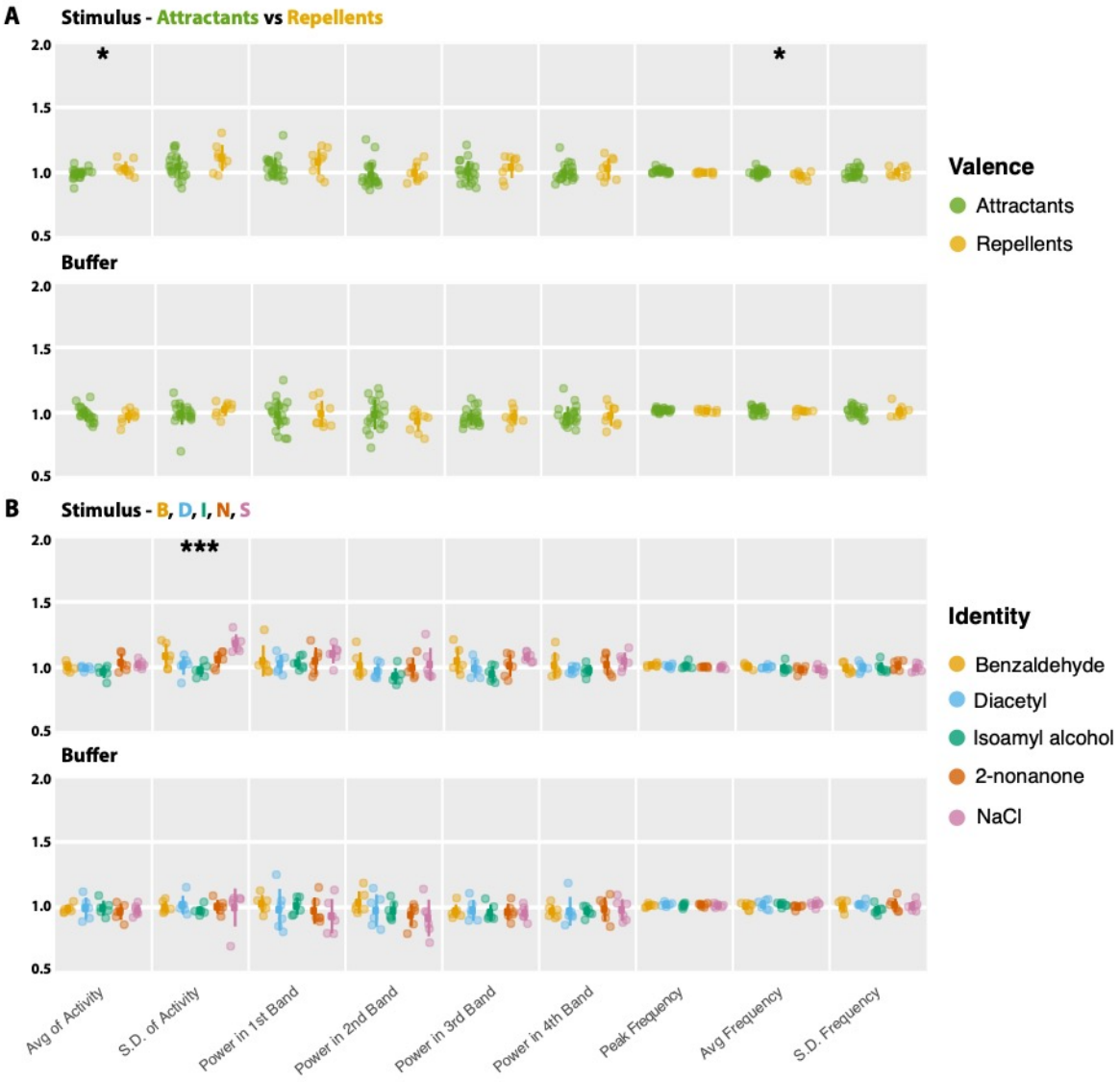


Figure 3.4 Stimulus valence and identity have distinct effects on neural activity on stimulus onset. Repellents induce an increase in average neural activity and a decrease in the average frequency of the peak frequency on stimulus onset (A). On the other hand, stimulus identity affects the variability (i.e., standard deviation) of neural activity on stimulus onset (B). There were no changes in any of the measured properties on buffer onset (A, B). Avg and S.D. of activity refer to average and standard deviation of neural activity. Power in 1st, 2nd, 3rd, and 4th bands refer to average power in the frequency ranges from 0.07 - 0.2 Hz, 0.2 - 0.34 Hz, 0.34 - 0.47 Hz, and 0.47 - 0.6 Hz. Peak frequency is the frequency with the most power in a 30-second bin, and avg frequency and S.D. frequency are the average and standard deviation, respectively, of the frequencies with the most power in a sliding-window bin covering a 30-second period. N = 21 for attractants and N = 9 for repellents (A), and N = 6 for each chemical stimulus (B). * $p < 0.025$, *** $p < 0.0005$, by likelihood ratio test on full and null generalized linear mixed-effects model, where the former included either valence or identity as a fixed effect.

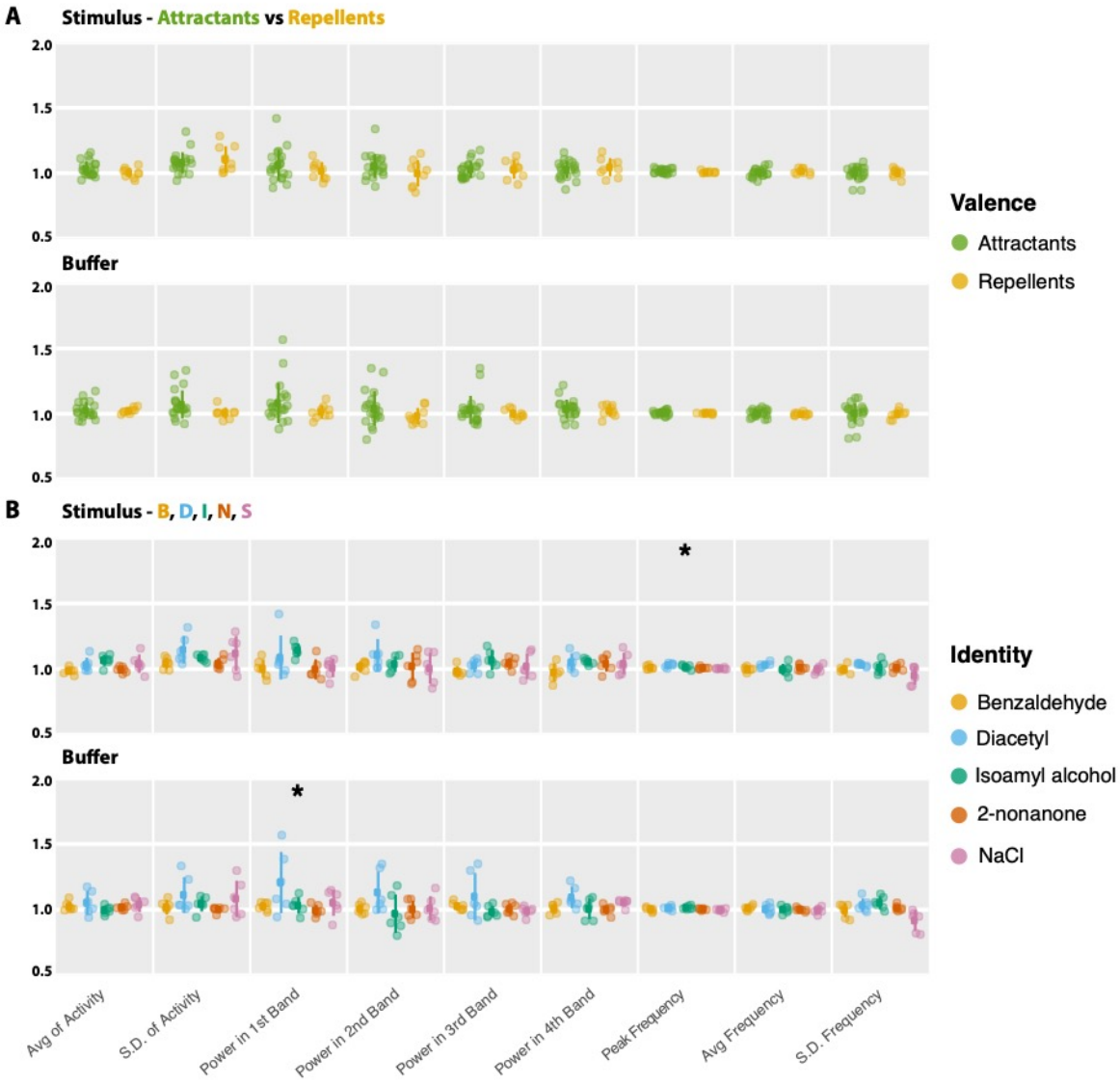


Figure 3.5 Stimulus valence and identity have distinct effects on neural activity on stimulus offset. Repellents effect no change in neural activity on stimulus offset (A). On the other hand, stimulus identity affects the peak frequency of neural activity on stimulus offset (B). Buffer offset affected average power in the 1st frequency band (B). Avg and S.D. of activity refer to average and standard deviation of neural activity. Power in 1st, 2nd, 3rd, and 4th bands refer to average power in the frequency ranges from 0.07 - 0.2 Hz, 0.2 - 0.34 Hz, 0.34 - 0.47 Hz, and 0.47 - 0.6 Hz. Peak frequency is the frequency with the most power in a 30-second bin, and avg frequency and S.D. frequency are the average and standard deviation, respectively, of the frequencies with the most power in a sliding-window bin covering a 30-second period. N = 21 for attractants and N = 9 for repellents (A), and N = 6 for each chemical stimulus (B). * $p < 0.025$, *** $p < 0.0005$, by likelihood ratio test on full and null generalized linear mixed-effects model, where the former included either valence or identity as a fixed effect.

Previous studies have shown that spontaneous activity in the nervous system of an immobilized worm lies in a low-dimensional PCA space (Kato et al., 2015; Nichols et al., 2017; Skora et al., 2018). Indeed, our analyses also suggest that, during the Spontaneous session, neural activity loops through a low-dimensional manifold, where the first three principal components (PCs) capture a median of 59% of the variance in our 21-minute long imaging sessions (Figure 6A,C). However, we found that PCA was not able to infer different states during any type of stimulation – either Buffer or Stimulus changes – as both exhibited more complicated network dynamics than observed in an unstimulated worm (Figure 6B). Specifically, the first three PCs captured a median of only 51% of the variance in stimulation sessions (Figure 6C; p = 0.002 and 4.54E-5 for Spontaneous to Buffer and Spontaneous to Stimulus comparisons, respectively), and instead of smooth trajectories through PCA space, we observed jumps between different regions of state space (Figure 6B). This agrees with (Scholz et al., 2018), who found that a non-stimulated, but moving, worm also exhibits network dynamics that cannot be easily explained by the first three PCs.

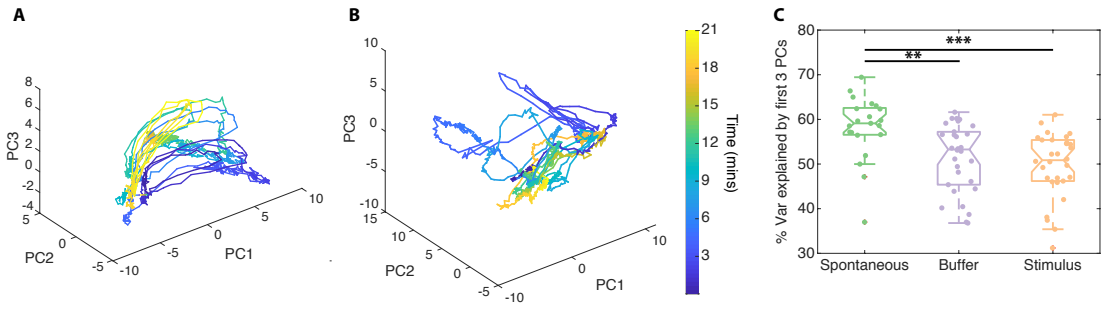


Figure 3.6 Observed neural dynamics preclude the use of PCA. Example neural dynamics observed during a Spontaneous session form loops through PCA-space (A), but not during a Stimulus session (B). Generally, the first three principal components explain a larger percentage of the variance during Spontaneous sessions than during Buffer or Stimulus sessions (C). Kruskall-Wallis test, with Dunn-Sidak post-hoc test, ** $p < 0.01$, *** $p < 0.001$.

Thus, a different approach is needed to decode stimulus properties from network dynamics in the absence of neural labels, particularly if traditional dimensionality-reduction-based methods fail to capture a significant portion of the variance. We next propose to use graph-theoretic features of the interactions between neurons.

### 3.4.2 Computing graph-theoretic features of neural activity

We next asked if different stimulus properties could be better distinguished based on interaction patterns between neurons, instead of activity statistics of individual neurons. Graph-theoretic features capture complex interactions amongst groups of neurons. For example, these features can quantify how well a network can be divided into relatively independent clusters such that neurons in a cluster mostly interact with other neurons in the same cluster and sparsely interact with neurons in other clusters (this feature is called modularity). Other features capture how quickly information can spread through the network such that signals in one part of the network can be received and processed in another part of the network (one such feature is the largest eigenvalue of the graph) (Rubinov and Sporns, 2010; Yang et al., 2003). Graph-theoretic features have been previously used to characterize activity changes in coarse brain networks (e.g., where nodes represent entire brain regions or large populations of neurons; reviewed by Rubinov and Sporns, 2010; Bassett and Sporns, 2017), but have not, to our knowledge, been used to analyze whole-brain activity at the single neuron level.

To characterize interactions between neurons, we first need to infer interactions between neurons based on their individual activities. For example, if neuron B's activity rises shortly after neuron A's activity rises, then we may infer a functional interaction

between neurons A and B. Formally, to predict interactions, we computed the normalized mutual information (NMI; Strehl and Ghosh, 2002) between the activity vectors of every pair of neurons in a 30-second period around a stimulus switch (i.e., onset or offset). NMI measures how much information one variable contains about another variable, which in this context reveals a putative interaction between the activity vectors of two neurons (see Materials and Methods). We computed the NMI between all pairs of *n* neurons in a given worm during a 30-second period of interest (either before or after a stimulus switch). We focused on a 30-second period for two reasons: 1) an animal can begin to move toward or away from an attractant or repellent, respectively, well within 30 seconds (Albrecht and Bargmann, 2011; Hilliard et al., 2002), and 2) sensory neurons that detect chemical stimuli tend to reach their maximum response within ~10 seconds of stimulus onset (Chalasani et al., 2007). Thus, analyzing 30 seconds following a stimulus switch should be sufficient to capture the representation of ecologically-relevant information in neural activity (Chalasani et al., 2007; Chatzigeorgiou et al., 2013; Hilliard et al., 2002).

We then computed a weighted graph $G=(V,E)$, where $V$ is the set of nodes (neurons) and $E$ is the set of weighted edges (inferred functional interactions) between neurons. Each edge weight equals the NMI between the two neurons, which lies between 0 and 1, where a larger number implies a stronger interaction. Pearson's correlation (PC) has been previously used (Bassett et al., 2011) to generate functional connectivity networks with both positive and negative weights (as well as 0 for uncorrelated neurons, which is rare in practice); the former indicates that both neurons increase or decrease their activity together (e.g., excitation), and the latter implies that as one neuron increases its activity, the other neuron's activity decreases (e.g., inhibition). As a group, GCaMPs

are known to faithfully reflect increases in a cell's internal calcium concentration, and thus its excitation; however, GCaMPs were not optimized to reflect a decrease in calcium concentration, or its hyperpolarization (e.g., see Tian et al., 2009; Akerboom et al., 2012). Further, many graph-theoretic analyses require that all edge weights be non-negative, and we found that 46.8% of edges had a negative weight when we used Pearson's correlation. Thus, we did not use weights from Pearson's correlation, though we did use it in separate analyses to independently study the putatively excitatory and inhibitory subnetworks.

From each graph, we extracted network features that capture different interaction patterns at both the local and global network scales. Specifically, we focused on five classes of network measures, including basic structure, functional segregation, functional integration, centrality, and resilience (summarized in Table 1 and Rubinov and Sporns, 2010). Basic structure refers to general aspects of the graph, such as the largest eigenvalue or the median weight of the network, which indicates how strongly nodes interact with one another. Functional segregation measures how much processing occurs in small groups of neurons, or modules, and encompasses the network's modularity and number of modules – in a more modular network, neurons cluster into groups that strongly communicate with one another. Functional integration indicates how efficiently different groups of neurons can pass information to each other; a representative measure is the average shortest path distance between pairs of neurons in the network, which indicates how quickly, on average, information can pass between any two neurons. Centrality measures how important, or central, a neuron is to information transmission between different parts of the network and can be assessed, for example, using the average

betweenness centrality – the average fraction of shortest paths linking any two neurons that pass through a given neuron. Finally, measures of resilience to perturbations, such as lesions, includes the average assortativity coefficient – the average correlation coefficient between the degrees of any two connected neurons.

For fair comparisons, each graph-theoretic feature was normalized to account for any dependence on network size (van Wijk et al., 2010). Further, to highlight changes in a graph-theoretic property after a stimulus switch, we used the same normalization scheme we used for neural activity features – in short, we divided the post-switch value of the feature to its pre-switch value. This was a critical normalization scheme as the organization of each worm's neural network was quite variable, even in the absence of stimulation (Figure 7). Thus, we report how the addition or removal of a stimulus affected patterns of neural network activity.

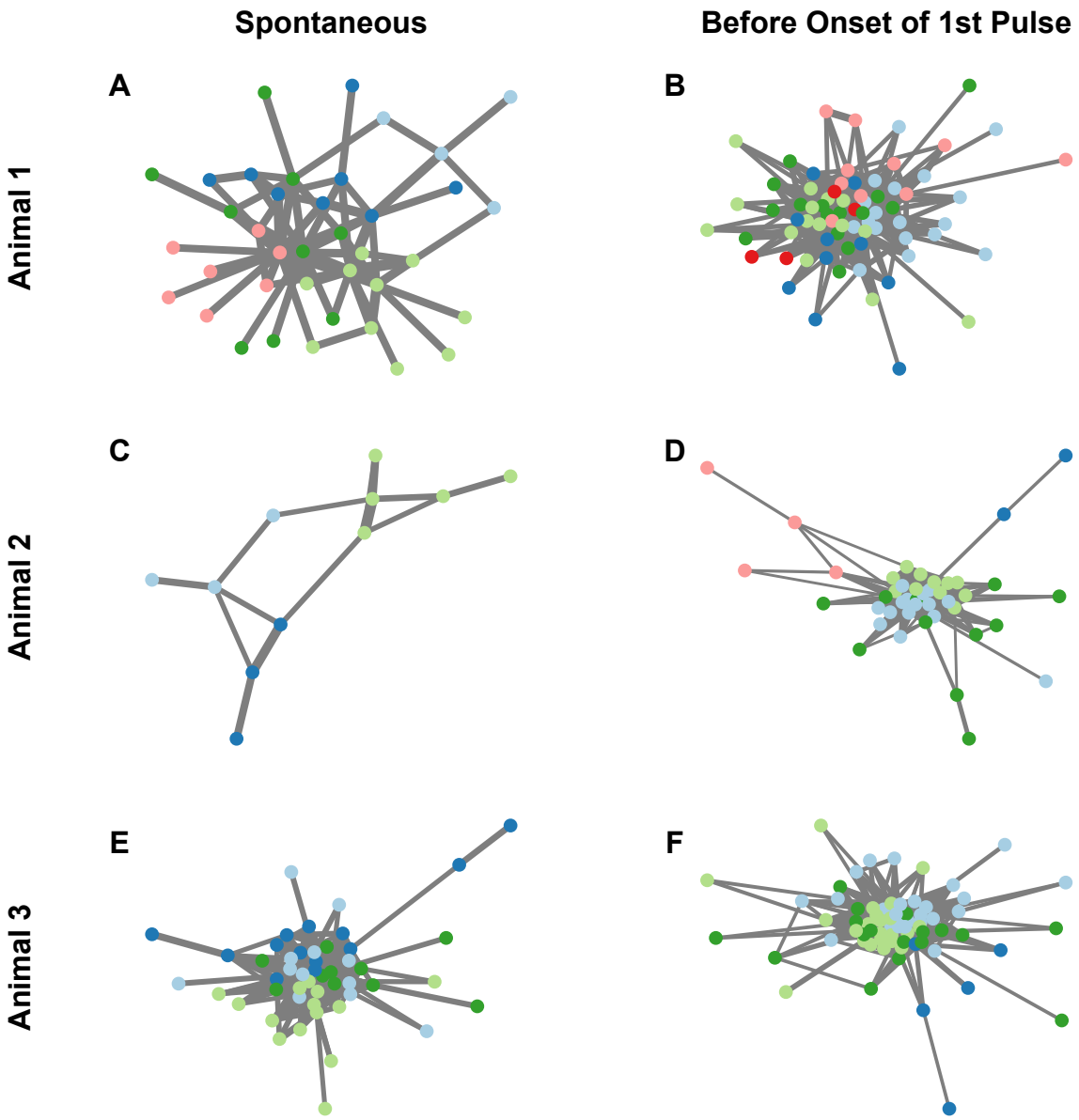


Figure 3.7 The neural networks of worms vary both within and across worms. The networks depicted here, for three example worms, show neurons (circles) connected by lines (edges); the thickness of the edges correspond to the amount of normalized mutual information between the two linked neurons. All networks are based on neural activity observed in the 30-second period between 30 seconds and 1 minute into the beginning of either the Spontaneous (A, C, E) or Stimulus (B, D, F) session for three worms. Neurons with the same color belong to the same module. Some worms have different numbers of modules in the absence of stimulus (A has 5 modules, B has 6 modules), while others have different numbers of strongly interacting neurons (C, D), and still others look fairly similar (E, F). All edges less than 0.2 were removed for the purpose of visualization.

Table 3.1 Definition of graph-theoretic features studied in this manuscript. The twenty-two listed features are grouped into one of five classes: basic structure (of the adjacency matrix), functional segregation (measures of the decomposability of the network), functional integration (the potential for disparate parts of the network to communicate), centrality (the importance of any one neuron to network communication), and resilience to perturbations, such as lesions (measures of how robust the system is to disruptions at individual nodes).

| **Graph Theory Feature** | **Description** |
|---|---|
| *Basic structure* | |
| numNodes | the number of neurons that had at least one non-zero weight to another neuron |
| numEdges | the number of edges |
| density | the density of edges (i.e., the number of actual edges divided by the total possible number of edges in a fully-connected network) |
| numComponents | the number of isolated subgraphs in the network |
| avgWeight | the average weight of the network |
| medWeight | the median weight of the network |
| avgEigenvalue | the mean of the positive eigenvalues of the adjacency matrix |
| maxEigenvalue | the largest eigenvalue of the adjacency matrix |
| *Functional segregation* | |
| avgClusteringCoeff | the average over all neurons of the fraction of 3-neuron clusters, or triangles, around each neuron |
| transitivity | a globally normalized version of the clustering coefficient |
| avgLocalEff | the mean local efficiency (i.e., the average over all neurons of the lengths of the shortest paths between two of the neuron's neighbors) |
| modularity | the extent to which a network can be divided into clusters, or modules, of neurons with dense connections amongst themselves, and sparse connections to neurons in other clusters |
| numModules | the number of modules |
| *Functional integration* | |
| avgShortestPath | the average shortest path between all pairs of neurons in the network |
| globalEff | the global efficiency, or the average inverse shortest path length |
| radius | the smallest shortest path connecting any two neurons |
| diameter | the largest shortest path connecting any two neurons |
| *Centrality* | |
| avgParticipationCoeff | the degree to which a neuron communicates with neurons in different modules |
| avgBetweennessCentrality | the average of the fraction of shortest paths linking any two neurons that pass through a given neuron |

Table 3.1 Definition of graph-theoretic features studied in this manuscript (continued).

| Graph Theory Feature | Description |
|---|---|
| *Resilience to perturbations* | |
| avgDegDist | the average of each neuron's degree, or sum of the edge weights to other neurons |
| assortCoeff | the correlation coefficient between the degrees of two connected neurons, where a negative number indicates neurons with a high degree are connected to neurons with a low degree |
| avgNeighborDegree | the average degree of the neighbors of a given node, averaged over all nodes |

### 3.4.3 Graph-theoretic features distinguish stimulus identity

For each stimulus property, we tested the extent to which any graph-theoretic feature significantly changed in response to a stimulus switch. Overall, some network features showed a reliable change upon both switches (onset and offset), whereas activity features of neurons revealed no such reliable change. For example, the average betweenness centrality reliably changed with respect to stimulus valence. Repellents decreased the network's average betweenness centrality on both stimulus onset and offset, while attractants had no effect (Figures 8A,B; Table 2). Furthermore, these changes were not concomitant with a change in the median weight of the network (Figure 8A,B; Table 2), which indicates that the change in average betweenness centrality is not simply driven by stronger or weaker interactions in one condition over another, but rather by differences in the patterns of interactions amongst neurons. Thus, valence modulates the centrality of neurons bridging disparate regions of the network. Surprisingly, these effects occur both at stimulus onset and offset, indicative of a fundamental signature in how each class of stimulus is processed in the *C. elegans* nervous system.

Stimulus identity affected several features, though there were only a few features - the median network weight, transitivity, and max eigenvalue - that reliably changed on both stimulus onset and offset (Figures 8C,D, 9, 10; Table 2). When worms were exposed to NaCl, the network had the largest median weight and the smallest diameter (i.e., the furthest distance between any two neurons). This indicates that the NaCl-induced network could efficiently transmit information across the network. Furthermore, this network had the largest transitivity (i.e., average strength of interactions between connected triplets of neurons) and max eigenvalue (the larger the max eigenvalue, the more easily signal spreads through a network), suggesting a unique combination of strong local connectivity and efficient global reach, which is often observed in small-world networks (Watts and Strogatz, 1998). Buffer sessions modulated no graph-theoretic features on buffer onset (Figures 8, 9, 10; Table 2); however, for stimulus identity, buffer offset did effect change in several graph-theoretic features, but not median weight (Figure 10; Table 2). This indicates that changes in median weight may require a stimulus, consistent with previous studies showing that stimuli drive correlated activity across multiple neurons (Kohn and Smith, 2005; Eggermont, 2007; Aertsen et al., 1989). Overall, stimulus properties affect network connectivity in a reliable manner, and these features may serve as decoding signatures.


Figure 3.8 Stimulus valence and identity have distinct effects on network features. Repellents consistently induce a decrease in average betweenness centrality on stimulus onset (A) and offset (B). Stimulus identity also affects the average betweenness centrality on stimulus onset (C), but not offset (D), in addition to effects on various other network features. There were no changes in any of the measured properties on buffer onset (A, C) or offset (B, D). N = 21 for attractants and N = 9 for repellents (A, B), and N = 6 for each chemical stimulus (C, D). * $p < 0.025$, ** $p < 0.005$, by likelihood ratio test on full and null generalized linear mixed-effects model, where the former included either valence or identity as a fixed effect.

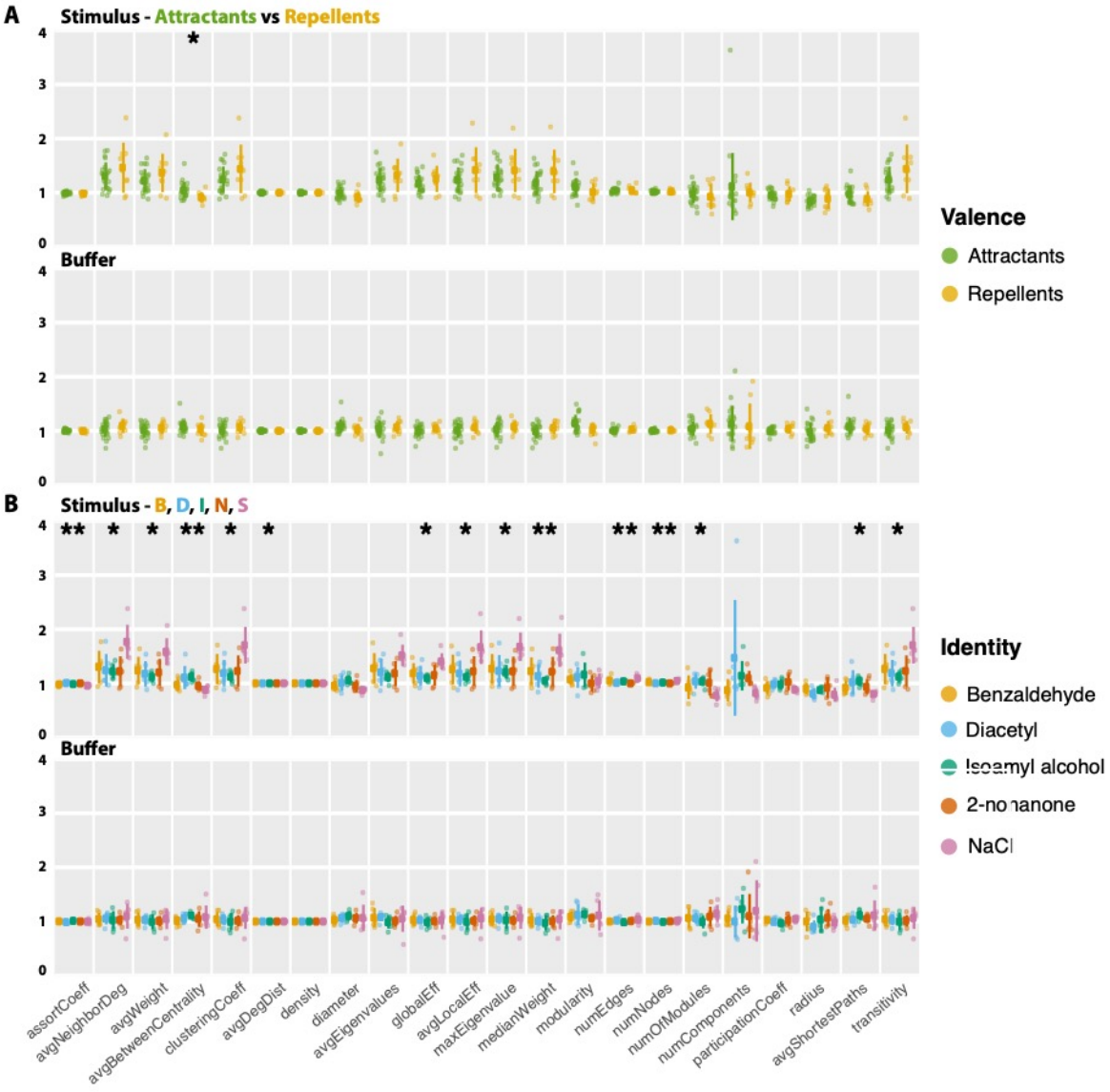


Figure 3.9 Stimulus valence and identity modulate distinct network features on stimulus onset. All 22 graph-theoretic features on the x-axes are plotted according to stimulus valence (A) and identity (B), and depict results from networks computed on stimulus onset during Buffer and Stimulus sessions. Network features are derived from adjacency matrices constructed with normalized mutual information. Colored dots indicate the mean across 7 pulses. N = 21 for attractants and N = 9 for repellents (A), and N = 6 for each chemical stimulus (B). * $p < 0.025$, ** $p < 0.005$, by likelihood ratio test on full and null generalized linear mixed-effects model, where the former included either valence or identity as a fixed effect.

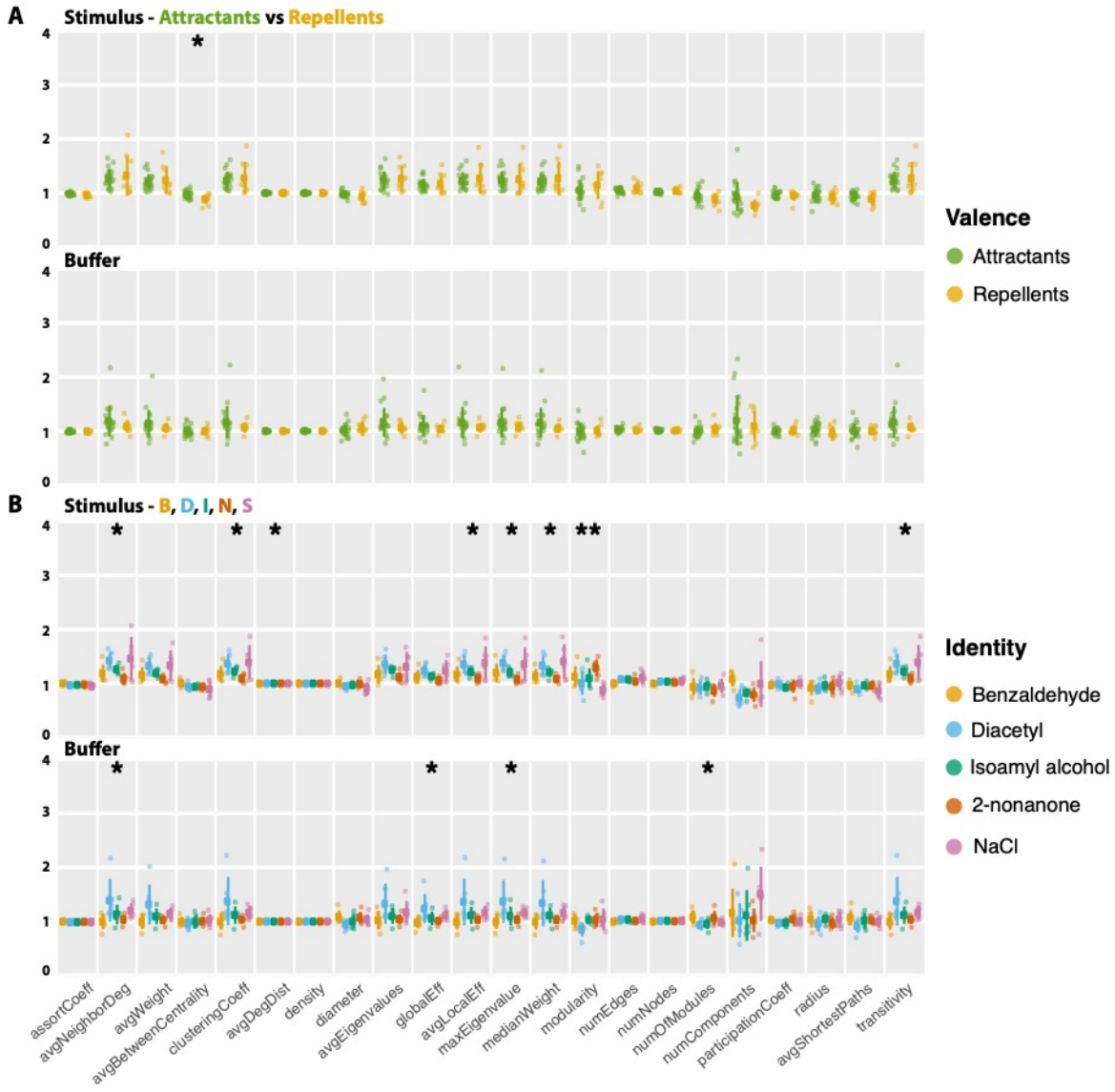


Figure 3.10 Stimulus valence and identity modulate distinct network features on stimulus offset. All 22 graph-theoretic features on the x-axes are plotted according to stimulus valence (A) and identity (B), and depict results from networks computed on stimulus offset during Buffer and Stimulus sessions. Network features are derived from adjacency matrices constructed with normalized mutual information. Colored dots indicate the mean across 7 pulses. N = 21 for attractants and N = 9 for repellents (A), and N = 6 for each chemical stimulus (B). * $p < 0.025$, ** $p < 0.005$, by likelihood ratio test on full and null generalized linear mixed-effects model, where the former included either valence or identity as a fixed effect.

Table 3.2 Graph-theoretic results from likelikood ratio test on generalized linear mixed-effects models. Results from the likelihood ratio test applied on a full vs null model. The full model includes information on either Valence or Identity in addition to the null model. The null model includes information on animal ID and time since first pulse. The p-values in **bold** indicate a significant difference in the data's likelihood when explained with the full model vs the null model; hence, the parameter (i.e., Valence or Identity) significantly improved model fit.

| Session | Pulse Switch | Graph Theory Feature | Valence | Identity |
|---|---|---|---|---|
| Buffer | Onset | assortCoeff | 0.349 | 0.550 |
| | | avgBetweenCentrality | 0.288 | 0.665 |
| | | avgClusteringCoeff | 0.335 | 0.939 |
| | | avgDegDist | 0.448 | 0.688 |
| | | avgEigenvalue | 0.520 | 0.768 |
| | | avgLocalEff | 0.318 | 0.939 |
| | | avgNeighborDeg | 0.297 | 0.915 |
| | | avgParticipationCoeff | 0.235 | 0.362 |
| | | avgShortestPath | 0.329 | 0.607 |
| | | avgWeight | 0.341 | 0.952 |
| | | density | 0.530 | 0.649 |
| | | diameter | 0.166 | 0.872 |
| | | globalEff | 0.311 | 0.955 |
| | | maxEigenvalue | 0.405 | 0.970 |
| | | medWeight | 0.219 | 0.912 |
| | | modularity | 0.034 | 0.918 |
| | | numComponents | 0.626 | 0.756 |
| | | numEdges | 0.297 | 0.270 |
| | | numModules | 0.152 | 0.457 |
| | | numNodes | 0.303 | 0.367 |
| | | radius | 0.246 | 0.432 |
| | | transitivity | 0.335 | 0.939 |
| | Offset | assortCoeff | 0.930 | 0.904 |
| | | avgBetweenCentrality | 0.940 | 0.866 |
| | | avgClusteringCoeff | 0.307 | 0.032 |
| | | avgDegDist | 0.979 | 0.840 |
| | | avgEigenvalue | 0.261 | 0.098 |
| | | avgLocalEff | 0.306 | 0.032 |
| | | avgNeighborDeg | 0.322 | **0.011** |
| | | avgParticipationCoeff | 0.508 | 0.241 |
| | | avgShortestPath | 0.982 | 0.165 |
| | | avgWeight | 0.334 | 0.031 |

Table 3.2 Graph-theoretic results from likelikood ratio test on generalized linear mixed-effects models (continued).

| Session | Pulse Switch | Graph Theory Feature | Valence | Identity |
|---|---|---|---|---|
| Buffer | Offset | density | | 0.138 |
| | | diameter | 0.239 | 0.146 |
| | | globalEff | 0.386 | **0.022** |
| | | maxEigenvalue | 0.370 | **0.015** |
| | | medWeight | 0.250 | 0.049 |
| | | modularity | 0.706 | 0.048 |
| | | numComponents | 0.606 | 0.222 |
| | | numEdges | 0.695 | 0.484 |
| | | numModules | 0.311 | 0.084 |
| | | numNodes | 0.819 | 0.658 |
| | | radius | 0.398 | 0.676 |
| | | transitivity | 0.307 | 0.032 |
| Stimulus | Onset | assortCoeff | 0.486 | **0.002** |
| | | avgBetweenCentrality | **0.013** | **0.003** |
| | | avgClusteringCoeff | 0.154 | **0.005** |
| | | avgDegDist | 0.808 | **0.008** |
| | | avgEigenvalue | 0.388 | 0.028 |
| | | avgLocalEff | 0.158 | **0.006** |
| | | avgNeighborDeg | 0.285 | **0.008** |
| | | avgParticipationCoeff | 0.583 | 0.095 |
| | | avgShortestPath | 0.153 | **0.016** |
| | | avgWeight | 0.195 | **0.009** |
| | | density | 0.865 | 0.089 |
| | | diameter | 0.076 | 0.028 |
| | | globalEff | 0.259 | **0.020** |
| | | maxEigenvalue | 0.322 | **0.016** |
| | | medWeight | 0.079 | **0.003** |
| | | modularity | 0.141 | 0.495 |
| | | numComponents | 0.766 | 0.032 |
| | | numEdges | 0.778 | **0.003** |
| | | numModules | 0.481 | **0.021** |
| | | numNodes | 0.733 | **0.003** |
| | | radius | 0.405 | 0.242 |
| | | transitivity | 0.154 | **0.005** |
| | Offset | assortCoeff | 0.075 | 0.063 |
| | | avgBetweenCentrality | **0.021** | 0.267 |
| | | avgClusteringCoeff | 0.654 | **0.020** |
| | | avgDegDist | 0.164 | 0.064 |
| | | avgEigenvalue | 0.692 | 0.126 |
| | | avgLocalEff | 0.649 | **0.022** |

Table 3.2 Graph-theoretic results from likelikood ratio test on generalized linear mixed-effects models (continued).

| Session | Pulse Switch | Graph Theory Feature | Valence | Identity |
|---|---|---|---|---|
| Stimulus | Offset | avgNeighborDeg | 0.638 | **0.012** |
| | | avgParticipationCoeff | 0.410 | 0.325 |
| | | avgShortestPath | 0.158 | 0.196 |
| | | avgWeight | 0.696 | 0.029 |
| | | density | 0.469 | 0.232 |
| | | diameter | 0.131 | 0.247 |
| | | globalEff | 0.729 | 0.050 |
| | | maxEigenvalue | 0.938 | **0.017** |
| | | medWeight | 0.471 | **0.011** |
| | | modularity | 0.304 | **0.002** |
| | | numComponents | 0.056 | 0.041 |
| | | numEdges | 0.113 | 0.030 |
| | | numModules | 0.176 | 0.706 |
| | | numNodes | 0.110 | 0.030 |
| | | radius | 0.587 | 0.686 |
| | | transitivity | 0.654 | **0.020** |

Graph-theoretic features quantitatively capture differences in network structures that emerge during stimulus presentation. To illustrate these differences more intuitively, we visualized how the networks changed shape before and after stimulus onset. Figure 11 shows the network of one worm before the onset of 200 mM NaCl (Figure 11A,C), and during the first 30 seconds of the pulse (Figure 11B, D). In the latter, there is an increase in the number of strong edges (i.e., edges of weight larger than 0.2), a decrease in number of modules (from 7 to 5), and a decrease in the betweenness centrality of several neurons. More neurons are connected with the rest of the network (thereby increasing the max eigenvalue), and triplets of neurons are more likely to be strongly connected (i.e., a larger transitivity). Due to the normalization scheme employed, changes in the values of graph-theoretic features may appear to be mild; however, as illustrated, these changes capture

significant differences in connectivity patterns between neurons and may be biologically informative.

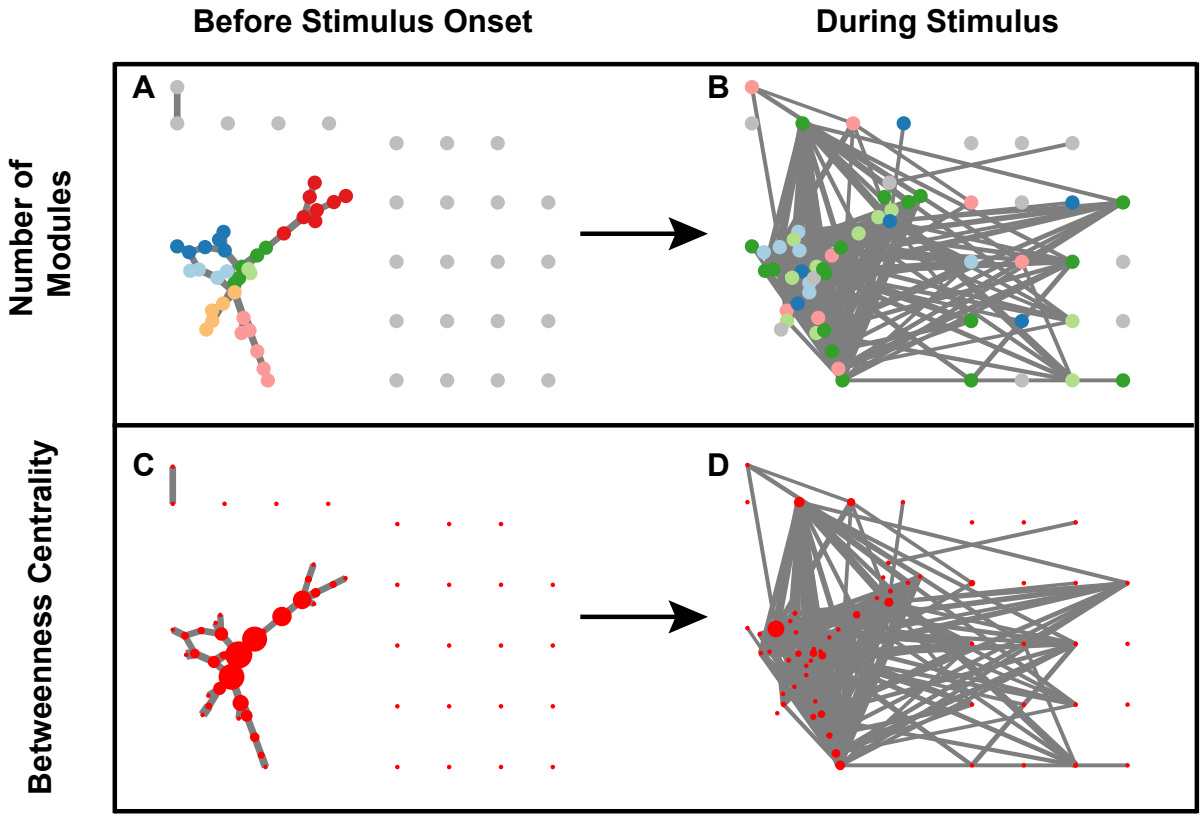


Figure 3.11 NaCl induces a decrease in the number of modules and average betweenness centrality of the worm's neural network. The networks depicted here, for one example worm, show neurons (circles) connected by lines (edges); the thickness of the edges correspond to the amount of normalized mutual information between the two linked neurons. Each neuron's position is fixed across all four panels. Prior to stimulation with 200 mM NaCl (A, C), this worm's functional connectivity had 7 modules (A) and fairly central neurons (C). During the first 30 seconds of stimulation, however, the number of modules dropped to 5 (B has fewer colors than A), with fewer central neurons (D has smaller circles than C). Note the increase in recruited neurons during (B, D), relative to before (A, C), stimulus. Neurons with the same color in A and B belong to the same module. The size of the neurons in C and D are positively correlated with their betweenness centrality. All edges less than 0.2 were removed for the purpose of visualization. Thus, isolated neurons only had weak edges to all other neurons.

### 3.4.4 Using machine learning methods to predict stimulus properties

We used a machine learning approach to test how well neural activity features (Figure 3) and graph-theoretic features (Figure 8) could predict stimulus properties on the first stimulus pulse, when the animal has not undergone any adaptation. As before, the stimulus properties we considered were stimulus valence and identity. We used a logistic regression classifier, which is a simple and commonly used classifier that has no built-in assumptions about the distribution of the data. We evaluated its ability to generalize to unseen networks using cross-validation, followed by a permutation test to assess its performance against an empirically-derived chance level of accuracy (see Materials and Methods). We also combined graph-theoretic and neural activity features, to see if graph theory and neural activity provided distinct information that could collectively improve classification accuracy.

The logistic regression classifier performed well on predicting stimulus identity on onset, but not offset (Figure 12B,D, and Table 3). In particular, accuracy was high when using graph-theoretic features alone (40% accuracy, chance: 20% permutation accuracy: 16±8%, p-value = 0.004). Adding neural activity features increased the accuracy slightly (47% accuracy, Figure 12B). On the other hand, when training the classifier using only neural activity data, accuracy was far lower (17%; Fig 12B). Finally, we did not exceed chance accuracy when classifying attractants and repellents using either of the three feature sets (Figure 12A,C, and Table 3), or any of the buffer sessions except for identity on buffer offset (Figure 13D and Table 3). However, buffer sessions that preceded stimulus sessions did not show above chance accuracy (Figure 14), suggesting that the above-chance performance on all buffer sessions combined might be confounded by prior

stimulus experience. Thus, graph-theoretic features alone appear capable of quantitatively discriminating identity on stimulus onset, with some gain when also including measures of neural activity in combination. Together, these data show that the *C. elegans* neural network responding to stimulus, but not buffer, has structural characteristics that can be identified using graph theory with a simple machine learning classifier.

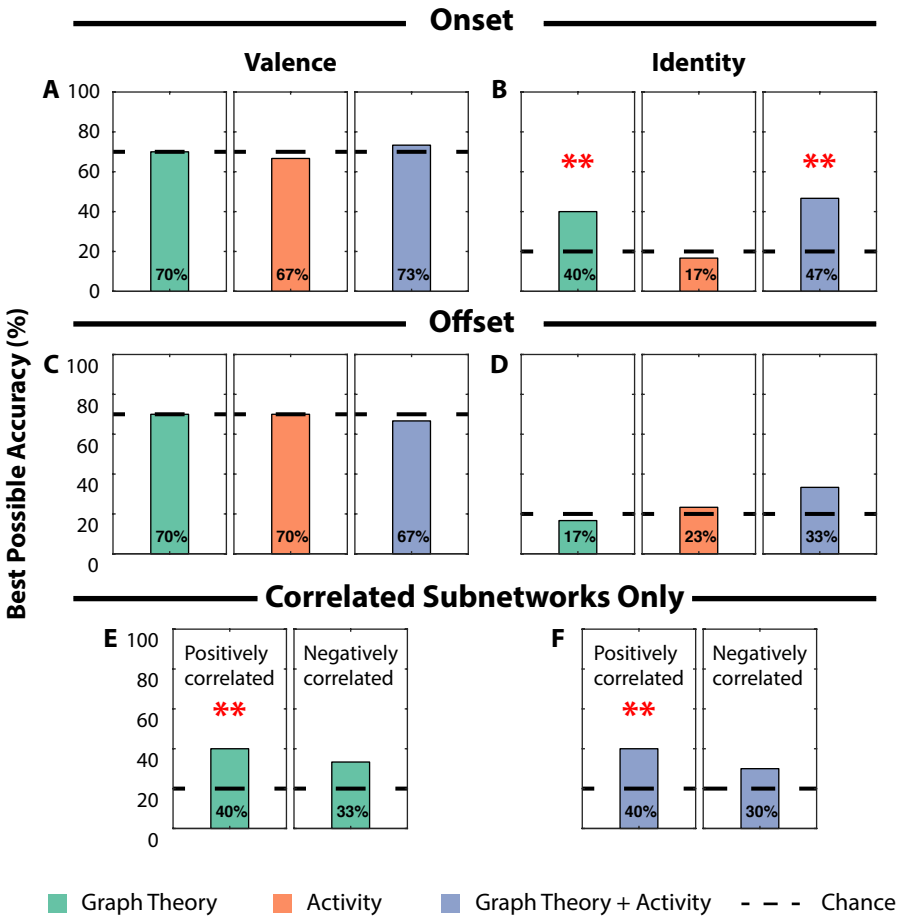


Figure 3.12 Network features increase classification accuracy of stimulus identity. Classification accuracy achieved on the first pulse of Stimulus sessions using a Logistic Regression classifier trained using network features (green), neural activity features (orange) or both (blue). Accuracies are shown for stimulus valence and identity at stimulus onset (A, B) and offset (C, D), respectively. The accuracy on correlated subnetworks for stimulus identity at stimulus onset is shown for only network (E) or combined features (F). Red asterisks indicate significantly above-chance classification accuracy as determined with a permutation test (**$p < 0.005$). Black dotted lines indicate theoretical chance accuracy.

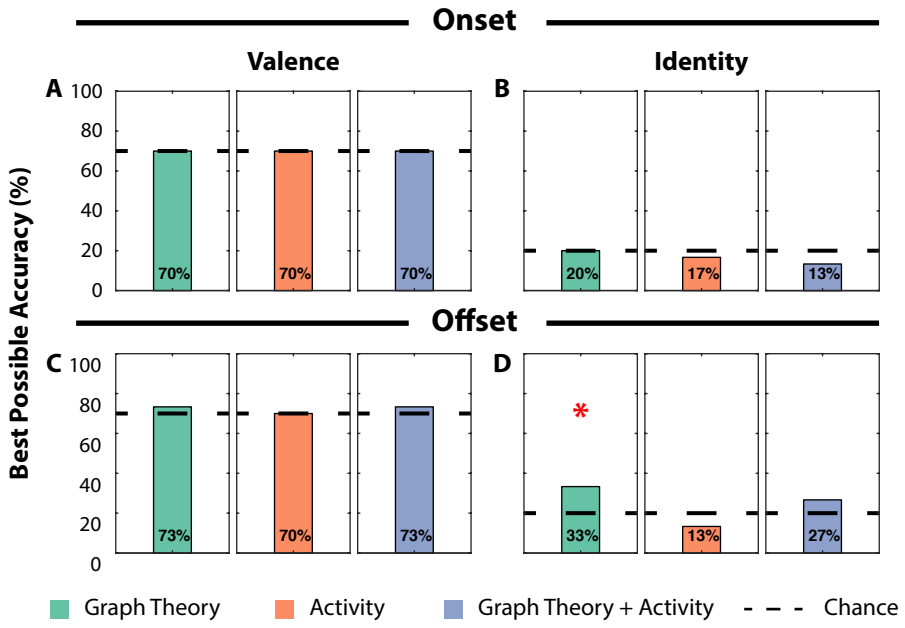


Figure 3.13 Logistic regression classifier attains above-chance classification accuracy for stimulus identity on Buffer sessions. Classification accuracy achieved on the first pulse of Buffer sessions using a Logistic Regression classifier trained using network features (green), neural activity features (orange) or both (blue). Accuracies are shown for stimulus valence and identity at stimulus onset (A, B) and offset (C, D), respectively. Red asterisks indicate significantly above-chance classification accuracy as determined with a permutation test (*$p < 0.025$). Black dotted lines indicate theoretical chance accuracy.

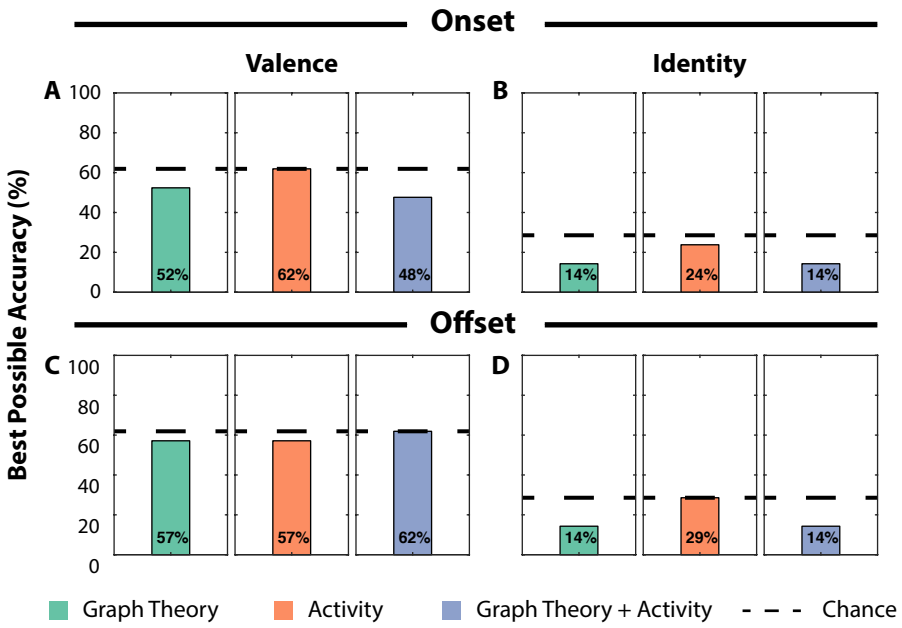


Figure 3.14 Logistic regression classifier does not attain above-chance classification accuracy for stimulus identity on Buffer sessions in 'naïve' animals. Classification accuracy achieved on the first pulse of Buffer sessions in naïve animals using a Logistic Regression classifier trained using network features (green), neural activity features (orange) or both (blue). Accuracies are shown for stimulus valence and identity at stimulus onset (A, B) and offset (C, D), respectively. We do not achieve significantly above-chance classification accuracy, assessed with permutation testing ($p > 0.05$). Black dotted lines indicate theoretical chance accuracy.

Table 3.3 Classifier results from permutation testing on full networks. Best performance achieved by Logistic Regression classifier on a specific classification task – namely, for a given session, pulse switch type, comparison, and one of three sets of features, correctly classify responses. The leave-one-out cross validation accuracy, the mean and standard deviation of the accuracies of a null distribution built using 1000 permutations of the labels, and the corresponding p-value, or relative position of its accuracy in the null distribution, are all listed. Values in **bold** attained significantly above-chance accuracies. Some tasks did not exceed chance (e.g., Valence on stimulus onset during Stimulus sessions with activity features), and this is indicated by a dashed line to indicate that no permutation testing was conducted. Accuracy on some classification tasks was higher when features were standardized (y = yes, n = no, y/n = same accuracy with or without standardization). Chance is 70% for Valence and 20% for Identity. GT = Graph Theory, Comb = Activity + Graph Theory.

| Session | Pulse Switch | Comparison | Features | Best Possible Accuracy (%) | Permutation score (%, mean±s.d.) | p-value | Standardized |
|---|---|---|---|---|---|---|---|
| Buffer | Onset | Valence | GT | 70 | - | - | n |
| | | | Activity | 70 | - | - | n |
| | | | Comb. | 70 | - | - | n |
| | | Identity | GT | 20 | - | - | y |
| | | | Activity | 17 | - | - | y |
| | | | Comb. | 13 | - | - | y |
| | Offset | Valence | GT | 73 | 61±7 | 0.074 | y |
| | | | Activity | 70 | - | - | n |
| | | | Comb. | 73 | 58±9 | 0.066 | y |
| | | Identity | **GT** | **33** | **16±8** | **0.021** | **y** |
| | | | Activity | 13 | - | - | y |
| | | | Comb. | 27 | 11±7 | 0.032 | n |
| Stimulus | Onset | Valence | GT | 70 | - | - | y/n |
| | | | Activity | 67 | - | - | n |
| | | | Comb. | 73 | 59±9 | 0.069 | y |
| | | Identity | **GT** | **40** | **16±8** | **0.004** | **y** |
| | | | Activity | 17 | - | - | y |
| | | | **Comb.** | **47** | **16±8** | **0.003** | **y** |
| | Offset | Valence | GT | 70 | - | - | n |
| | | | Activity | 70 | - | - | n |
| | | | Comb. | 67 | - | - | y |
| | | Identity | GT | 17 | - | - | y |
| | | | Activity | 23 | 15±8 | 0.196 | y |
| | | | Comb. | 33 | 16±8 | 0.038 | y |

### 3.4.5 Contributions of putative excitatory and inhibitory subnetworks to discrimination of stimulus identity

NMI can detect non-linear interactions between two signals but is unable to determine the sign of the interaction. For instance, two neurons can have high NMI, yet they may be positively or negatively correlated. The sign of the correlation is important because it implies different types of interactions, both of which are biologically meaningful – positive correlations are thought to indicate excitation, while negative correlations may imply inhibition, although this is not always true (e.g., if neurons A and B each receive input from a common, third neuron, then A and B will be positively correlated, in spite of the lack of a direct interaction between them). To identify the contributions of the positively and negatively correlated subnetworks to discriminating stimulus identity, we computed adjacency matrices based on Pearson's correlation and used the sign of those networks to split the NMI-based networks into two subnetworks: one composed of putatively excitatory interactions, and another composed of putatively inhibitory interactions. This enabled us to capture all non-linearities in neuronal interactions and analyze each subnetwork independently.

Unlike our results on the full network, we found no consistent differences between attractants and repellents on stimulus onset or offset for either the positively or negatively correlated subnetworks alone (Table 4). This suggests that the decrease in average betweenness centrality seen in the full network (Figure 8A,B) is driven by a decrease in the centrality of neurons that integrate both excitatory and inhibitory signals. On the other hand, several network features consistently changed on stimulus onset and offset for both

subnetworks in an identity-dependent manner (Table 4). While not all of these features are shared between the excitatory and inhibitory subnetworks, many, such as the network diameter and median weight, are. Finally, similar to the full network, there are few valence or identity-dependent changes on buffer onset, and a few on buffer offset (Table 5). Curiously, many of these identity-dependent changes are only seen in the negatively-correlated subnetworks, which indicates that the inhibitory subnetwork may carry a stronger memory of past stimulus.

Finally, we tried to classify stimulus valence and identity using network features solely derived from one subnetwork at a time. We found that the network features based on the positively correlated subnetwork contained as much discriminatory power as network features based on the full network (40% accuracy for both, chance: 20% permutation accuracy: 14±8%, p-value = 0.003; Figure 12E,F, and Table 6), while the negatively correlated subnetwork's features contained no discriminatory power (Figure 12E,F, and Table 7). This implies that stimulus identity most strongly modulates the pattern of excitation, but not inhibition. Oddly, neural activity features did not change the discriminatory power for the positively correlated subnetwork features (Table 6), which suggests that the interplay of excitation and inhibition together allows the context of neural activity to improve accuracy.

Overall, these additional analyses further demonstrate the value of using graph-theoretic features to decode stimulus properties. We anticipate that other parameters introduced when extracting features (e.g., modifying the size of time windows, inferring directionality, measuring the perceived intensity of a stimulus) may provide further biological insight.

Table 3.4 Graph-theoretic results from likelikood ratio test on generalized linear mixed-effects models for the Stimulus session on differently correlated networks. The positively (+) and negatively (-) correlated subnetworks are shown (columns). Results from the likelihood ratio test applied on a full vs null model. The full model includes information on either Valence or Identity in addition to the null model. The null model includes information on animal ID and time since first pulse. The p-values in **bold** indicate a significant difference in the data's likelihood when explained with the full model vs the null model; hence, the parameter (i.e., Valence or Identity) significantly improved model fit. The 'assortCoeff' cells are empty because they had negative numbers which could not be fit by a gamma distribution GLME. Other cells are empty because extreme outliers prevented convergence.

| Comparison | Pulse Switch | Graph Theory Feature | + | - |
|---|---|---|---|---|
| Valence | Onset | assortCoeff | | |
| | | avgBetweenCentrality | 0.050 | 0.046 |
| | | avgClusteringCoeff | 0.279 | 0.134 |
| | | avgDegDist | 0.753 | 0.982 |
| | | avgEigenvalue | 0.365 | 0.068 |
| | | avgLocalEff | 0.225 | 0.136 |
| | | avgNeighborDeg | 0.328 | 0.269 |
| | | avgParticipationCoeff | 0.891 | **0.006** |
| | | avgShortestPaths | 0.072 | 0.103 |
| | | avgWeight | 0.259 | 0.117 |
| | | density | 0.754 | 0.979 |
| | | diameter | 0.076 | 0.175 |
| | | globalEff | 0.194 | 0.163 |
| | | maxEigenvalue | 0.600 | 0.227 |
| | | medianWeight | 0.142 | 0.046 |
| | | modularity | 0.274 | 0.674 |
| | | numComponents | 0.766 | 0.766 |
| | | numEdges | 0.731 | 0.780 |
| | | numModules | 0.476 | **0.014** |
| | | numNodes | 0.733 | 0.733 |
| | | radius | 0.669 | 0.330 |
| | | transitivity | 0.317 | 0.127 |
| | Offset | assortCoeff | | |
| | | avgBetweenCentrality | 0.161 | 0.065 |
| | | avgClusteringCoeff | 0.799 | 0.537 |
| | | avgDegDist | 0.584 | 0.871 |
| | | avgEigenvalue | 0.835 | 0.799 |
| | | avgLocalEff | 0.756 | 0.881 |
| | | avgNeighborDeg | 0.973 | 0.381 |

Table 3.4 Graph-theoretic results from likelikood ratio test on generalized linear mixed-effects models for the Stimulus session on differently correlated networks (continued).

| Comparison | Pulse Switch | Graph Theory Feature | + | - |
|---|---|---|---|---|
| Valence | Offset | avgParticipationCoeff | **0.022** | 0.830 |
| | | avgShortestPaths | 0.334 | 0.139 |
| | | avgWeight | 0.814 | 0.570 |
| | | density | 0.569 | 0.889 |
| | | diameter | 0.469 | 0.031 |
| | | globalEff | 0.920 | 0.503 |
| | | maxEigenvalue | 0.554 | 0.570 |
| | | medianWeight | 0.535 | 0.526 |
| | | modularity | 0.250 | 0.041 |
| | | numComponents | 0.056 | 0.056 |
| | | numEdges | 0.196 | 0.176 |
| | | numModules | 0.213 | 0.482 |
| | | numNodes | 0.110 | 0.110 |
| | | radius | 0.672 | 0.340 |
| | | transitivity | 0.924 | 0.513 |
| Identity | Onset | assortCoeff | | |
| | | avgBetweenCentrality | 0.481 | **0.001** |
| | | avgClusteringCoeff | **0.010** | 0.060 |
| | | avgDegDist | 0.577 | 0.641 |
| | | avgEigenvalue | **0.017** | **0.020** |
| | | avgLocalEff | **0.009** | **0.005** |
| | | avgNeighborDeg | 0.066 | **0.002** |
| | | avgParticipationCoeff | **0.001** | 0.204 |
| | | avgShortestPaths | **0.013** | **0.005** |
| | | avgWeight | **0.017** | **0.003** |
| | | density | 0.549 | 0.661 |
| | | diameter | **0.000** | **0.004** |
| | | globalEff | 0.028 | **0.006** |
| | | maxEigenvalue | 0.211 | **0.005** |
| | | medianWeight | **0.008** | **0.001** |
| | | modularity | **0.020** | **0.000** |
| | | numComponents | 0.032 | 0.032 |
| | | numEdges | 0.287 | **0.002** |
| | | numModules | 0.033 | 0.031 |
| | | numNodes | **0.003** | **0.003** |
| | | radius | 0.470 | 0.166 |
| | | transitivity | 0.028 | 0.064 |
| | Offset | assortCoeff | | |
| | | avgBetweenCentrality | 0.219 | 0.065 |
| | | avgClusteringCoeff | 0.053 | **0.023** |

Table 3.4 Graph-theoretic results from likelikood ratio test on generalized linear mixed-effects models for the Stimulus session on differently correlated networks (continued).

| Comparison | Pulse Switch | Graph Theory Feature | + | - |
|---|---|---|---|---|
| Identity | Offset | avgDegDist | 0.391 | 0.302 |
| | | avgEigenvalue | 0.097 | **0.004** |
| | | avgLocalEff | 0.034 | **0.008** |
| | | avgNeighborDeg | 0.033 | **0.017** |
| | | avgParticipationCoeff | **0.025** | 0.920 |
| | | avgShortestPaths | 0.078 | 0.072 |
| | | avgWeight | 0.046 | **0.013** |
| | | density | 0.395 | 0.302 |
| | | diameter | 0.044 | 0.042 |
| | | globalEff | 0.034 | **0.013** |
| | | maxEigenvalue | 0.034 | **0.008** |
| | | medianWeight | **0.025** | **0.004** |
| | | modularity | 0.192 | **0.018** |
| | | numComponents | 0.041 | 0.041 |
| | | numEdges | **0.020** | 0.062 |
| | | numModules | 0.598 | 0.619 |
| | | numNodes | 0.030 | 0.030 |
| | | radius | 0.542 | 0.317 |
| | | transitivity | 0.077 | **0.023** |

Table 3.5 Graph-theoretic results from likelikood ratio test on generalized linear mixed-effects models for the Buffer session on differently correlated networks. The positively (+) and negatively (-) correlated subnetworks are shown (columns). Results from the likelihood ratio test applied on a full vs null model. The full model includes information on either Valence or Identity in addition to the null model. The null model includes information on animal ID and time since first pulse. The p-values in **bold** indicate a significant difference in the data's likelihood when explained with the full model vs the null model; hence, the parameter (i.e., Valence or Identity) significantly improved model fit. The 'assortCoeff' cells are empty because they had negative numbers which could not be fit by a gamma distribution GLME. Other cells are empty because extreme outliers prevented convergence.

| Comparison | Pulse Switch | Graph Theory Feature | + | - |
|---|---|---|---|---|
| Valence | Onset | assortCoeff | | |
| | | avgBetweenCentrality | 0.074 | 0.860 |
| | | avgClusteringCoeff | 0.490 | |
| | | avgDegDist | 0.311 | 0.261 |
| | | avgEigenvalue | 0.419 | 0.364 |
| | | avgLocalEff | 0.394 | 0.532 |
| | | avgNeighborDeg | 0.193 | 0.308 |
| | | avgParticipationCoeff | 0.600 | 0.696 |
| | | avgShortestPaths | 0.234 | 0.340 |
| | | avgWeight | 0.392 | 0.385 |
| | | density | 0.321 | 0.258 |
| | | diameter | 0.626 | 0.698 |
| | | globalEff | 0.212 | 0.297 |
| | | maxEigenvalue | 0.511 | 0.715 |
| | | medianWeight | 0.137 | 0.387 |
| | | modularity | 0.048 | 0.857 |
| | | numComponents | 0.626 | 0.626 |
| | | numEdges | 0.113 | 0.705 |
| | | numModules | 0.527 | 0.815 |
| | | numNodes | 0.303 | 0.303 |
| | | radius | 0.397 | 0.639 |
| | | transitivity | 0.403 | **0.004** |
| | Offset | assortCoeff | | |
| | | avgBetweenCentrality | 0.056 | 0.695 |
| | | avgClusteringCoeff | 0.344 | 0.205 |
| | | avgDegDist | 0.178 | 0.054 |
| | | avgEigenvalue | 0.344 | 0.345 |
| | | avgLocalEff | 0.319 | 0.214 |
| | | avgNeighborDeg | 0.284 | 0.395 |

Table 3.5 Graph-theoretic results from likelikood ratio test on generalized linear mixed-effects models for the Buffer session on differently correlated networks (continued).

| Comparison | Pulse Switch | Graph Theory Feature | + | - |
|---|---|---|---|---|
| Valence | Offset | avgParticipationCoeff | 0.122 | 0.551 |
| | | avgShortestPaths | 0.531 | 0.512 |
| | | avgWeight | 0.371 | 0.322 |
| | | density | 0.180 | 0.052 |
| | | diameter | 0.648 | 0.443 |
| | | globalEff | 0.297 | 0.483 |
| | | maxEigenvalue | 0.439 | 0.566 |
| | | medianWeight | 0.269 | 0.251 |
| | | modularity | 0.071 | 0.331 |
| | | numComponents | 0.606 | 0.606 |
| | | numEdges | 0.238 | 0.388 |
| | | numModules | 0.997 | 0.113 |
| | | numNodes | 0.819 | 0.819 |
| | | radius | 0.535 | 0.243 |
| | | transitivity | 0.421 | 0.367 |
| Identity | Onset | assortCoeff | | |
| | | avgBetweenCentrality | 0.114 | 0.813 |
| | | avgClusteringCoeff | 0.972 | 0.757 |
| | | avgDegDist | 0.421 | 0.465 |
| | | avgEigenvalue | 0.759 | 0.748 |
| | | avgLocalEff | 0.952 | 0.124 |
| | | avgNeighborDeg | 0.654 | 0.914 |
| | | avgParticipationCoeff | 0.382 | 0.035 |
| | | avgShortestPaths | 0.560 | 0.637 |
| | | avgWeight | 0.933 | 0.902 |
| | | density | 0.436 | 0.452 |
| | | diameter | 0.813 | 0.508 |
| | | globalEff | 0.829 | 0.900 |
| | | maxEigenvalue | 0.698 | 0.844 |
| | | medianWeight | 0.903 | 0.801 |
| | | modularity | 0.087 | 0.779 |
| | | numComponents | 0.756 | 0.756 |
| | | numEdges | 0.099 | 0.978 |
| | | numModules | 0.787 | 0.165 |
| | | numNodes | 0.367 | 0.367 |
| | | radius | 0.447 | 0.576 |
| | | transitivity | 0.943 | 0.067 |
| | Offset | assortCoeff | | |
| | | avgBetweenCentrality | 0.455 | 0.775 |
| | | avgClusteringCoeff | 0.049 | **0.022** |

Table 3.5 Graph-theoretic results from likelikood ratio test on generalized linear mixed-effects models for the Buffer session on differently correlated networks (continued).

| Comparison | Pulse Switch | Graph Theory Feature | + | - |
|---|---|---|---|---|
| Identity | Offset | avgDegDist | 0.741 | 0.420 |
| | | avgEigenvalue | 0.038 | **0.008** |
| | | avgLocalEff | 0.040 | **0.006** |
| | | avgNeighborDeg | 0.039 | **0.010** |
| | | avgParticipationCoeff | 0.576 | 0.602 |
| | | avgShortestPaths | 0.136 | 0.123 |
| | | avgWeight | 0.036 | 0.029 |
| | | density | 0.746 | 0.416 |
| | | diameter | 0.233 | 0.190 |
| | | globalEff | 0.035 | **0.016** |
| | | maxEigenvalue | 0.048 | **0.011** |
| | | medianWeight | 0.052 | 0.033 |
| | | modularity | 0.472 | 0.862 |
| | | numComponents | 0.222 | 0.222 |
| | | numEdges | 0.419 | 0.543 |
| | | numModules | 0.379 | 0.231 |
| | | numNodes | 0.658 | 0.658 |
| | | radius | 0.637 | 0.171 |
| | | transitivity | 0.063 | 0.027 |

Table 3.6 Classifier results from permutation testing on networks with positively correlated neurons. Best performance achieved by Logistic Regression classifier on a specific classification task – namely, for a given session, pulse switch type, comparison, and one of three sets of features, correctly classify responses. The leave-one-out cross validation accuracy, the mean and standard deviation of the accuracies of a null distribution built using 1000 permutations of the labels, and the corresponding p-value, or relative position of its accuracy in the null distribution, are all listed. Values in **bold** attained significantly above-chance accuracies. Some tasks did not exceed chance (e.g., Valence on stimulus onset during Stimulus sessions with activity features), and this is indicated by a dashed line to indicate that no permutation testing was conducted. Accuracy on some classification tasks was higher when features were standardized (y = yes, n = no, y/n = same accuracy with or without standardization). Chance is 70% for Valence and 20% for Identity. GT = Graph Theory, Comb = Activity + Graph Theory.

| Session | Pulse Switch | Comparison | Features | Best Possible Accuracy (%) | Permutation score (%, mean±s.d.) | p-value | Standardized |
|---|---|---|---|---|---|---|---|
| Buffer | Onset | Valence | GT | 63 | - | - | n |
| | | | Activity | 70 | - | - | n |
| | | | Comb. | 63 | - | - | n |
| | | Identity | GT | 17 | - | - | y |
| | | | Activity | 17 | - | - | y |
| | | | Comb. | 23 | 16±7 | 0.235 | y |
| | Offset | Valence | GT | 67 | - | - | y/n |
| | | | Activity | 70 | - | - | n |
| | | | Comb. | 63 | - | - | y/n |
| | | Identity | GT | 23 | 16±8 | 0.236 | y |
| | | | Activity | 13 | - | - | y |
| | | | Comb. | 20 | - | - | n |
| Stimulus | Onset | Valence | GT | 67 | - | - | y/n |
| | | | Activity | 67 | - | - | n |
| | | | Comb. | 60 | - | - | y/n |
| | | Identity | **GT** | **40** | **14±8** | **0.003** | **n** |
| | | | Activity | 17 | - | - | y |
| | | | **Comb.** | **40** | **15±8** | **0.004** | **n** |
| | Offset | Valence | GT | 73 | 59±8 | 0.064 | y |
| | | | Activity | 70 | - | - | n |
| | | | Comb. | 70 | - | - | n |
| | | Identity | GT | 27 | 16±7 | 0.102 | y |
| | | | Activity | 23 | 15±8 | 0.196 | y |
| | | | Comb. | 30 | 16±7 | 0.061 | y |

Table 3.7 Classifier results from permutation testing on networks with negatively correlated neurons. Best performance achieved by Logistic Regression classifier on a specific classification task – namely, for a given session, pulse switch type, comparison, and one of three sets of features, correctly classify responses. The leave-one-out cross validation accuracy, the mean and standard deviation of the accuracies of a null distribution built using 1000 permutations of the labels, and the corresponding p-value, or relative position of its accuracy in the null distribution, are all listed. Values in **bold** attained significantly above-chance accuracies. Some tasks did not exceed chance (e.g., Valence on stimulus onset during Stimulus sessions with activity features), and this is indicated by a dashed line to indicate that no permutation testing was conducted. Accuracy on some classification tasks was higher when features were standardized (y = yes, n = no, y/n = same accuracy with or without standardization). Chance is 70% for Valence and 20% for Identity. GT = Graph Theory, Comb = Activity + Graph Theory.

| Session | Pulse Switch | Comparison | Features | Best Possible Accuracy (%) | Permutation score (%, mean±s.d.) | p-value | Standardized |
|---|---|---|---|---|---|---|---|
| Buffer | Onset | Valence | GT | 63 | - | - | y |
| | | | Activity | 70 | - | - | n |
| | | | Comb. | 63 | - | - | y |
| | | Identity | GT | 20 | - | - | y |
| | | | Activity | 17 | - | - | y |
| | | | Comb. | 20 | - | - | y |
| | Offset | Valence | GT | 63 | - | - | n |
| | | | Activity | 70 | - | - | n |
| | | | Comb. | 63 | - | - | n |
| | | Identity | GT | 23 | 16±7 | 0.234 | y |
| | | | Activity | 13 | - | - | y |
| | | | Comb. | 20 | - | - | n |
| Stimulus | Onset | Valence | GT | 77 | 60±8 | 0.040 | y |
| | | | Activity | 67 | - | - | n |
| | | | Comb. | 73 | 58±9 | 0.071 | y/n |
| | | Identity | GT | 33 | 16±8 | 0.034 | y |
| | | | Activity | 17 | - | - | y |
| | | | Comb. | 30 | 14±8 | 0.051 | y/n |
| | Offset | Valence | GT | 67 | - | - | n |
| | | | Activity | 70 | - | - | n |
| | | | Comb. | 70 | - | - | y |
| | | Identity | GT | 20 | - | - | y |
| | | | Activity | 23 | 15±8 | 0.196 | y |
| | | | Comb. | 33 | 16±7 | 0.031 | y |

## 3.5 Discussion

A central challenge in neuroscience is to develop tools that can uncover how stimulus properties, such as valence and identity, are encoded within neural networks. We monitored changes in the activity of over 40 neurons in the head of *C. elegans* as it experienced diverse chemical stimuli. We found that some activity statistics, such as the mean and standard deviation of neural activity and Fourier-based frequency measures, are modulated by, yet unable to, distinguish stimulus valence and identity. We then extracted graph-theoretic features from time-series activity traces of neurons and found improved ability to predict stimulus identity. Our results suggest that some stimulus properties can be decoded using network features, which could be useful in instances where neuron labels are unknown or difficult to map across animals.

We used normalized mutual information to generate functional connectivity networks from neural activity traces. In contrast, recent work has tried to infer causal networks from activity traces using methods such as adaptive, sparsity-constrained Granger causality (Sheikhattar et al., 2018), network deconvolution (Feizi et al., 2013), convex risk minimization (Sefer and Kingsford, 2015), and convergent cross mapping (Sugihara et al., 2012). Some of these methods, however, make assumptions about the data type and nature of causality that may not be true here; e.g., they assume spiking data as opposed to graded potentials, or they assume specific models of information spread, such as those used in epidemiology. While we used a relatively simple approach, our method is general and allows for any network inference algorithm to be plugged into our framework.

The median network weight, transitivity, and max eigenvalue all emerged as useful features for discriminating stimulus identity. This implies that neural networks likely use changes in strength of interactions, especially amongst local triplets of neurons, to facilitate widespread communication and process stimulus identity. Consistently, amongst the five stimuli tested, NaCl always attained the greatest increase in median weight, max eigenvalue, and transitivity, which may reflect its ability to use both salt and odor circuitry to encode sensory information (Leinwand and Chalasani, 2013). The rest of the chemicals induced similar increases in the max eigenvalue and transitivity of the nematode neural network on stimulus onset, yet had more differentiated responses on stimulus offset, which indicates that the initial detection of an odorant might evoke core changes in neural network organization, supplemented with additional chemical-specific changes.

Stimulus valence, on the other hand, modulated the network's average betweenness centrality. While repellents led to network activity with a smaller average betweenness centrality, attractants did not produce substantial changes in centrality. This implies that repellent information is likely processed by fewer central neurons bridging disparate parts of the network, while attractants may require a large number of neurons across the entire network. Consistently, previous studies have shown that attractants are typically encoded by a combination of multiple sensory neurons (Leinwand et al., 2015), while the onset and offset of the repellent 2-nonanone is detected by the AWB chemosensory neurons (Ha et al., 2010).

While we chose several popular graph-theoretic features to study diverse aspects of network organization (Rubinov and Sporns, 2010; Rubinov and Sporns, 2011), this list

is not exhaustive, and there may be other features that can better discriminate stimulus properties. We also focused on fully-connected weighted networks, as opposed to sparse networks by applying an arbitrary threshold to remove weak edges. Sparse network analysis depends on the precise threshold and might result in data that is difficult to interpret (van den Heuvel et al., 2017). Consistently, attempts to use three different proportional thresholds to filter network weights showed that different features emerged as significant depending on the threshold chosen (Tables 8, 9), and the ability to classify stimulus identity was similarly variable (Tables 10 – 12). Finally, we used a basic machine learning approach to quantitatively test the power of using network features to classify stimulus properties. While we both used sample sizes (n=30 animals) comparable with prior studies and adopted standard approaches to avoid over-fitting (e.g., cross-validation, permutation testing), we nonetheless caution that building reliable machine learning models with relatively small datasets can be sensitive to a few data points. As it becomes experimentally easier to generate larger datasets with more neurons across many more conditions in other species, we hope our framework of using graph-theoretic features of network activity to understand neural function can be further improved.

Table 3.8 Graph-theoretic results from likelikood ratio test on generalized linear mixed-effects models for the Buffer session on thresholded networks. Only the top 30%, 20%, or 10% of weights were kept in each network (columns). Results from the likelihood ratio test applied on a full vs null model. The full model includes information on either Valence or Identity in addition to the null model. The null model includes information on animal ID and time since first pulse. The p-values in **bold** indicate a significant difference in the data's likelihood when explained with the full model vs the null model; hence, the parameter (i.e., Valence or Identity) significantly improved model fit. The 'assortCoeff' cells are empty because they had negative numbers which could not be fit by a gamma distribution GLME. Other cells are empty because extreme outliers prevented convergence.

| Comparison | Pulse Switch | Graph Theory Feature | 30% | 20% | 10% |
|---|---|---|---|---|---|
| Valence | Onset | assortCoeff | | | |
| | | avgBetweenCentrality | 0.321 | 0.836 | 0.152 |
| | | avgClusteringCoeff | 0.220 | 0.630 | 0.680 |
| | | avgDegDist | 0.981 | 0.893 | 0.368 |
| | | avgEigenvalue | 0.370 | 0.629 | 0.465 |
| | | avgLocalEff | 0.234 | 0.640 | 0.674 |
| | | avgNeighborDeg | 0.346 | 0.426 | 0.561 |
| | | avgParticipationCoeff | 0.035 | 0.583 | 0.972 |
| | | avgShortestPaths | 0.417 | 0.481 | 0.359 |
| | | avgWeight | 0.352 | 0.414 | 0.596 |
| | | density | 0.982 | 0.897 | 0.367 |
| | | diameter | 0.238 | 0.491 | 0.199 |
| | | globalEff | 0.333 | 0.407 | 0.371 |
| | | maxEigenvalue | 0.494 | 0.595 | 0.732 |
| | | medianWeight | 0.212 | 0.244 | 0.438 |
| | | modularity | 0.136 | 0.216 | |
| | | numComponents | 0.630 | 0.795 | 0.552 |
| | | numEdges | 0.838 | 0.246 | 0.811 |
| | | numModules | 0.837 | 0.986 | 0.455 |
| | | numNodes | 0.873 | 0.757 | 0.332 |
| | | radius | 0.203 | 0.159 | 0.087 |
| | | transitivity | 0.307 | 0.401 | 0.998 |
| | Offset | assortCoeff | | | |
| | | avgBetweenCentrality | 0.201 | 0.711 | 0.865 |
| | | avgClusteringCoeff | 0.259 | 0.346 | 0.504 |
| | | avgDegDist | 0.506 | 0.622 | 0.626 |
| | | avgEigenvalue | 0.441 | 0.573 | 0.890 |
| | | avgLocalEff | 0.270 | 0.412 | 0.541 |
| | | avgNeighborDeg | 0.406 | 0.394 | 0.417 |

Table 3.8 Graph-theoretic results from likelikood ratio test on generalized linear mixed-effects models for the Buffer session on thresholded networks (continued).

| Comparison | Pulse Switch | Graph Theory Feature | 30% | 20% | 10% |
|---|---|---|---|---|---|
| Valence | Offset | avgParticipationCoeff | 0.595 | 0.941 | 0.253 |
| | | avgShortestPaths | 0.891 | 0.849 | 0.996 |
| | | avgWeight | 0.403 | 0.457 | 0.527 |
| | | density | 0.502 | 0.620 | 0.627 |
| | | diameter | 0.595 | 0.574 | 0.785 |
| | | globalEff | 0.350 | 0.433 | 0.577 |
| | | maxEigenvalue | 0.360 | 0.408 | 0.457 |
| | | medianWeight | 0.347 | 0.443 | 0.605 |
| | | modularity | 0.743 | 0.449 | 0.872 |
| | | numComponents | 0.496 | 0.492 | 0.503 |
| | | numEdges | 0.673 | 0.029 | 0.884 |
| | | numModules | 0.891 | 0.810 | 0.581 |
| | | numNodes | 0.676 | 0.666 | 0.718 |
| | | radius | 0.356 | 0.346 | 0.220 |
| | | transitivity | 0.338 | 0.398 | 0.387 |
| Identity | Onset | assortCoeff | | | |
| | | avgBetweenCentrality | 0.154 | 0.086 | 0.443 |
| | | avgClusteringCoeff | 0.992 | 0.990 | 0.891 |
| | | avgDegDist | 0.926 | 0.903 | 0.996 |
| | | avgEigenvalue | 0.569 | 0.551 | 0.535 |
| | | avgLocalEff | 0.972 | 0.987 | 0.830 |
| | | avgNeighborDeg | 0.979 | 0.979 | 0.997 |
| | | avgParticipationCoeff | 0.516 | 0.247 | 0.545 |
| | | avgShortestPaths | 0.496 | 0.470 | 0.403 |
| | | avgWeight | 0.940 | 0.958 | 0.971 |
| | | density | 0.928 | 0.902 | 0.996 |
| | | diameter | 0.495 | 0.324 | 0.411 |
| | | globalEff | 0.881 | 0.936 | 0.941 |
| | | maxEigenvalue | 0.982 | 0.960 | 0.960 |
| | | medianWeight | 0.902 | 0.894 | 0.973 |
| | | modularity | 0.383 | 0.498 | |
| | | numComponents | 0.885 | 0.730 | 0.930 |
| | | numEdges | 0.985 | 0.873 | 0.632 |
| | | numModules | 0.722 | 0.667 | 0.662 |
| | | numNodes | 0.603 | 0.967 | 0.739 |
| | | radius | 0.453 | 0.534 | 0.722 |
| | | transitivity | 0.972 | 0.925 | 0.965 |
| | Offset | assortCoeff | | | |
| | | avgBetweenCentrality | 0.902 | 0.801 | 0.584 |
| | | avgClusteringCoeff | **0.005** | **0.007** | **0.011** |

Table 3.8 Graph-theoretic results from likelikood ratio test on generalized linear mixed-effects models for the Buffer session on thresholded networks (continued).

| Comparison | Pulse Switch | Graph Theory Feature | 30% | 20% | 10% |
|---|---|---|---|---|---|
| Identity | Offset | avgDegDist | 0.536 | 0.225 | 0.027 |
| | | avgEigenvalue | 0.173 | 0.191 | 0.055 |
| | | avgLocalEff | **0.008** | **0.018** | **0.013** |
| | | avgNeighborDeg | **0.008** | **0.004** | **0.002** |
| | | avgParticipationCoeff | 0.261 | 0.422 | 0.277 |
| | | avgShortestPaths | 0.165 | 0.129 | 0.031 |
| | | avgWeight | **0.016** | **0.016** | **0.014** |
| | | density | 0.535 | 0.224 | 0.026 |
| | | diameter | 0.187 | 0.189 | 0.063 |
| | | globalEff | 0.028 | 0.031 | **0.009** |
| | | maxEigenvalue | **0.013** | **0.014** | **0.007** |
| | | medianWeight | **0.024** | **0.022** | **0.014** |
| | | modularity | 0.146 | 0.305 | 0.306 |
| | | numComponents | 0.356 | 0.228 | 0.060 |
| | | numEdges | 0.281 | 0.161 | 0.889 |
| | | numModules | 0.027 | 0.559 | 0.217 |
| | | numNodes | 0.473 | 0.216 | 0.076 |
| | | radius | 0.710 | 0.628 | 0.434 |
| | | transitivity | **0.009** | **0.009** | **0.012** |

Table 3.9 Graph-theoretic results from likelikood ratio test on generalized linear mixed-effects models for the Stimulus session on thresholded networks. Only the top 30%, 20%, or 10% of weights were kept in each network (columns). Results from the likelihood ratio test applied on a full vs null model. The full model includes information on either Valence or Identity in addition to the null model. The null model includes information on animal ID and time since first pulse. The p-values in **bold** indicate a significant difference in the data's likelihood when explained with the full model vs the null model; hence, the parameter (i.e., Valence or Identity) significantly improved model fit. The 'assortCoeff' cells are empty because they had negative numbers which could not be fit by a gamma distribution GLME. Other cells are empty because extreme outliers prevented convergence.

| Comparison | Pulse Switch | Graph Theory Feature | 30% | 20% | 10% |
|---|---|---|---|---|---|
| Valence | Onset | assortCoeff | | | |
| | | avgBetweenCentrality | **0.009** | 0.114 | 0.814 |
| | | avgClusteringCoeff | 0.275 | 0.400 | 0.582 |
| | | avgDegDist | 0.631 | 0.978 | 0.954 |
| | | avgEigenvalue | 0.308 | 0.533 | 0.714 |
| | | avgLocalEff | 0.211 | 0.346 | 0.618 |
| | | avgNeighborDeg | 0.333 | 0.439 | 0.708 |
| | | avgParticipationCoeff | 0.495 | 0.474 | 0.635 |
| | | avgShortestPaths | 0.159 | 0.216 | 0.327 |
| | | avgWeight | 0.271 | 0.328 | 0.436 |
| | | density | 0.631 | 0.974 | 0.969 |
| | | diameter | 0.101 | 0.224 | 0.185 |
| | | globalEff | 0.318 | 0.438 | 0.610 |
| | | maxEigenvalue | 0.484 | 0.648 | 0.790 |
| | | medianWeight | 0.195 | 0.252 | 0.340 |
| | | modularity | 0.578 | 0.615 | 0.738 |
| | | numComponents | 0.106 | 0.526 | 0.556 |
| | | numEdges | 0.486 | 0.685 | 0.207 |
| | | numModules | 0.342 | 0.534 | 0.669 |
| | | numNodes | 0.536 | 0.824 | 0.601 |
| | | radius | 0.247 | 0.321 | 0.370 |
| | | transitivity | 0.397 | 0.545 | 0.633 |
| | Offset | assortCoeff | | | |
| | | avgBetweenCentrality | **0.001** | **0.000** | 0.731 |
| | | avgClusteringCoeff | 0.913 | 0.905 | 0.352 |
| | | avgDegDist | 0.155 | 0.554 | 0.183 |
| | | avgEigenvalue | 0.606 | 0.784 | 0.787 |
| | | avgLocalEff | 0.588 | 0.862 | 0.370 |
| | | avgNeighborDeg | 0.996 | 0.926 | 0.456 |

Table 3.9 Graph-theoretic results from likelikood ratio test on generalized linear mixed-effects models for the Stimulus session on thresholded networks (continued).

| Comparison | Pulse Switch | Graph Theory Feature | 30% | 20% | 10% |
|---|---|---|---|---|---|
| Valence | Offset | avgParticipationCoeff | 0.407 | 0.746 | 0.684 |
| | | avgShortestPaths | 0.132 | 0.096 | 0.294 |
| | | avgWeight | 0.630 | 0.772 | 0.940 |
| | | density | 0.155 | 0.552 | 0.180 |
| | | diameter | **0.007** | **0.003** | 0.172 |
| | | globalEff | 0.840 | 0.833 | 0.606 |
| | | maxEigenvalue | 0.561 | 0.536 | 0.285 |
| | | medianWeight | 0.468 | 0.622 | |
| | | modularity | 0.188 | 0.281 | 0.277 |
| | | numComponents | 0.467 | 0.089 | 0.131 |
| | | numEdges | 0.487 | 0.264 | 0.688 |
| | | numModules | 0.236 | 0.179 | 0.851 |
| | | numNodes | 0.224 | 0.842 | 0.373 |
| | | radius | 0.717 | 0.918 | 0.332 |
| | | transitivity | 0.768 | 0.552 | 0.297 |
| Identity | Onset | assortCoeff | | | |
| | | avgBetweenCentrality | **0.011** | 0.422 | 0.223 |
| | | avgClusteringCoeff | **0.009** | **0.025** | 0.082 |
| | | avgDegDist | 0.095 | 0.574 | 0.870 |
| | | avgEigenvalue | **0.017** | 0.042 | 0.206 |
| | | avgLocalEff | **0.008** | 0.034 | 0.089 |
| | | avgNeighborDeg | **0.019** | 0.034 | 0.080 |
| | | avgParticipationCoeff | 0.045 | **0.000** | **0.003** |
| | | avgShortestPaths | **0.018** | 0.041 | 0.116 |
| | | avgWeight | **0.008** | **0.013** | **0.022** |
| | | density | 0.095 | 0.576 | 0.870 |
| | | diameter | 0.109 | 0.187 | 0.554 |
| | | globalEff | **0.025** | 0.063 | 0.183 |
| | | maxEigenvalue | 0.039 | 0.088 | 0.204 |
| | | medianWeight | **0.005** | **0.011** | **0.021** |
| | | modularity | 0.584 | 0.614 | 0.575 |
| | | numComponents | **0.018** | 0.240 | 0.650 |
| | | numEdges | 0.096 | 0.699 | 0.467 |
| | | numModules | 0.051 | 0.106 | 0.505 |
| | | numNodes | 0.047 | 0.387 | 0.722 |
| | | radius | 0.162 | 0.171 | 0.312 |
| | | transitivity | **0.012** | **0.022** | 0.073 |
| | Offset | assortCoeff | | | |
| | | avgBetweenCentrality | **0.002** | **0.013** | 0.420 |
| | | avgClusteringCoeff | **0.009** | **0.011** | **0.004** |

Table 3.9 Graph-theoretic results from likelikood ratio test on generalized linear mixed-effects models for the Stimulus session on thresholded networks (continued).

| Comparison | Pulse Switch | Graph Theory Feature | 30% | 20% | 10% |
|---|---|---|---|---|---|
| Identity | Offset | avgDegDist | 0.440 | 0.325 | 0.135 |
| | | avgEigenvalue | 0.256 | 0.062 | 0.098 |
| | | avgLocalEff | **0.017** | **0.019** | **0.006** |
| | | avgNeighborDeg | **0.008** | **0.010** | **0.005** |
| | | avgParticipationCoeff | 0.271 | 0.070 | 0.114 |
| | | avgShortestPaths | 0.160 | 0.098 | 0.072 |
| | | avgWeight | **0.019** | **0.023** | 0.035 |
| | | density | 0.439 | 0.323 | 0.134 |
| | | diameter | 0.129 | 0.040 | 0.067 |
| | | globalEff | 0.037 | 0.033 | 0.035 |
| | | maxEigenvalue | **0.009** | **0.008** | **0.009** |
| | | medianWeight | **0.012** | **0.016** | 0.029 |
| | | modularity | 0.118 | 0.089 | 0.609 |
| | | numComponents | 0.833 | 0.227 | 0.095 |
| | | numEdges | 0.829 | 0.248 | 0.620 |
| | | numModules | 0.824 | 0.698 | 0.031 |
| | | numNodes | 0.394 | 0.615 | 0.324 |
| | | radius | 0.512 | 0.291 | 0.141 |
| | | transitivity | **0.006** | **0.005** | **0.007** |

Table 3.10 Classifier results from permutation testing on networks with the top 30% of weights. Best performance achieved by Logistic Regression classifier on a specific classification task – namely, for a given session, pulse switch type, comparison, and one of three sets of features, correctly classify responses. The leave-one-out cross validation accuracy, the mean and standard deviation of the accuracies of a null distribution built using 1000 permutations of the labels, and the corresponding p-value, or relative position of its accuracy in the null distribution, are all listed. Values in **bold** attained significantly above-chance accuracies. Some tasks did not exceed chance (e.g., Valence on stimulus onset during Stimulus sessions with activity features), and this is indicated by a dashed line to indicate that no permutation testing was conducted. Accuracy on some classification tasks was higher when features were standardized (y = yes, n = no, y/n = same accuracy with or without standardization). Chance is 70% for Valence and 20% for Identity. GT = Graph Theory, Comb = Activity + Graph Theory.

| Session | Pulse Switch | Comparison | Features | Best Possible Accuracy (%) | Permutation score (%, mean±s.d.) | p-value | Standardized |
|---|---|---|---|---|---|---|---|
| Buffer | Onset | Valence | GT | 67 | - | - | n |
| | | | Activity | 67 | - | - | y |
| | | | Comb. | 70 | - | - | n |
| | | Identity | GT | 13 | - | - | n |
| | | | Activity | 17 | - | - | y |
| | | | Comb. | 23 | 17±8 | 0.265 | y |
| | Offset | Valence | GT | 57 | - | - | n |
| | | | Activity | 70 | - | - | n |
| | | | Comb. | 60 | - | - | n |
| | | Identity | GT | 23 | 15±8 | 0.209 | y |
| | | | Activity | 13 | - | - | y |
| | | | Comb. | 20 | - | - | n |
| Stimulus | Onset | Valence | GT | 73 | 60±8 | 0.065 | y/n |
| | | | Activity | 67 | - | - | n |
| | | | Comb. | 73 | 58±9 | 0.054 | y/n |
| | | Identity | **GT** | **47** | **14±8** | **0.001** | **y/n** |
| | | | Activity | 17 | - | - | y |
| | | | **Comb.** | **43** | **14±8** | **0.002** | **n** |
| | Offset | Valence | GT | 63 | - | - | n |
| | | | Activity | 70 | - | - | n |
| | | | Comb. | 67 | - | - | y |
| | | Identity | GT | 27 | 16±8 | 0.115 | y |
| | | | Activity | 23 | 15±8 | 0.196 | y |
| | | | **Comb.** | **37** | **16±8** | **0.022** | **y** |

Table 3.11 Classifier results from permutation testing on networks with the top 20% of weights. Best performance achieved by Logistic Regression classifier on a specific classification task – namely, for a given session, pulse switch type, comparison, and one of three sets of features, correctly classify responses. The leave-one-out cross validation accuracy, the mean and standard deviation of the accuracies of a null distribution built using 1000 permutations of the labels, and the corresponding p-value, or relative position of its accuracy in the null distribution, are all listed. Values in **bold** attained significantly above-chance accuracies. Some tasks did not exceed chance (e.g., Valence on stimulus onset during Stimulus sessions with activity features), and this is indicated by a dashed line to indicate that no permutation testing was conducted. Accuracy on some classification tasks was higher when features were standardized (y = yes, n = no, y/n = same accuracy with or without standardization). Chance is 70% for Valence and 20% for Identity. GT = Graph Theory, Comb = Activity + Graph Theory.

| Session | Pulse Switch | Comparison | Features | Best Possible Accuracy (%) | Permutation score (%, mean±s.d.) | p-value | Standardized |
|---|---|---|---|---|---|---|---|
| Buffer | Onset | Valence | GT | 63 | - | - | y |
| | | | Activity | 70 | - | - | n |
| | | | Comb. | 70 | - | - | y |
| | | Identity | GT | 17 | - | - | y |
| | | | Activity | 17 | - | - | y |
| | | | Comb. | 27 | 17±8 | 0.136 | y |
| | Offset | Valence | GT | 70 | - | - | y |
| | | | Activity | 70 | - | - | n |
| | | | Comb. | 70 | - | - | y |
| | | Identity | GT | 30 | 16±8 | 0.084 | y |
| | | | Activity | 13 | - | - | y |
| | | | Comb. | 23 | 17±8 | 0.249 | y |
| Stimulus | Onset | Valence | GT | 67 | - | - | n |
| | | | Activity | 67 | - | - | n |
| | | | Comb. | 73 | 58±9 | 0.057 | y |
| | | Identity | **GT** | **37** | **14±7** | **0.007** | **y/n** |
| | | | Activity | 17 | - | - | y |
| | | | Comb. | 27 | 13±7 | 0.071 | n |
| | Offset | Valence | GT | 57 | - | - | n |
| | | | Activity | 70 | - | - | n |
| | | | Comb. | 70 | - | - | y |
| | | Identity | GT | 30 | 16±8 | 0.069 | y |
| | | | Activity | 23 | 15±8 | 0.196 | y |
| | | | **Comb.** | **37** | **17±8** | **0.018** | **y** |

Table 3.12 Classifier results from permutation testing on networks with the top 10% of weights. Best performance achieved by Logistic Regression classifier on a specific classification task – namely, for a given session, pulse switch type, comparison, and one of three sets of features, correctly classify responses. The leave-one-out cross validation accuracy, the mean and standard deviation of the accuracies of a null distribution built using 1000 permutations of the labels, and the corresponding p-value, or relative position of its accuracy in the null distribution, are all listed. Values in **bold** attained significantly above-chance accuracies. Some tasks did not exceed chance (e.g., Valence on stimulus onset during Stimulus sessions with activity features), and this is indicated by a dashed line to indicate that no permutation testing was conducted. Accuracy on some classification tasks was higher when features were standardized (y = yes, n = no, y/n = same accuracy with or without standardization). Chance is 70% for Valence and 20% for Identity. GT = Graph Theory, Comb = Activity + Graph Theory.

| Session | Pulse Switch | Comparison | Features | Best Possible Accuracy (%) | Permutation score (%, mean±s.d.) | p-value | Standardized |
|---|---|---|---|---|---|---|---|
| Buffer | Onset | Valence | GT | 67 | - | - | n |
| | | | Activity | 70 | - | - | n |
| | | | Comb. | 67 | - | - | n |
| | | Identity | GT | 23 | 14±8 | 0.148 | n |
| | | | Activity | 17 | - | - | y |
| | | | Comb. | 27 | 17±8 | 0.155 | y |
| | Offset | Valence | GT | 57 | - | - | y |
| | | | Activity | 70 | - | - | n |
| | | | Comb. | 57 | - | - | n |
| | | Identity | GT | 13 | - | - | n |
| | | | Activity | 13 | - | - | y |
| | | | Comb. | 13 | - | - | y |
| Stimulus | Onset | Valence | GT | 60 | - | - | n |
| | | | Activity | 67 | - | - | n |
| | | | Comb. | 63 | - | - | y |
| | | Identity | GT | 23 | 16±8 | 0.215 | y |
| | | | Activity | 17 | - | - | y |
| | | | Comb. | 30 | 16±7 | 0.069 | y |
| | Offset | Valence | GT | 70 | - | - | n |
| | | | Activity | 60 | - | - | y |
| | | | Comb. | 60 | - | - | y/n |
| | | Identity | GT | 20 | - | - | y |
| | | | Activity | 23 | 15±8 | 0.196 | y |
| | | | Comb. | 23 | 16±8 | 0.215 | y |

## 3.6 Materials and Methods

### 3.6.1 Whole-brain calcium imaging

All imaging experiments were performed on a previously published strain (ZIM1048 *lite-1(ce314)X, msmIs4*; Nichols et al., 2017). We trapped 30 young adults in a modified olfactory chip (Chronis et al., 2007) that orients animals similarly (Schrodel et al., 2013). Changes in GCaMP fluorescence were monitored using a Zeiss LSM 880 Airyscan (1.27-1.62 volumes/second) while the animal's nose experienced buffer or one of five stimuli (Diacetyl $10^{-4}$ %vol/vol, $10^{-6}$ %vol/vol (Larsch et al., 2015; Hale et al., 2016), benzaldehyde $10^{-3}$ %vol/vol, $10^{-6}$ %vol/vol (Leinwand et al., 2015), isoamyl alcohol $10^{-5}$ %vol/vol, $10^{-7}$ %vol/vol (Chalasani et al., 2007; Yoshida et al., 2012), 2-nonanone $10^{-2}$ %vol/vol, $10^{-4}$ %vol/vol (Hale et al., 2016) and NaCl at an aversive 600mM (Chatzigeorgiou et al., 2013) and at an attractive 200mM (Wang et al., 2016) concentration). For each animal, we obtained a 21-minute recording with no stimulation ("Spontaneous"), a second 21-minute recording with M9 buffer changes ("Buffer") and a third 21-minute recording with stimuli changes ("Stimulus"). Buffer and Stimulus sessions were interleaved for different animals except for those experiencing 2-nonanone, when Buffer always preceded Stimulus. The Stimulus or Buffer pattern was adapted from Albrecht and Bargmann (2011).

### 3.6.2 Data processing

We first deconvolved the pixels using built-in Airyscan processing tools. We then corrected for motion using NormCorre (https://github.com/flatironinstitute/NoRMCorre) and extracted the raw fluorescence traces using CaImAn

(https://github.com/flatironinstitute/CaImAn-MATLAB) (Pnevmatikakis et al., 2013; Pnevmatikakis et al., 2014; Friedrich and Paninski, 2016; Pnevmatikakis et al., 2016; Pnevmatikakis et al., 2017; Giovannucci et al., 2019). We used multiple iterations using grids of decreasing size to analyze high concentration NaCl “Stimulus” trials, which had larger motion artefacts compared to other stimuli. Importantly, the low concentration NaCl “Stimulus” trials did not require this extra preprocessing step. Nine of thirty “Spontaneous” sessions had too much movement to correct, and were not further analyzed. To accurately identify all neurons in the head of the animal, we set the cutoff K, for the number of components to look for, to 140 (this is higher than the number of neurons previously detected in this strain (Nichols et al., 2017)) allowing the CaImAn algorithm to detect many neurons with a high signal-to-noise ratio as recommended by (Giovannucci et al., 2019). Hence, neurons with no change in fluorescence were not detected. Finally, we used custom software to manually verify that regions of interest extracted by our analysis pipeline qualitatively matched the video, and to eliminate non-neuronal ROIs (e.g., gut granules).

### 3.6.3 Measuring statistical features of neural activity

Each neuron’s activity trace was normalized within a session by the max fluorescence value reached in that 21-minute imaging session. To highlight the change in neural activity properties after a stimulus switch, we normalized the value of the property to its value pre-switch. For example, for stimulus onset, we computed the feature in the first 30-seconds after stimulus onset and divided by the value of the feature in the 30-seconds prior to stimulus onset. Thus, we report how much stimulus onset or offset

changed the value of the feature from its pre-switch baseline to reflect how the addition or removal of a stimulus affected neural activity.

All analyses of the temporal dynamics of neural activity was performed using Fourier transforms. We used MATLAB's periodogram to average the power of the four frequency bands used in our analyses (1st band: 0.07 – 0.2 Hz, 2nd band: 0.2 – 0.33 Hz, 3rd band: 0.33 – 0.47 Hz, 4th band: 0.47 – 0.6 Hz). We used MATLAB's spectrogram to determine the max, average, and standard deviation of the frequency with the most power in a 30-second bin, using 10-second long sliding windows with 50% overlap. Thus, our measures quantified how much a switch from buffer to stimulus or stimulus to buffer changed activity.

### 3.6.4 Determining functional connectivity

For each session, every neuron's activity was normalized by the peak value it reached in the entire 21-minute imaging session, bounding every neuron's activity in the range [0,1]. Each session generated an $n$ x $T$ matrix, where $n$ is the number of neurons and $T$ is the length in time of imaging. Using this matrix, we generated two adjacency matrices, one for the pre-switch period and one for the post-switch period. Each of these periods lasted 30 seconds and resulted in 28 periods of activity (each session had 7 pulses, 2 switches per pulse, and 2 pre- and post-switch periods per switch). We made two types of adjacency matrices for every block: one based on the absolute value of the Pearson's correlation (PC), and the other based on the normalized mutual information (NMI) with a 0.1 bin size. The former was calculated using MATLAB's built-in corr function. The latter was calculated per Strehl and Ghosh (2002) as: $\mathrm{NMI}(A,B) =$

$\frac{\mathrm{MI}(A,B)}{\sqrt{\mathrm{entropy}(A)\times\mathrm{entropy}(B)}}$, where entropy(A) is the entropy of the activity of neuron A, and MI(A,B) is the mutual information between the activity patterns of neurons A and B. While many variants of NMI exist (Kvålseth, 2017), the one we used has the desirable property of only reaching its maximum value when the distributions of states of two neurons are identical. If a neuron had an entropy of 0 because all its activity during the entire 30-second period was localized to one histogram bin (e.g., 0-0.1), then its edges to all other neurons were set to 0, effectively decoupling the neuron from the network; this only occurred for 7.3%, or 8,930 out of 123,116 cells across all imaging sessions and worms. We reasoned that a neuron whose activity did not appreciably change in a 30-second time period is not likely to be involved in processing of that stimulus. Finally, all self-loops were removed by setting the diagonal of the adjacency matrix to 0.

### 3.6.5 Graph-theoretic analysis

Graph-theoretic features were calculated using the Brain Connectivity Toolbox (Rubinov and Sporns, 2010; Rubinov and Sporns, 2011) on the largest connected component of each network. For features that produced distributions, such as local efficiency, we report the mean value. The degree distribution, radius, diameter, largest eigenvalue, and average shortest path, were all normalized by the number of neurons in the largest connected component. We used the Louvain community detection algorithm to find modules (Blondel et al., 2008).

### 3.6.6 Machine learning classification

The logistic regression classifier was built using one of three sets of features. The first set was composed of graph-theoretic features. The second set (called activity features) included the mean and standard deviation of neural activity. The third set of features combined the first and second sets. All graph-theoretic features used to classify stimulus valence and identity came from adjacency matrices constructed using NMI. A logistic regression classifier was trained on these three sets of features, and built using Python's scikit-learn library (Pedregosa et al., 2011), with default settings and using leave-one-out cross-validation to test generalization error. Finally, to avoid over-fitting, we used permutation testing (Test 1 in Ojala and Garriga, 2010) in which we randomly permutated the labels of the classes 1000 times and compared each classifier's performance to its own null distribution. We took the relative position of the classifier's true accuracy (trained on non-permutated labels) in this permutation distribution to be its p-value (Ojala and Garriga, 2010; Combrisson and Jerbi, 2015). This was a critical test that ensured our results were not merely due to chance, which is a significant yet often unappreciated issue in machine learning applications because theoretical chance is defined for sample sizes that are infinitely large (Combrisson and Jerbi, 2015).

### 3.6.7 Statistical analyses for mixed-effects models

Our experiments consisted of multiple measurements from the same animal, grouped according to three ecologically-relevant aspects of chemical stimuli. This repeated-measures design is often modeled using a mixed-effects model because it accounts for: 1) fixed-effects owed to the ecologically-relevant condition (e.g., valence),

and 2) random-effects due to animal variability (e.g., some animals might naturally have a larger modularity). Thus, we can provide a mixed-effects model with a matrix that contains information on the time in seconds since the first pulse, graph-theoretic features assessed at that pulse, and an indicator variable denoting which stimulus property the animal experienced (e.g., attractant or repellent). A mixed-effects model that better explains the data using the class indicator than without it, tested using a likelihood-ratio test, indicates a significant contribution from the fixed-effect to the model fit. We used linear mixed-effects models when the data were qualitatively normally distributed, as tested with a quantile-quantile plot using MATLAB's qqplot, or a generalized linear-mixed effects model with a response distribution modeled as a gamma distribution otherwise.

Chapter 3, in full, is a manuscript submitted for publication. Neural network features distinguish chemosensory stimuli in *Caenorhabditis elegans*. How, Javier J.; Navlakha, Saket; Chalasani, Sreekanth H, 2020. The dissertation author was the primary investigator and author of this paper.

### 3.7 References


Ressler KJ, Sullivan SL, Buck LB. A zonal organization of odorant receptor gene expression in the olfactory epithelium. Cell. 1993;73:597-609.

Kurtovic A, Widmer A, Dickson BJ. A single class of olfactory neurons mediates behavioural responses to a Drosophila sex pheromone. Nature. 2007;446(7135):542-6. Epub 2007/03/30. doi: 10.1038/nature05672. PubMed PMID: 17392786.

Hallem EA, Carlson JR. Coding of odors by a receptor repertoire. Cell. 2006;125(1):143-60. Epub 2006/04/18. doi: 10.1016/j.cell.2006.01.050. PubMed PMID: 16615896.

Ai M, Min S, Grosjean Y, Leblanc C, Bell R, Benton R, Suh GSB. Acid sensing by the Drosophila olfactory system. Nature. 2010;468(7324):691-5. Epub 2010/11/19. doi: 10.1038/nature09537. PubMed PMID: 21085119; PubMed Central PMCID: PMCPMC3105465.

Dweck HK, Ebrahim SA, Kromann S, Bown D, Hillbur Y, Sachse S, Hansson BS, Stensmyr MC. Olfactory preference for egg laying on citrus substrates in Drosophila. Curr Biol. 2013;23(24):2472-80. Epub 2013/12/10. doi: 10.1016/j.cub.2013.10.047. PubMed PMID: 24316206.

Stensmyr MC, Dweck HK, Farhan A, Ibba I, Strutz A, Mukunda L, Linz J, Grabe V, Steck K, Lavista-Llanos S, Wicher D, Sachse S, Knaden M, Becher PG, Seki Y, Hansson BS. A conserved dedicated olfactory circuit for detecting harmful microbes in Drosophila. Cell. 2012;151(6):1345-57. Epub 2012/12/12. doi: 10.1016/j.cell.2012.09.046. PubMed PMID: 23217715.

Leinwand SG, Chalasani SH. Olfactory networks: from sensation to perception. Curr Opin Genet Dev. 2011;21(6):806-11. Epub 2011/09/06. doi: S0959-437X(11)00118-3 [pii] 10.1016/j.gde.2011.07.006. PubMed PMID: 21889328.

Grabe V, Sachse S. Fundamental principles of the olfactory code. Biosystems. 2018;164:94-101. Epub 2017/10/22. doi: 10.1016/j.biosystems.2017.10.010. PubMed PMID: 29054468.

Smith DV, St John SJ. Neural coding of gustatory information. Curr Opin Neurobiol. 1999;9(4):427-35. Epub 1999/08/17. doi: 10.1016/S0959-4388(99)80064-6. PubMed PMID: 10448155.

de Brito Sanchez G, Giurfa M. A comparative analysis of neural taste processing in animals. Philos Trans R Soc Lond B Biol Sci. 2011;366(1574):2171-80. Epub 2011/06/22. doi: 10.1098/rstb.2010.0327. PubMed PMID: 21690133; PubMed Central PMCID: PMCPMC3130363.

Ohla K, Yoshida R, Roper SD, Di Lorenzo PM, Victor JD, Boughter JD, Fletcher M, Katz DB, Chaudhari N. Recognizing Taste: Coding Patterns Along the Neural Axis in Mammals. Chem Senses. 2019;44(4):237-47. Epub 2019/02/23. doi: 10.1093/chemse/bjz013. PubMed PMID: 30788507; PubMed Central PMCID: PMCPMC6462759.

White JG, Southgate E, Thomson JN, Brenner S. The structure of the nervous system of the nematode Caenorhabditis elegans. Philos Trans R Soc Lond B Biol Sci. 1986;314(1165):1-340. PubMed PMID: 22462104.

Cook SJ, Jarrell TA, Brittin CA, Wang Y, Bloniarz AE, Yakovlev MA, Nguyen KCQ, Tang LTH, Bayer EA, Duerr JS, Bülow HE, Hobert O, Hall DH, Emmons SW. Whole-animal connectomes of both Caenorhabditis elegans sexes. Nature. 2019;571(7763):63-71. Epub 2019/07/05. doi: 10.1038/s41586-019-1352-7. PubMed PMID: 31270481.

Jospin M, Jacquemond V, Mariol MC, Segalat L, Allard B. The L-type voltage-dependent Ca2+ channel EGL-19 controls body wall muscle function in Caenorhabditis elegans. J Cell Biol. 2002;159(2):337-48. PubMed PMID: 12391025.

Kerr R, Lev-Ram V, Baird G, Vincent P, Tsien RY, Schafer WR. Optical imaging of calcium transients in neurons and pharyngeal muscle of C. elegans. Neuron. 2000;26(3):583-94. PubMed PMID: 10896155.

Liu Q, Kidd PB, Dobosiewicz M, Bargmann CI. C. elegans AWA Olfactory Neurons Fire Calcium-Mediated All-or-None Action Potentials. Cell. 2018;175(1):57-70 e17. Epub 2018/09/18. doi: 10.1016/j.cell.2018.08.018. PubMed PMID: 30220455.

Leinwand SG, Chalasani SH. Neuropeptide signaling remodels chemosensory circuit composition in Caenorhabditis elegans. Nat Neurosci. 2013;16(10):1461-7. Epub 2013/09/10. doi: nn.3511 [pii] 10.1038/nn.3511. PubMed PMID: 24013594; PubMed Central PMCID: PMC3786745.

Leinwand SG, Yang CJ, Bazopoulou D, Chronis N, Srinivasan J, Chalasani SH. Circuit mechanisms encoding odors and driving aging-associated behavioral declines in Caenorhabditis elegans. eLife. 2015;4:e10181. doi: 10.7554/eLife.10181. PubMed PMID: 26394000; PubMed Central PMCID: PMC4577979.

Chronis N, Zimmer M, Bargmann CI. Microfluidics for in vivo imaging of neuronal and behavioral activity in Caenorhabditis elegans. Nat Methods. 2007;4(9):727-31. Epub 2007/08/21. doi: nmeth1075 [pii] 10.1038/nmeth1075. PubMed PMID: 17704783.

Chalasani SH, Chronis N, Tsunozaki M, Gray JM, Ramot D, Goodman MB, Bargmann CI. Dissecting a circuit for olfactory behaviour in Caenorhabditis elegans. Nature. 2007;450(7166):63-70. Epub 2007/11/02. doi: nature06292 [pii] 10.1038/nature06292. PubMed PMID: 17972877.

Schrodel T, Prevedel R, Aumayr K, Zimmer M, Vaziri A. Brain-wide 3D imaging of neuronal activity in Caenorhabditis elegans with sculpted light. Nat Methods. 2013;10(10):1013-20. Epub 2013/09/10. doi: nmeth.2637 [pii] 10.1038/nmeth.2637. PubMed PMID: 24013820.

Kato S, Kaplan HS, Schrodel T, Skora S, Lindsay TH, Yemini E, Lockery S, Zimmer M. Global brain dynamics embed the motor command sequence of Caenorhabditis elegans. Cell. 2015;163(3):656-69. Epub 2015/10/20. doi: 10.1016/j.cell.2015.09.034. PubMed PMID: 26478179.

Nichols ALA, Eichler T, Latham R, Zimmer M. A global brain state underlies C. elegans sleep behavior. Science. 2017;356(6344). Epub 2017/06/24. doi: 10.1126/science.aam6851. PubMed PMID: 28642382.

Grabe V, Baschwitz A, Dweck HKM, Lavista-Llanos S, Hansson BS, Sachse S. Elucidating the Neuronal Architecture of Olfactory Glomeruli in the Drosophila Antennal Lobe. Cell reports. 2016;16(12):3401-13. Epub 2016/09/23. doi: 10.1016/j.celrep.2016.08.063. PubMed PMID: 27653699.

Skora S, Mende F, Zimmer M. Energy Scarcity Promotes a Brain-wide Sleep State Modulated by Insulin Signaling in C. elegans. Cell reports. 2018;22(4):953-66. Epub 2018/02/02. doi: 10.1016/j.celrep.2017.12.091. PubMed PMID: 29386137; PubMed Central PMCID: PMCPMC5846868.

Scholz M, Linder AN, Randi F, Sharma AK, Yu X, Shaevitz JW, Leifer A. Predicting natural behavior from whole-brain neural dynamics. bioRxiv. 2018:445643.

Müller B, Reinhardt J, Strickland MT. Neural networks: an introduction: Springer Science & Business Media; 2012.

Easley D, Kleinberg J. Networks, crowds, and markets: Cambridge university press Cambridge; 2010.

Barabási A-L. Network science: Cambridge university press; 2016.

Albrecht DR, Bargmann CI. High-content behavioral analysis of Caenorhabditis elegans in precise spatiotemporal chemical environments. Nat Methods. 2011;8(7):599-605. Epub 2011/06/15. doi: nmeth.1630 [pii] 10.1038/nmeth.1630. PubMed PMID: 21666667; PubMed Central PMCID: PMC3152576.

Bargmann CI, Hartwieg E, Horvitz HR. Odorant-selective genes and neurons mediate olfaction in C. elegans. Cell. 1993;74(3):515-27. PubMed PMID: 8348618.

Chatzigeorgiou M, Bang S, Hwang SW, Schafer WR. tmc-1 encodes a sodium-sensitive channel required for salt chemosensation in C. elegans. Nature. 2013;494(7435):95-9. Epub 2013/02/01. doi: 10.1038/nature11845. PubMed PMID: 23364694; PubMed Central PMCID: PMCPMC4021456.

Chalasani SH, Kato S, Albrecht DR, Nakagawa T, Abbott LF, Bargmann CI. Neuropeptide feedback modifies odor-evoked dynamics in Caenorhabditis elegans olfactory neurons. Nat Neurosci. 2010;13(5):615-21. Epub 2010/04/07. doi: nn.2526 [pii] 10.1038/nn.2526. PubMed PMID: 20364145; PubMed Central PMCID: PMC2937567.

Rubinov M, Sporns O. Complex network measures of brain connectivity: uses and interpretations. Neuroimage. 2010;52(3):1059-69. Epub 2009/10/13. doi: 10.1016/j.neuroimage.2009.10.003. PubMed PMID: 19819337.

Yang W, Chakrabarti D, Chenxi W, Faloutsos C, editors. Epidemic spreading in real networks: an eigenvalue viewpoint. 22nd International Symposium on Reliable Distributed Systems, 2003 Proceedings; 2003 6-8 Oct. 2003.

Bassett DS, Sporns O. Network neuroscience. Nat Neurosci. 2017;20(3):353-64. Epub 2017/02/24. doi: 10.1038/nn.4502. PubMed PMID: 28230844; PubMed Central PMCID: PMCPMC5485642.

Strehl A, Ghosh J. Cluster ensembles---a knowledge reuse framework for combining multiple partitions. Journal of machine learning research. 2002;3(Dec):583-617.

Hilliard MA, Bargmann CI, Bazzicalupo P. C. elegans responds to chemical repellents by integrating sensory inputs from the head and the tail. Curr Biol. 2002;12(9):730-4. PubMed PMID: 12007416.

Bassett DS, Wymbs NF, Porter MA, Mucha PJ, Carlson JM, Grafton ST. Dynamic reconfiguration of human brain networks during learning. Proceedings of the National Academy of Sciences. 2011;108(18):7641. doi: 10.1073/pnas.1018985108.

Tian L, Hires SA, Mao T, Huber D, Chiappe ME, Chalasani SH, Petreanu L, Akerboom J, McKinney SA, Schreiter ER, Bargmann CI, Jayaraman V, Svoboda K, Looger LL. Imaging neural activity in worms, flies and mice with improved GCaMP calcium indicators. Nat Methods. 2009;6(12):875-81. PubMed PMID: 19898485.

Akerboom J, Chen TW, Wardill TJ, Tian L, Marvin JS, Mutlu S, Calderon NC, Esposti F, Borghuis BG, Sun XR, Gordus A, Orger MB, Portugues R, Engert F, Macklin JJ, Filosa A, Aggarwal A, Kerr RA, Takagi R, Kracun S, Shigetomi E, Khakh BS, Baier H, Lagnado L, Wang SS-H, Bargmann CI, Kimmel BE, Jayaraman V, Svoboda K, Kim DS, Schreiter DS, Looger LL. Optimization of a GCaMP calcium indicator for neural activity imaging. J Neurosci. 2012;32(40):13819-40. doi: 10.1523/JNEUROSCI.2601-12.2012. PubMed PMID: 23035093; PubMed Central PMCID: PMC3482105.

van Wijk BC, Stam CJ, Daffertshofer A. Comparing brain networks of different size and connectivity density using graph theory. PLoS One. 2010;5(10):e13701. Epub 2010/11/10. doi: 10.1371/journal.pone.0013701. PubMed PMID: 21060892; PubMed Central PMCID: PMCPMC2965659.

Watts DJ, Strogatz SH. Collective dynamics of 'small-world' networks. Nature. 1998;393(6684):440-2. Epub 1998/06/12. doi: 10.1038/30918. PubMed PMID: 9623998.

Kohn A, Smith MA. Stimulus dependence of neuronal correlation in primary visual cortex of the macaque. Journal of Neuroscience. 2005;25(14):3661-73.

Eggermont JJ. Correlated neural activity as the driving force for functional changes in auditory cortex. Hearing research. 2007;229(1-2):69-80.

Aertsen A, Gerstein G, Habib M, Palm G. Dynamics of neuronal firing correlation: modulation of" effective connectivity". Journal of neurophysiology. 1989;61(5):900-17.

Sheikhattar A, Miran S, Liu J, Fritz JB, Shamma SA, Kanold PO, Babadi B. Extracting neuronal functional network dynamics via adaptive Granger causality analysis. Proc Natl Acad Sci U S A. 2018;115(17):E3869-E78. Epub 2018/04/11. doi:

10.1073/pnas.1718154115. PubMed PMID: 29632213; PubMed Central PMCID: PMCPMC5924897.

Feizi S, Marbach D, Medard M, Kellis M. Network deconvolution as a general method to distinguish direct dependencies in networks. Nat Biotechnol. 2013;31(8):726-33. Epub 2013/07/16. doi: 10.1038/nbt.2635. PubMed PMID: 23851448; PubMed Central PMCID: PMCPMC3773370.

Sefer E, Kingsford C, editors. Convex risk minimization to infer networks from probabilistic diffusion data at multiple scales. 2015 IEEE 31st International Conference on Data Engineering; 2015: IEEE.

Sugihara G, May R, Ye H, Hsieh CH, Deyle E, Fogarty M, Munch S. Detecting causality in complex ecosystems. Science. 2012;338(6106):496-500. Epub 2012/09/22. doi: 10.1126/science.1227079. PubMed PMID: 22997134.

Ha H, Hendricks M, Shen Y, Gabel CV, Fang-Yen C, Qin Y, Colon-Ramos D, Shen K, Samuel ADT, Zhang Y. Functional organization of a neural network for aversive olfactory learning in Caenorhabditis elegans. Neuron. 2010;68(6):1173-86. Epub 2010/12/22. doi: S0896-6273(10)00941-4 [pii] 10.1016/j.neuron.2010.11.025. PubMed PMID: 21172617; PubMed Central PMCID: PMC3038580.

Rubinov M, Sporns O. Weight-conserving characterization of complex functional brain networks. Neuroimage. 2011;56(4):2068-79. Epub 2011/04/05. doi: 10.1016/j.neuroimage.2011.03.069. PubMed PMID: 21459148.

van den Heuvel MP, de Lange SC, Zalesky A, Seguin C, Yeo BTT, Schmidt R. Proportional thresholding in resting-state fMRI functional connectivity networks and consequences for patient-control connectome studies: Issues and recommendations. Neuroimage. 2017;152:437-49. Epub 2017/02/09. doi: 10.1016/j.neuroimage.2017.02.005. PubMed PMID: 28167349.

Larsch J, Flavell SW, Liu Q, Gordus A, Albrecht DR, Bargmann CI. A Circuit for Gradient Climbing in C. elegans Chemotaxis. Cell reports. 2015;12(11):1748-60. doi: 10.1016/j.celrep.2015.08.032. PubMed PMID: 26365196.

Hale LA, Lee ES, Pantazis AK, Chronis N, Chalasani SH. Altered Sensory Code Drives Juvenile-to-Adult Behavioral Maturation in Caenorhabditis elegans. eNeuro. 2016;3(6). doi: 10.1523/ENEURO.0175-16.2016. PubMed PMID: 28083560; PubMed Central PMCID: PMCPMC5220224.

Yoshida K, Hirotsu T, Tagawa T, Oda S, Wakabayashi T, Iino Y, Takeshi I. Odour concentration-dependent olfactory preference change in C. elegans. Nature communications. 2012;3:739. Epub 2012/03/15. doi: 10.1038/ncomms1750. PubMed PMID: 22415830.

Wang X, Li G, Liu J, Liu J, Xu XZ. TMC-1 Mediates Alkaline Sensation in C. elegans through Nociceptive Neurons. Neuron. 2016;91(1):146-54. Epub 2016/06/21. doi:

10.1016/j.neuron.2016.05.023. PubMed PMID: 27321925; PubMed Central PMCID: PMCPMC4938749.

Pnevmatikakis EA, Merel J, Pakman A, Paninski L, editors. Bayesian spike inference from calcium imaging data. 2013 Asilomar Conference on Signals, Systems and Computers; 2013: IEEE.

Pnevmatikakis EA, Gao Y, Soudry D, Pfau D, Lacefield C, Poskanzer K, Bruno R, Yuste R, Paninski L. A structured matrix factorization framework for large scale calcium imaging data analysis. arXiv preprint arXiv:14092903. 2014.

Friedrich J, Paninski L, editors. Fast active set methods for online spike inference from calcium imaging. Advances In Neural Information Processing Systems; 2016.

Pnevmatikakis EA, Soudry D, Gao Y, Machado TA, Merel J, Pfau D, Reardon T, Mu Y, Lacefield C, Yang W, Ahrens M, Bruno R, Jessell TM, Peterka DS, Yuste R, Paninski L. Simultaneous Denoising, Deconvolution, and Demixing of Calcium Imaging Data. Neuron. 2016;89(2):285-99. Epub 2016/01/18. doi: 10.1016/j.neuron.2015.11.037. PubMed PMID: 26774160; PubMed Central PMCID: PMCPMC4881387.

Pnevmatikakis EA, Giovannucci A. NoRMCorre: An online algorithm for piecewise rigid motion correction of calcium imaging data. J Neurosci Methods. 2017;291:83-94. Epub 2017/08/08. doi: 10.1016/j.jneumeth.2017.07.031. PubMed PMID: 28782629.

Giovannucci A, Friedrich J, Gunn P, Kalfon J, Brown BL, Koay SA, Taxidis J, Najafi F, Gauthier JL, Zhou P, Khakh BS, Tank DW, Chklovskii DB, Pnevmatikakis EA. CaImAn an open source tool for scalable calcium imaging data analysis. eLife. 2019;8. Epub 2019/01/18. doi: 10.7554/eLife.38173. PubMed PMID: 30652683; PubMed Central PMCID: PMCPMC6342523.

Kvålseth T. On normalized mutual information: measure derivations and properties. Entropy. 2017;19(11):631.

Blondel VD, Guillaume J-L, Lambiotte R, Lefebvre E. Fast unfolding of communities in large networks. Journal of Statistical Mechanics: Theory and Experiment. 2008;2008(10):P10008. doi: 10.1088/1742-5468/2008/10/p10008.

Pedregosa F, Varoquaux G, Gramfort A, Michel V, Thirion B, Grisel O, Blondel M, Prettenhofer P, Weiss R, Dubourg V, Vanderplas J, Passos A, Cournapeau D, Brucher M, Perrot M, Duchesnay E. Scikit-learn: Machine learning in Python. Journal of machine learning research. 2011;12(Oct):2825-30.

Ojala M, Garriga GC. Permutation tests for studying classifier performance. Journal of Machine Learning Research. 2010;11(Jun):1833-63.

Combrisson E, Jerbi K. Exceeding chance level by chance: The caveat of theoretical chance levels in brain signal classification and statistical assessment of decoding accuracy. J Neurosci Methods. 2015;250:126-36. Epub 2015/01/18. doi: 10.1016/j.jneumeth.2015.01.010. PubMed PMID: 25596422.

## 4. Conclusions

Altogether, I have described organizational principles of the *C. elegans* nervous system's structural and functional connectivity that may play a role in processing information about the environment.

I first studied the structural connectivity of the *C. elegans* nervous system, and of several other complex networks, in Chapter 2. I discovered that these networks all demonstrate a power-law relationship between the number of nodes in a module and the number of edges crossing between modules. This property, called Rentian scaling, was unique to information processing networks, and not found in other types of networks (e.g. social networks). Importantly, this property was evident when I used evolutionarily-defined 'functional' modules, or groups of nodes with a similar function, which suggests that evolution converged on Rentian scaling for different types of biological networks, similar to how the human design process did for integrated circuits. This indicates that information processing networks negotiate a trade-off between the efficiency of information transfer and the cost of maintaining structural connections. The *C. elegans* nervous system, in particular, seems to prioritize computational power over cost by integrating information over functionally distinct neurons.

I next inferred and characterized the functional connectivity of the *C. elegans* 'brain' in Chapter 3. I found that chemical stimuli elicit stimulus-specific patterns of activity on stimulus onset and offset, but that simpler features of population activity are not as consistently modulated. Additionally, these graph-theoretic features help classify which chemical an animal is experiencing. This suggests that graph theory may be a useful theoretical framework in the study of large-scale neural activity. For one, it does not

depend on the ability to consistently identify neurons across individuals, which is not likely to be tractable in other species with many more neurons. Furthermore, compared to dimensionality reduction techniques, I argue that graph theory, by focusing on cellular interactions, better captures biologically plausible mechanisms of information processing in neural networks. Finally, this approach revealed stimulus-specific neural network features that could be tested with targeted, cell-specific analyses to identify their biological underpinnings.

### 4.1 Origins and interpretation of Rentian scaling

While I found that the molecular networks of several species and cell types exhibit Rentian scaling, it has only been tested in a few biological neural networks (Bassett et al., 2010). Because neural networks must also negotiate a trade-off between cost and efficiency, I propose that neural networks in other species are also likely to demonstrate Rentian scaling. Indeed, a recent study found that the central brain of adult *Drosophila melanogaster* is also Rentian (Scheffer et al., 2020). Modern efforts to determine the structural connectivity of the mouse and larval zebrafish brains will allow us to test for the generality of Rentian scaling in neural networks across the animal kingdom (Oh et al., 2014; Hildebrand et al., 2017).

Because Rentian scaling is found in different types of networks, it is unclear which generative mechanisms can give rise to it, and how these mechanisms control the value of the Rent's exponent. I posit that Rentian scaling is limited to resource-constrained networks, and is likely to emerge via distinct mechanisms. For instance, both protein-protein interaction networks (PPIs) and the London Underground have limited resources and exhibit Rentian scaling. Nonetheless, the biologically-inspired generative mechanism

I proposed in Chapter 2 for PPIs is not likely to be relevant for the formation of the London Underground. On the other hand, three social and technological networks I studied, which do not necessarily incur costs in maintaining connections, were not Rentian. Arguably, the network of scientific collaborations I considered in Chapter 2 does process information and does incur costs, but is perhaps not optimized by a central coordinator, as in the case of electronic circuits which demonstrate Rentian scaling, or refined over millennia, as biological networks often are; hence, it would not be Rentian because it has not been fine-tuned. Future work should explain why some mechanisms, but not others, produce networks with Rentian scaling. It would also be interesting to understand if some mechanisms do not at first produce Rentian networks but, if refined over time, can lead to Rentian scaling (as in the case of the London Underground).

Developmental programs seem to refine the precise value of the Rent's exponent. I showed, in Chapter 2, that regulatory networks in embryonic stem cells have a smaller Rent's exponent than differentiated cell lines. Therefore, I hypothesize that mature networks will typically have larger Rent's exponent than their undeveloped counterparts. To test this, one could measure the Rent's exponent of the *C. elegans* nervous system in different larval stages, and contrast these with the exponent measured for a young adult in Chapter 2. Additionally, one could compute the Rent's exponent of human children, teens, and adults, and see how this trade-off between cost and efficiency is renegotiated across time. It is important to note that the numbers of neurons and synapses changes over time in nervous systems (Urbán and Guillemot, 2014; Navlakha et al., 2015). Hence, I propose that, like regulatory networks, these added edges will be preferably laid

between functional modules, thereby increasing the Rent's exponent across developmental time.

A network's Rent's exponent describes a trade-off between the cost of wiring and efficiency of information transmission and integration in a network. Hence, a network with a larger Rent's exponent should be more computationally powerful. One way to test this hypothesis would be to measure the Rent's exponents of structural or functional brain networks of several human individuals, and correlate their Rent's exponent with conventional intelligence measurements; an important caveat is that intelligence is difficult to assess. One may also expect that Rent's exponents are sensitive to diseased states, which could provide new insight into the physiological processes that go awry. For instance, a lower Rent's exponent in some disease, compared to healthy individuals, may suggest that long-range, intermodule connections are disproportionally lesioned, thereby impairing the ability of the nervous system to integrate information across the brain. Altogether, these studies would clarify the functional significance of the precise value of the Rent's exponent.

### 4.2 Towards a neural graph theory

Graph theory has helped characterize the local and global organization of diverse social, informational, technological, and biological networks (Newman, 2010). It has allowed scientists to find striking similarities, and dissimilarities, between many natural and artificial networks, suggesting that there may be fundamental design constraints and organizational principles shared by certain types of systems. On the other hand, these properties may simply be evolutionary spandrels, or byproducts, of other design principles

shared by all of these networks (Rubinov, 2016). Furthermore, while some graph-theoretic properties are believed to play certain roles in the transmission of information throughout a network, their applicability to real neural networks is currently unclear. For instance, the characteristic path length is the average of the shortest paths linking any two neurons; hence, the lower this value, the more easily any two neurons are believed to communicate. A low characteristic path length implies that the network efficiently transmits information, and is a hallmark of small-world networks. Nevertheless, there is no reason to believe that two neurons will, need, or should communicate via the shortest path that links them. Moreover, it is unclear how individual neurons would even discover the shortest path in the absence of some central coordinator with knowledge of the entire brain's topology (Sporns, 2018). Graph theory should incorporate domain-specific knowledge to become a more powerful framework for the study of real neural networks.

There are many aspects of neural network function that would help us develop a more neuroscience-oriented graph theory. Future work should focus on the role of non-neuronal cells (Mu et al., 2019), build data-constrained network models (Naumann et al., 2016; Williamson et al., 2019), study the temporal evolution of neuronal interactions and coordination of different forms of neuronal communication (e.g. chemical, electrical, neuromodulatory, excitatory, inhibitory) using multilayer and multiplex networks (see reviews by Kivela et al., 2014, and Aleta and Moreno, 2019), develop theories to relate network structure and function (see review by Curto and Morrison, 2019), potentially by studying control theory (Liu et al., 2011; Gu et al., 2015; Yan et al., 2017), and finally relate all of these in behaving animals (Venkatachalam et al., 2016; Nguyen et al., 2016; Nguyen et al., 2017; Scholz et al., 2018; Kim et al., 2017; Cong et al., 2017; Symvoulidis

et al., 2017). In the end, these efforts would help us model the biological instantiation of computational algorithms in the brains of animals, and mechanistically understand how cells in the brain produce complex, perhaps even cognitive, behaviors. We could then predict how an animal will respond to an arbitrary stimulus – from activity in the sensory periphery to behavior. The ability to describe and predict how neural activity gives rise to behavior would constitute a thorough understanding of the brain.

Non-neuronal cells, such as astrocytes, are known to influence neuronal communication and network function (see review by Allen, 2014). Hermaphroditic *C. elegans* have 56 glia, some of which are astrocyte-like, which seem to interact with neurons in an evolutionarily-conserved manner (see review by Singhvi and Shaham, 2019), and the failure to record their activity and interactions with neurons provides an incomplete picture of the relevant elements in neural networks. Therefore, it will be important to simultaneously record from both neurons and glia, as has been recently done in larval zebrafish (Mu et al., 2019). The incorporation of different node types, such as neurons and glial cells, into our graph-theoretic framework may require the development of bipartite graphs, or two graphs of different types of nodes (e.g. neurons and astrocytes), where there is a connection between pairs of nodes in different graphs if they interact (e.g. neurons in one graph are connected to astrocytes in the other graph that regulate their input or output). Projecting these graphs onto a single graph might describe neurons that are connected if they are regulated by the same astrocytes, or astrocytes that are connected if they regulate the same neurons (Newman, 2010), and thus reveal organizational patterns from two perspectives.

Data-constrained circuit models have been used to predict how functionally distinct neurons may be connected to produce behavior, yet may yield multiple topologies that can quantitatively recapitulate observed neural activity and animal behavior (e.g. Naumann et al., 2016). This ambiguity may be partly due to the use of fairly simple stimuli and behavioral outputs to study a high-dimensional system (i.e. the nervous system of any organism; Gao and Ganguli, 2015). One approach to address this problem may be to use artificial neural networks to drive network activity to unexplored states, which could be assessed using dimensionality reduction techniques (e.g. Bashivan et al., 2019). Alternatively, natural stimuli may drive the nervous system to exist in ecologically-relevant states, which should provide a clearer idea of how the nervous system was evolutionarily 'meant' to function, as opposed to how it 'could' function by using artificial stimuli (Jazayeri and Afraz, 2017; Krakauer et al., 2017). In any case, a data-constrained network model could mechanistically relate ongoing neuronal dynamics and structural connectivity to network activity.

The highly recurrent nature of the brain ensures that feedback circuitry is important to animal behavior. Neuropeptide feedback in *C. elegans*, for instance, regulates turning during olfactory behaviors (Chalasani et al., 2010) and salt chemotaxis learning (Tomioka et al., 2006). Neurons can, at the very least, communicate via neurotransmitters, neuropeptides, neuromodulators, and gap junctions, and these forms of communication can affect neurons over different timescales. Multilayer and multiplex networks can model these types of interactions to extract novel insight (see reviews by Kivela et al., 2014, Aleta and Moreno, 2019), but are still fairly immature. Furthermore, current GCaMP indicators and microscopes may be too slow to precisely model how interactions between

neurons change across time. Hence, future efforts should focus on developing fluorescent neurotransmitter-specific and voltage indicators (reviewed by Lin and Schnitzer, 2016), and microscopes with faster acquisition rates (reviewed by Weisenburger and Vaziri, 2018).

The notion that 'form follows function' dictates that the structure of some object is due, at least partly, to its function. While some have found that even a small network's topology does not accurately predict its function (e.g. Guet et al., 2002), others have noted that there is a substantial correspondence between structural and functional connectivity (e.g. van den Heuvel et al., 2009a; see review by Honey et al., 2010). Consistently, some groups have found that control theory can be used to predict how to drive networks to desired states by modulating selected nodes (see reviews by Liu and Barabási, 2016; Lynn and Bassett, 2019), and have used it to predict novel locomotory roles for neurons in *C. elegans* (Yan et al., 2017). In any case, a theory that makes predictions about how structure will impact function must be experimentally tested. For instance, if a theory proposes that connections between certain neurons would lead to aberrant synchronization across the nervous system and, perhaps, epileptic symptoms, then experimentally adding these connections would be a strong test (Hawk and Colón-Ramos, 2020). If our graph-theoretic analysis suggests that certain neurons are on the shortest paths between many neurons, and thus are central to the network (i.e. have high betweenness centrality), then optogenetically modulating their activity could help us test if neurons really need to communicate via the shortest path. By simultaneously measuring behavior, quantified using recent advances in computer vision (reviewed by Datta et al.,

2019), we will be able to understand how large-scale nervous system structure and function give rise to behavior.

Finally, there are fundamental limitations in using *C. elegans* as a model organism. For one, the functional roles of its neurons are not clearly delineated; for instance, some sensory neurons are involved in multiple sensory modalities (e.g., Kuhara et al., 2008; Biron et al., 2008; Leinwand and Chalasani, 2013), whereas those in other, commonly-studied species in neuroscience can be functionally limited. Moreover, neurons in *C. elegans* typically do not have an all-or-nothing action potential like those seen in other species; rather, they mostly use graded or plateau potentials (Mellem et al., 2008; Liu et al., 2018). Finally, its 302-neuron nervous system in orders of magnitude smaller than that of many other commonly studied model organisms, and its behavioral repertoire may also be relatively limited (Stephens et al., 2008). As a result, it is unclear if and how much the results described in Chapter 3 extend to other model organisms, but future efforts should assess the generality of our approach. Studying whole-brain activity in larval zebrafish, with ~100,000 neurons that use action potentials, would be a natural extension to this work (Ahrens et al., 2012).

In the end, interactions-based mechanistic approaches, alongside many others, will need to be integrated to answer how purely physical processes give rise to emergent phenomena, such as cognition. If one proceeds from the premise that ongoing activity in the nervous system, not the mere polarizations one observes in single neurons, but the large-scale patterns of activity and interactions between all relevant cells (e.g. neurons, interneurons, glia), is the physical and observable substrate of fairly abstract, and perhaps ill-defined, cognitive phenomena, then these aforementioned questions partly answer

why some, but not other, patterns of activity emerge, and how they contribute to cognition and behavior. It will be crucial to relate these mechanisms to behavior, measured in tasks designed to pinpoint subtle aspects of cognition (Bayne et al., 2019), which may be more feasible in species other than *C. elegans*.

### 4.3 References


Ahrens MB, Li JM, Orger MB, Robson DN, Schier AF, Engert F, Portugues R. (2012). Brain-wide neuronal dynamics during motor adaptation in zebrafish. *Nature*. https://doi.org/10.1038/nature11057

Aleta A, Moreno Y. (2019). Multilayer Networks in a Nutshell. *Annual Review of Condensed Matter Physics*. https://doi.org/10.1146/annurev-conmatphys-031218-013259

Allen NJ. (2014). Astrocyte Regulation of Synaptic Behavior. *Annual Review of Cell and Developmental Biology*. https://doi.org/10.1146/annurev-cellbio-100913-013053

Bashivan P, Kar K, DiCarlo JJ. (2019). Neural population control via deep image synthesis. *Science*. https://doi.org/10.1126/science.aav9436

Bassett DS, Greenfield DL, Meyer-Lindenberg A, Weinberger DR, Moore SW, Bullmore ET. (2010). Efficient physical embedding of topologically complex information processing networks in brains and computer circuits. *PLoS Computational Biology*, *6*(4). https://doi.org/10.1371/journal.pcbi.1000748

Bayne T, Brainard D, Byrne RW, Chittka L, Clayton N, Heyes C, Mather J, Ölveczky B, Shadlen M, Suddendorf T, Webb B. (2019). What is cognition? In *Current Biology*. https://doi.org/10.1016/j.cub.2019.05.044

Biron D, Wasserman S, Thomas JH, Samuel ADT, Sengupta P. (2008). An olfactory neuron responds stochastically to temperature and modulates Caenorhabditis elegans thermotactic behavior. *Proceedings of the National Academy of Sciences of the United States of America*. https://doi.org/10.1073/pnas.0805004105

Chalasani SH, Kato S, Albrecht DR, Nakagawa T, Abbott LF, Bargmann CI. (2010). Neuropeptide feedback modifies odor-evoked dynamics in Caenorhabditis elegans olfactory neurons. *Nature Neuroscience*. https://doi.org/10.1038/nn.2526

Cong L, Wang Z, Chai Y, Hang W, Shang C, Yang W, Bai L, Du J, Wang K, Wen Q. (2017). Rapid whole brain imaging of neural activity in freely behaving larval zebrafish (Danio rerio). *ELife*. https://doi.org/10.7554/eLife.28158

Curto C, Morrison K. (2019). Relating network connectivity to dynamics: opportunities and challenges for theoretical neuroscience. In *Current Opinion in Neurobiology*. https://doi.org/10.1016/j.conb.2019.06.003

Datta SR, Anderson DJ, Branson K, Perona P, Leifer A. (2019). Computational Neuroethology: A Call to Action. In *Neuron* (Vol. 104, Issue 1, pp. 11–24). https://doi.org/10.1016/j.neuron.2019.09.038

Gao P, Ganguli S. (2015). On simplicity and complexity in the brave new world of large-scale neuroscience. In *Current Opinion in Neurobiology*. https://doi.org/10.1016/j.conb.2015.04.003

Gu S, Pasqualetti F, Cieslak M, Telesford QK, Yu AB, Kahn AE, Medaglia JD, Vettel JM, Miller MB, Grafton ST, Bassett DS. (2015). Controllability of structural brain networks. *Nature Communications*. https://doi.org/10.1038/ncomms9414

Guet CC, Elowitz MB, Hsing W, Leibler S. (2002). Combinatorial synthesis of genetic networks. *Science*. https://doi.org/10.1126/science.1067407

Hawk JD. (2020). HySyn : A genetically-encoded synthetic synapse to rewire neural circuits in vivo. *BioRxiv*. https://doi.org/10.1101/2020.01.27.922203

Hildebrand DGC, Cicconet M, Torres RM, Choi W, Quan TM, Moon J, Wetzel AW, Scott Champion A, Graham BJ, Randlett O, Plummer GS, Portugues R, Bianco IH, Saalfeld S, Baden AD, Lillaney K, Burns R, Vogelstein JT, Schier AF, Lee WCA, Jeong WK, Lichtman JW, Engert F. (2017). Whole-brain serial-section electron microscopy in larval zebrafish. *Nature*. https://doi.org/10.1038/nature22356

Honey CJ, Thivierge JP, Sporns O. (2010). Can structure predict function in the human brain? In *NeuroImage*. https://doi.org/10.1016/j.neuroimage.2010.01.071

Jazayeri M, Afraz A. (2017). Navigating the Neural Space in Search of the Neural Code. In *Neuron*. https://doi.org/10.1016/j.neuron.2017.02.019

Kim DH, Kim J, Marques JC, Grama A, Hildebrand DGC, Gu W, Li JM, Robson DN. (2017). Pan-neuronal calcium imaging with cellular resolution in freely swimming zebrafish. *Nature Methods*. https://doi.org/10.1038/nmeth.4429

Kivelä M, Arenas A, Barthelemy M, Gleeson JP, Moreno Y, Porter MA. (2014). Multilayer networks. *Journal of Complex Networks*. https://doi.org/10.1093/comnet/cnu016

Krakauer JW, Ghazanfar AA, Gomez-Marin A, MacIver MA, Poeppel D. (2017). Neuroscience Needs Behavior: Correcting a Reductionist Bias. In *Neuron*. https://doi.org/10.1016/j.neuron.2016.12.041

Kuhara A, Okumura M, Kimata T, Tanizawa Y, Takano R, Kimura KD, Inada H, Matsumoto K, Mori I. (2008). Temperature sensing by an olfactory neuron in a circuit controlling behavior of C. elegans. *Science*. https://doi.org/10.1126/science.1148922

Lin MZ, Schnitzer MJ. (2016). Genetically encoded indicators of neuronal activity. In *Nature Neuroscience*. https://doi.org/10.1038/nn.4359

Liu YY, Barabási AL. (2016). Control principles of complex systems. *Reviews of Modern Physics*. https://doi.org/10.1103/RevModPhys.88.035006

Liu YY, Slotine JJ, Barabási AL. (2011). Controllability of complex networks. *Nature*. https://doi.org/10.1038/nature10011

Lynn CW, Bassett DS. (2019). The physics of brain network structure, function and control. *Nature Reviews Physics*. https://doi.org/10.1038/s42254-019-0040-8

Mellem JE, Brockie PJ, Madsen DM, Maricq A V. (2008). Action potentials contribute to neuronal signaling in C. elegans. *Nature Neuroscience*. https://doi.org/10.1038/nn.2131

Mu Y, Bennett D V., Rubinov M, Narayan S, Yang CT, Tanimoto M, Mensh BD, Looger LL, Ahrens MB. (2019). Glia Accumulate Evidence that Actions Are Futile and Suppress Unsuccessful Behavior. *Cell*. https://doi.org/10.1016/j.cell.2019.05.050

Naumann EA, Fitzgerald JE, Dunn TW, Rihel J, Sompolinsky H, Engert F. (2016). From Whole-Brain Data to Functional Circuit Models: The Zebrafish Optomotor Response. *Cell*. https://doi.org/10.1016/j.cell.2016.10.019

Navlakha S, Barth AL, Bar-Joseph Z. (2015). Decreasing-Rate Pruning Optimizes the Construction of Efficient and Robust Distributed Networks. *PLoS Computational Biology*. https://doi.org/10.1371/journal.pcbi.1004347

Newman M. (2010). Networks: An Introduction. In *Networks: An Introduction*. https://doi.org/10.1093/acprof:oso/9780199206650.001.0001

Nguyen JP, Linder AN, Plummer GS, Shaevitz JW, Leifer AM. (2017). Automatically tracking neurons in a moving and deforming brain. *PLoS Computational Biology*. https://doi.org/10.1371/journal.pcbi.1005517

Nguyen JP, Shipley FB, Linder AN, Plummer GS, Liu M, Setru SU, Shaevitz JW, Leifer AM. (2016). Whole-brain calcium imaging with cellular resolution in freely behaving Caenorhabditis elegans. *Proceedings of the National Academy of Sciences of the United States of America*. https://doi.org/10.1073/pnas.1507110112

Oh SW, Harris JA, Ng L, Winslow B, Cain N, Mihalas S, Wang Q, Lau C, Kuan L, Henry AM, Mortrud MT, Ouellette B, Nguyen TN, Sorensen SA, Slaughterbeck CR, Wakeman W, Li Y, Feng D, Ho A, Nicholas E, Hirokawa KE, Bohn P, Joines KM, Peng H, Hawrylycz MJ, Phillips JW, Hohmann JG, Wohnoutka P, Gerfen CR, Koch C, Bernard A, Dang C, Jones AR, Zeng H. (2014). A mesoscale connectome of the mouse brain. *Nature*. https://doi.org/10.1038/nature13186

Rubinov M. (2016). Constraints and spandrels of interareal connectomes. *Nature Communications*. https://doi.org/10.1038/ncomms13812

Scheffer LK, Xu CS, Januszewski M, Lu Z, Takemura S, Hayworth KJ, Huang GB, Shinomiya K, Maitin-Shepard J, Berg S, Clements J, Hubbard P, Katz W, Umayam L, Zhao T, Ackerman D, Blakely T, Bogovic J, Dolafi T, Kainmueller D, Kawase T, Khairy KA, Leavitt L, Li PH, Lindsey L, Neubarth N, Olbris DJ, Otsuna H, Trautman ET, Ito M, Goldammer J, Wolff T, Svirskas R, Schlegel P, Neace ER, Knecht CJ, Alvarado CX, Bailey DA, Ballinger S, Borycz JA, Canino BS, Cheatham N, Cook M, Dreher M, Duclos O, Eubanks B, Fairbanks K, Finley S, Forknall N, Francis A, Hopkins GP, Joyce EM, Kim S, Kirk NA, Kovalyak J, Lauchie SA, Lohff A, Maldonado C, Manley EA, McLin S, Mooney C, Ndama M, Ogundeyi O, Okeoma N, Ordish C, Padilla N, Patrick C, Paterson T, Phillips EE,

Phillips EM, Rampally N, Ribeiro C, Robertson MK, Rymer JT, Ryan SM, Sammons M, Scott AK, Scott AL, Shinomiya A, Smith C, Smith K, Smith NL, Sobeski MA, Suleiman A, Swift J, Takemura S, Talebi I, Tarnogorska D, Tenshaw E, Tokhi T, Walsh JJ, Yang T, Horne JA, Li F, Parekh R, Rivlin PK, Jayaraman V, Ito K, Saalfeld S, George R, Meinertzhagen IA, Rubin GM, Hess HF, Jain V, Plaza SM. (2020). A Connectome and Analysis of the Adult Drosophila Central Brain. *BioRxiv*, 2020.04.07.030213. https://doi.org/10.1101/2020.04.07.030213

Scholz M, Linder AN, Randi F, Sharma AK, Yu X, Shaevitz JW, Leifer A. (2018). Predicting natural behavior from whole-brain neural dynamics. *BioRxiv*. https://doi.org/10.1101/445643

Singhvi A, Shaham S. (2019). Glia-Neuron Interactions in Caenorhabditis elegans . *Annual Review of Neuroscience*. https://doi.org/10.1146/annurev-neuro-070918-050314

Sporns O. (2018). Graph theory methods: applications in brain networks. In *Dialogues in clinical neuroscience*.

Stephens GJ, Johnson-Kerner B, Bialek W, Ryu WS. (2008). Dimensionality and dynamics in the behavior of C. elegans. *PLoS Computational Biology*, *4*(4). https://doi.org/10.1371/journal.pcbi.1000028

Symvoulidis P, Lauri A, Stefanoiu A, Cappetta M, Schneider S, Jia H, Stelzl A, Koch M, Perez CC, Myklatun A, Renninger S, Chmyrov A, Lasser T, Wurst W, Ntziachristos V, Westmeyer GG. (2017). NeuBtracker - Imaging neurobehavioral dynamics in freely behaving fish. *Nature Methods*. https://doi.org/10.1038/nmeth.4459

Tomioka M, Adachi T, Suzuki H, Kunitomo H, Schafer WR, Iino Y. (2006). The Insulin/PI 3-Kinase Pathway Regulates Salt Chemotaxis Learning in Caenorhabditis elegans. *Neuron*. https://doi.org/10.1016/j.neuron.2006.07.024

Urbán N, Guillemot F. (2014). Neurogenesis in the embryonic and adult brain: Same regulators, different roles. In *Frontiers in Cellular Neuroscience*. https://doi.org/10.3389/fncel.2014.00396

van den Heuvel MP, Hulshoff Pol HE. (2010). Exploring the brain network: A review on resting-state fMRI functional connectivity. In *European Neuropsychopharmacology*. https://doi.org/10.1016/j.euroneuro.2010.03.008

Venkatachalam V, Ji N, Wang X, Clark C, Mitchell JK, Klein M, Tabone CJ, Florman J, Ji H, Greenwood J, Chisholm AD, Srinivasan J, Alkema M, Zhen M, Samuel ADT. (2016). Pan-neuronal imaging in roaming Caenorhabditis elegans. *Proceedings of the National Academy of Sciences of the United States of America*. https://doi.org/10.1073/pnas.1507109113

Weisenburger S, Vaziri A. (2018). A Guide to Emerging Technologies for Large-Scale and Whole-Brain Optical Imaging of Neuronal Activity. *Annual Review of Neuroscience*. https://doi.org/10.1146/annurev-neuro-072116-031458

Williamson RC, Doiron B, Smith MA, Yu BM. (2019). Bridging large-scale neuronal recordings and large-scale network models using dimensionality reduction. In *Current Opinion in Neurobiology*. https://doi.org/10.1016/j.conb.2018.12.009

Yan G, Vértes PE, Towlson EK, Chew YL, Walker DS, Schafer WR, Barabási AL. (2017). Network control principles predict neuron function in the Caenorhabditis elegans connectome. *Nature*. https://doi.org/10.1038/nature24056